Doctoral Dissertation

Anomalous elastic behavior in Fe-Pd alloys exhibiting a second-order-like FCC-FCT martensitic transformation

Fei Xiao （肖飛）

January 2013

Graduate School of Engineering,
Osaka University

Doctoral Dissertation

Anomalous elastic behavior in Fe-Pd alloys exhibiting a second-order-like FCC-FCT martensitic transformation

Fei Xiao （肖飛）

January 2013

Graduate School of Engineering,
Osaka University

Contents

Chapter 1

Introduction

1.1 Purpose of the present study

The mechanical behavior of shape memory alloys (SMAs) exhibiting a thermoelastic martensitic transformation (MT) has attracted considerable attention in several decades. This behavior is mainly investigated in alloys showing a typical first-order MT, in which the lattice parameters jump discontinuously at the transformation temperature and vary slightly in the martensite phase as shown in Fig. 1.1(a). The typical alloys are Ti-Ni [1,2], Cu-based [3,4] and Ni-Mn-X (X=Ga, In, Sn) [5-7] alloys.

There are some materials exhibiting second-order-like thermoelastic FCC-FCT MTs such as In-Tl alloys [8-10], Mn-Cu alloys [11,12], Fe_3Pt alloys [13,14] and Fe-Pd alloys [15,16]. Here FCT is a tetragonal structure with one axis extended or contracted slightly. Although the Bravais lattice of FCT martensite is BCT (body center tetragonal), we use the term FCT for convenience in this thesis. The martensite transformation in A15 type Nb_3Sn and V_3Si is also second-order-like transformation from a cubic structure to a tetragonal structure. In this class of transformation, the lattice parameters show a small discontinuity at the transformation temperature and then gradually change with decreasing temperature as schematically shown in Fig. 1.1(b). Compared with Ti-Ni and Cu-based SMAs exhibiting clear first-order transformation, the mechanical behavior of the alloys exhibiting a second-order-like transformation is not well understood. So, in this study we investigate the mechanical behavior

and related phenomena in the alloy exhibiting a second-order-like FCC-FCT MT.

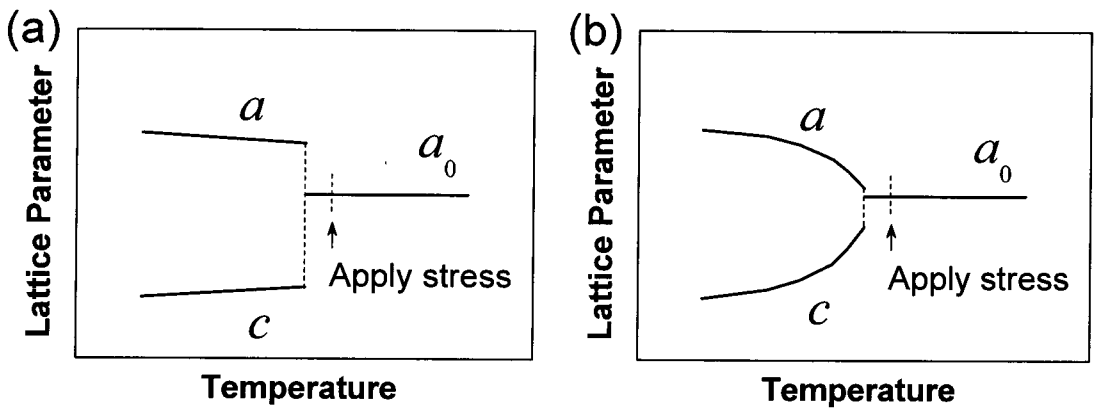

Fig. 1.1. Sketch illustration showing temperature dependence of lattice parameters in a typical first-order MT (a) and a second-order-like FCC-FCT MT (b).

1.1.1 Superelastic behavior

Superelasticity (or pseudoelasticity) in SMAs is widely used because it offers a large recoverable strain before plastic deformation [17]. When a stress is applied above the reverse transformation finish temperature (A_f) in a typical first-order thermoelastic MT, a large nonlinear reversible strain can be obtained as schematically illustrated in Fig. 1.2(a). This large reversible strain primarily arises from the transformation strain $\Delta\varepsilon$ due to the discontinuous structural change between the parent phase and the martensite phase during the loading and unloading processes. The transformation strain is usually characterized by "plateaus" with a significant stress hysteresis in the experimental stress-strain curve, and is uniquely determined from the lattice parameters at the transformation temperature [3,18]. Typical values of transformation strain are between 1% and 10% in conventional SMAs. Compared with the transformation strain, the elastic strains in the parent phase and the martensite phase are usually 1% or smaller in SMAs such as Ti-Ni alloys [1,2] and Cu-Al-Ni alloys [3,4].

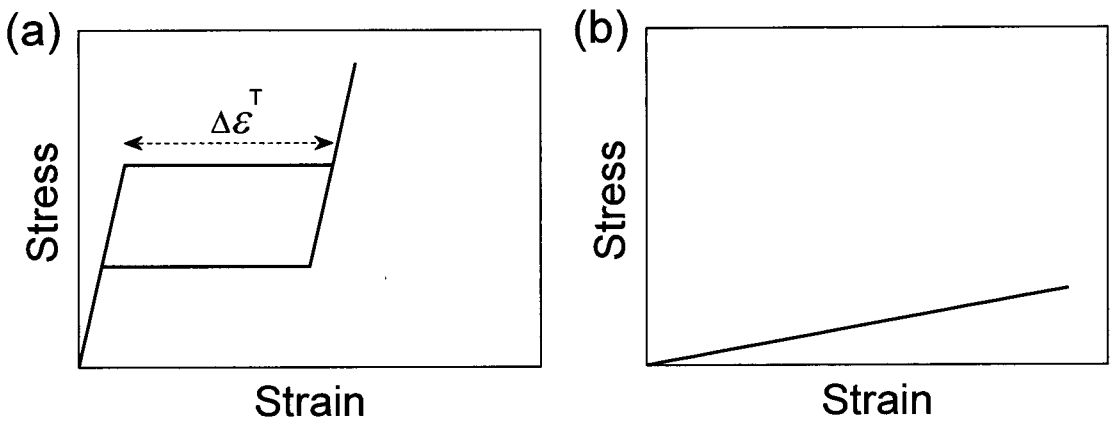

Fig. 1.2. Schematic illustrations showing the superelastic behavior in (a) a typical first-order MT and (b) a second-order-like FCC-FCT MT.

In a second-order-like FCC-FCT MT, the jump of lattice parameters at the transformation temperature is small. This implies a small value of transformation strain. However, the continuous change of lattice parameter in the martensite phase with temperature can be induced by stress. This process should be an elastic deformation, but the lattice distortion is much larger than that of conventional metals; in other words, a large elastic-like deformation should be obtained. Furthermore, this kind of transformation is frequently accompanied with the lattice softening in the parent phase. In particular, the elastic constant $C'(=(C_{11}-C_{12})/2)$ strongly decreases with decreasing temperature, and its value is close to zero near the transformation temperature [19-23]. The Young's modulus in the [001] direction $E_{[001]}$ is given by [24]

$$\frac{1}{E_{[001]}} = \frac{1}{9K} + \frac{1}{3C'}, \tag{1.1}$$

where $K = (C_{11}+2C_{12})/3$ is the bulk modulus. In the case of C' is much smaller than K, the Young's modulus in the [001] direction can be approximated as

$$E_{[001]} \approx 3C'. \tag{1.2}$$

Consequently, a large elastic strain with low Young's modulus is expected to be obtained in the [001] direction as shown in Fig. 1.2(b), when C' is small.

1.1.2 Critical point in the stress-temperature phase diagram

In the alloy exhibiting a second-order-like FCC-FCT MT, when the FCC parent phase is compressed in the [001] direction, it contracts in the [001] direction and expands in the [100] and [010] directions. Consequently, the elastically deformed parent phase has tetragonal symmetry, not cubic symmetry. This means that the martensitic transformation in these alloys under a uniaxial stress is tetragonal to tetragonal transformation although it is usually described as FCC to FCT transformation. When the two phases separated by a phase boundary have the same symmetry, the phase boundary could terminate at a point termed as a critical point. Beyond the critical point, there is no difference between the elastically deformed parent phase and the martensite phase. This behavior in the case of the tetragonality being less than unity is illustrated in Fig. 1.3.

The appearance of such a critical point is well know for gas-liquid transformation [25,26], in which gas and liquid phases have the same symmetry (isotropy structure). The pressure-temperature phase diagram of water is shown in Fig. 1.4. On approaching the critical point, the liquid phase and the gas phase become indistinguishable.

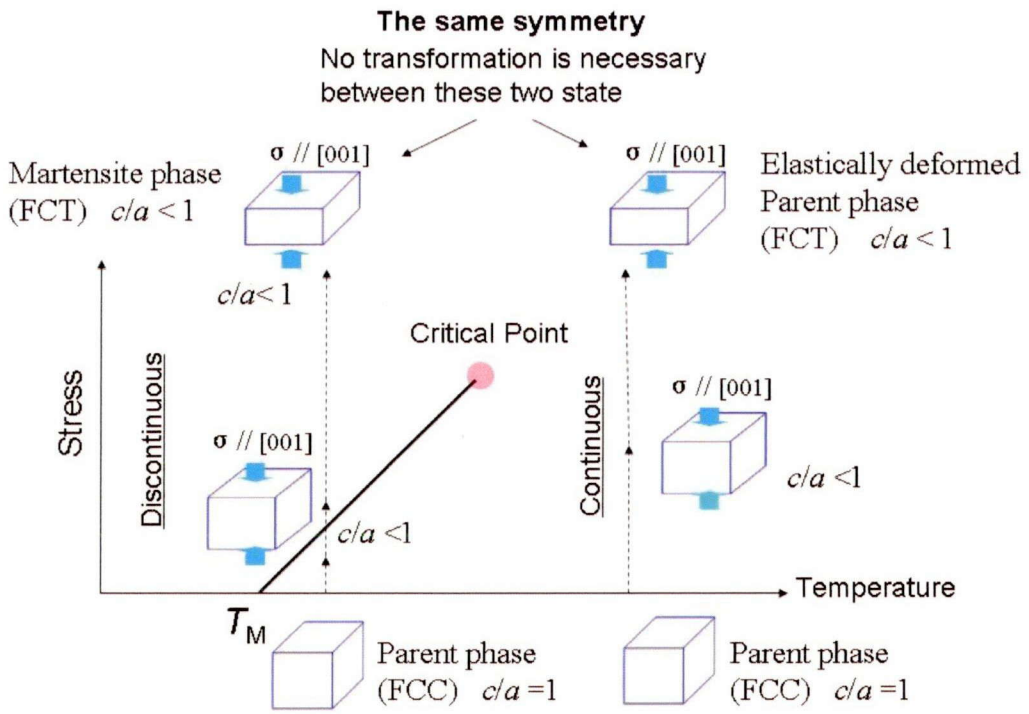

Fig.1.3. Sketch of a critical point in the stress-temperature phase diagram of an alloy exhibiting a second-order-like FCC-FCT MT with the tetragonality less than unity.

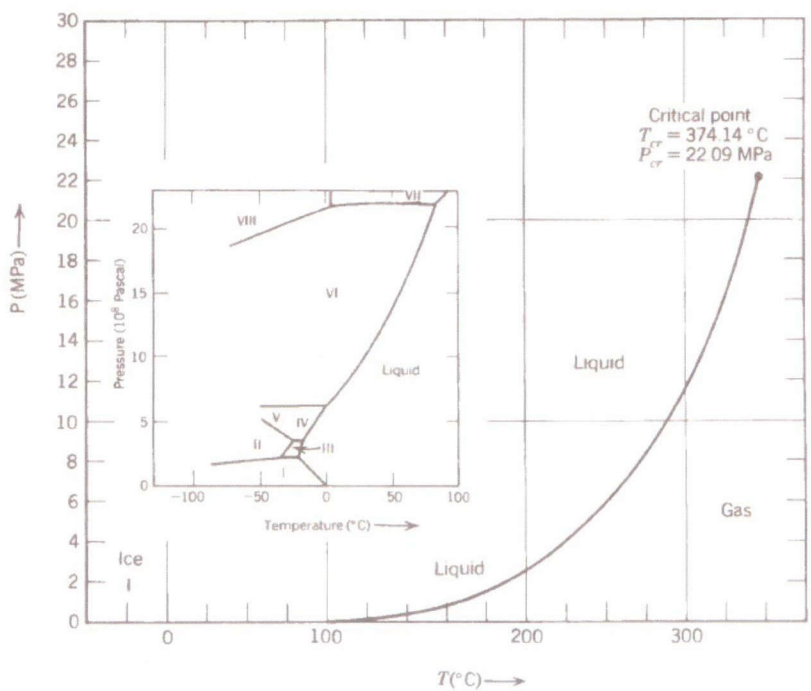

Fig. 1.4. The pressure-temperature phase diagram of water with a critical point [26].

The essentially important condition for the appearance of the critical point in the alloys exhibiting a second-order-like FCC-FCT MT is that the parent and the martensite phases have the same symmetry under a uniaxial stress. This condition is difficult to be satisfied in SMAs showing a typical first-order MT. For example, in case of the B2-B19' transformation in Ti-Ni alloy [1,2], the martensite phase is monoclinic; there is no way to obtain a monoclinic symmetry by applying a uniaxial stress on the cubic (B2) parent phase. The same conclusion is reached for 2H, 4H, 9R 18R, 10M, 14M transformations observed in Cu-based SMAs [3,4] and Ni-Mn-X (X=Ga, In, Sn, Al) based magnetic SMAs [5-7]. The phase boundary in these alloys must be terminated by intersecting the equilibrium curves of other phases or slip.

1.1.3 Elastocaloric effect

As mentioned in section 1.1.1, a characteristic feature of the alloys exhibiting a second-order-like FCC-FCT MT is the lattice softening in the parent phase. The elastic constant C' significantly depends on temperature [23] and can be simply expressed as linear relationship

$$\frac{\partial C'(T)}{\partial T} \approx k , \tag{1.3}$$

where k is a constant positive value. Considering a simple elastic deformation, the strain in the [001] direction ε obeys Hooke's law

$$\varepsilon = E_{[001]}^{-1}\sigma , \tag{1.4}$$

where σ is the uniaxial stress in the [001] direction and $E_{[001]}$ is the Young's modulus in the [001] direction which can be replaced by equation (1.2). So, ε as a function of temperature can be further expressed as

$$\varepsilon \approx (3C'(T))^{-1}\sigma , \tag{1.5}$$

and it simply illustrated in Fig. 1.5(a). It is found that the strain under a constant stress in the [001] direction increase continuously with decreasing temperature. The absolute value of

derivative of strain by temperature can be expressed as

$$\left|\frac{\partial \varepsilon}{\partial T}\right|_{\sigma} \approx \frac{\sigma k}{3C'(T)^2}. \tag{1.6}$$

For the alloys exhibiting a second-order-like MT, the value k is large and elastic constant C' is small, so the value $\left|\frac{\partial \varepsilon}{\partial T}\right|_{\sigma}$ is large.

By using the Maxwell relation, the isothermal entropy change ΔS_{iso} induced by an uniaxial stress σ is expressed as [27]

$$\Delta S_{iso}(0 \rightarrow \sigma) = \int_0^{\sigma} \left(\frac{\partial \varepsilon}{\partial T}\right)_{\sigma} d\sigma \ . \tag{1.7}$$

A large elastocaloric effect (large entropy change) in a wide temperature range is expected to be obtained in SMAs exhibiting a second-order-like FCC-FCT MT. In conventional SMAs with a typical first-order MT, the large elastocaloric effect is limited to appear in the vicinity of the transformation temperature (Fig. 1.5(b)); the temperature range of the large elastocaloric effect is much shorter than that of the SMAs showing a second-order-like FCC-FCT MT. In addition, the elastic deformation in the SMAs exhibiting a second-order-like FCC-FCT MT indicates a quite small stress hysteresis; in other words, quite low energy dissipation will be realized. Due to the large elastocaloric effect and low hysteresis loss in a wide temperature range, SMAs exhibiting a second-order-like FCC-FCT MT can be a candidate material for an environmentally friendly refrigerator system.

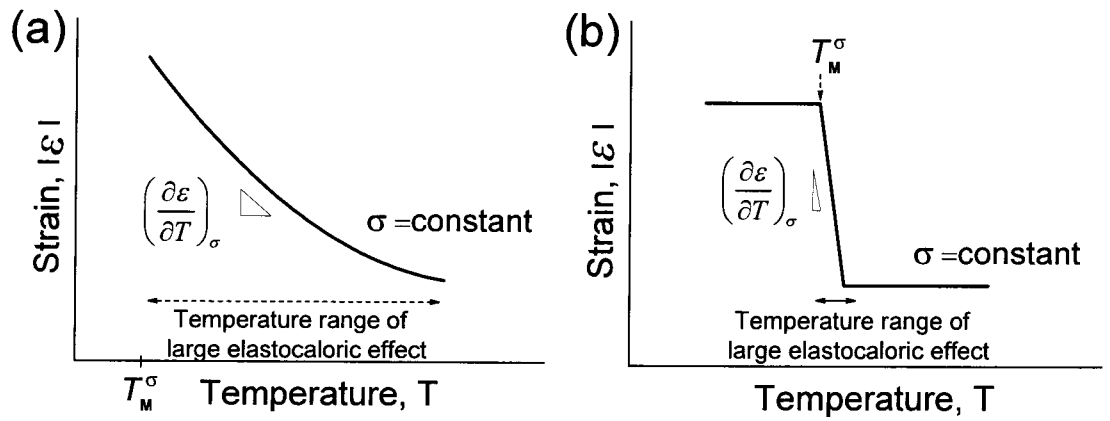

Fig. 1.5. Schematic illustrations of the temperature range of a large elastocaloric effect in (a) a stress-induced second-order-like FCC-FCT MT and (b) a typical stress-induced first-order MT.

1.1.4 Damping behavior

Usually, the internal friction (IF) spectrum during a typical first-order MT is decomposed into three terms [28-30] as shown in Fig. 1.6(a):

$$IF=IF_{Tr}+IF_{PT}+IF_{Int}. \quad (1.8)$$

The first term, IF_{Tr}, is the transitory term (or kinetic term), which shows a peak during the MT and only appears at non-zero cooling/heating rate. The second term, IF_{PT}, is the phase transition term (or isothermal term), which origins from the phase transformation itself but is independent of the cooling/heating rate. The third term, IF_{Int}, is intrinsic term, which arises from the microstructure of each phases. In conventional SMAs exhibiting a typical first-order MT such as Ti-Ni-based [31-33] or Cu-based alloys [28,34,35], the high damping characteristic is mainly caused by the first term IF_{Tr}; it appears in a narrow temperature range between M_s and M_f. The inherent internal damping values ($IF_{PT}+IF_{Int}$) in these alloys is small under isothermal condition.

Due to the near continuous change in the lattice parameter at the transformation temperature

in the SMAs exhibiting a second-order-like FCC-FCT MT, the first term IF_{Tr} can be small. The twinning structure is always reported in the martensite phase of these alloys [9,11,14,36]. It is well known that the energy dissipation during the movement of the twined boundaries is an important source of high damping behaviors [34]. So a high sustainable damping behavior obtained from internal damping value is expected to be obtained as shown in Fig. 1.6(b).

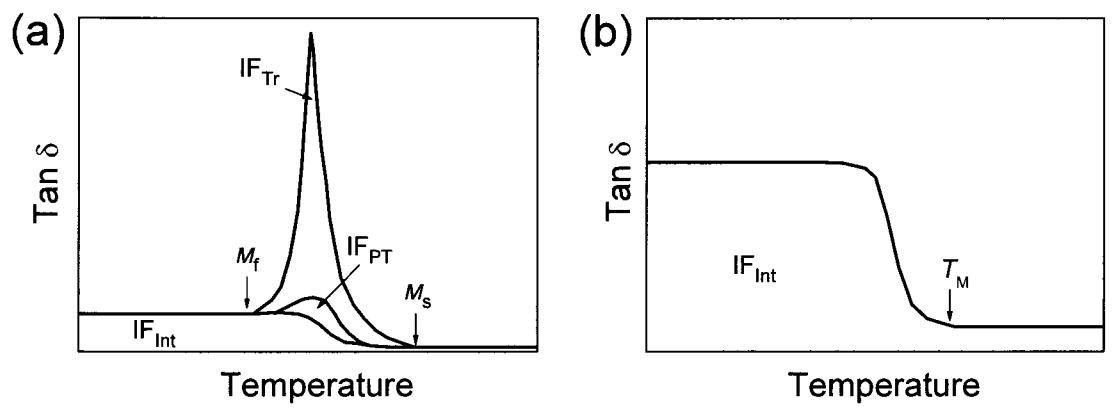

Fig. 1.6. Schematic representation of the internal friction during a typical first-order MT (a) and a second-order-like MT (b).

On the other hand, the energy dissipation caused by stress hysteresis plays an important role to determine the usefulness of a refrigeration system. Fortunately, dynamic mechanical analyzer just provides a direct way to detect the energy dissipation. So, it is necessary to investigate the dynamic mechanical properties of these alloys.

1.2 Second-order-like FCC-FCT MT in Fe-Pd alloys

Among the alloys exhibiting a second-order-like FCC-FCT MT, an Fe-Pd alloy is a promising SMA owing to its high corrosion resistance, ductility and biocompatibility [37,38]. So, in this thesis, we will investigate the related phenomena expected from a second-order-like martensitic

transformation in Fe-Pd alloys such as a large elastic deformation, a large elastocaloric effect and a critical point in the stress-temperature phase diagram.

Figure 1.7 shows the equilibrium phase diagram of the Fe-Pd alloys [39]. Alloys with Pd concentration near 30 at.% have liquid phase when the temperature above 1623 K. The liquid phase solidifies into disordered FCC phase below 1623 K, and the disordered FCC structure decomposes into α-Fe and γ-phase when the temperature is between 878 K and 1023 K. Below 878 K, the equilibrium phase contains α-Fe and ordered $L1_0$ FePd. But, through quickly cooling, the disordered FCC phase can be retained, and this FCC phase exhibits a martensitic transformation.

It has been reported that the MT in Fe-Pd alloys strongly depends on their Pd content [15,40]. The alloys with low Pd content transform from the FCC parent phase to the BCC martensite phase. The transformation product changes to the BCT martensite as the Pd content increases, and alloys with Pd content of approximately 30 at.% and more transform to the so-called FCT martensite. However, there are few systematic studies on Pd content dependence of the FCC-FCT transformation temperature. The most well referred phase diagram for martensitic transformation in the Fe-Pd system is that reported by Sugiyama et al. [36] as shown in Fig. 1.8. However, the transformation temperatures they reported are lower than recently examined transformation temperatures [36,41]. One possibility of this deviation is that Sugiyama et al. determined the transformation temperature by optical microscope observation. In addition, they did not examine transformation below 77 K. In chapter 2, we investigate the FCC-FCT MT temperature by magnetic susceptibility which is more sensitive than the method employed by Sugiyama et al.

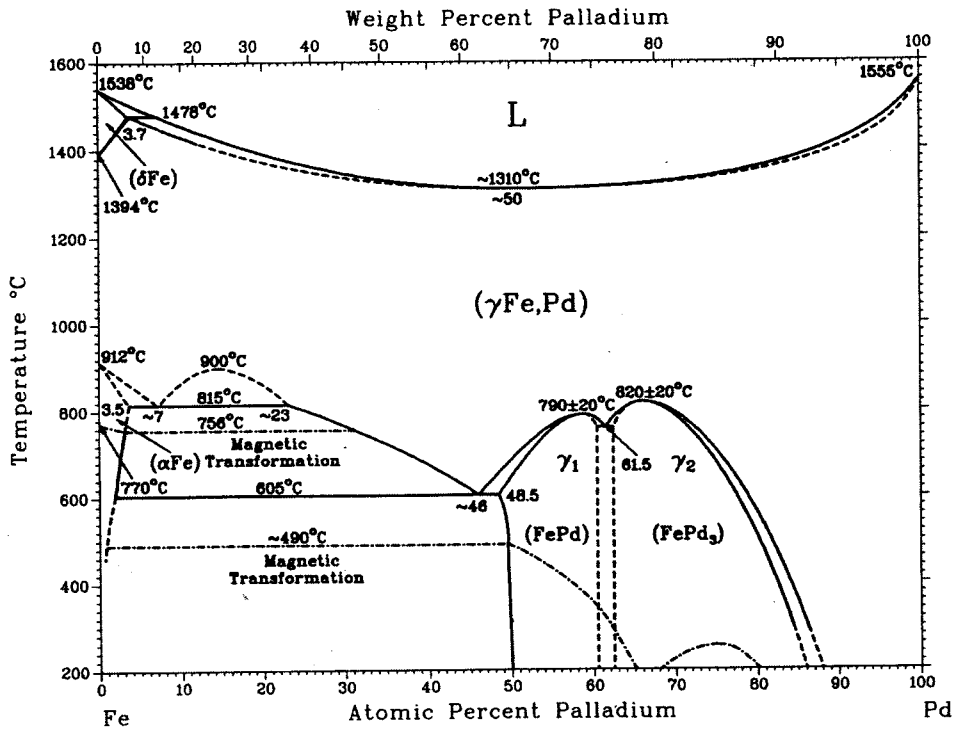

Fig. 1.7. Equilibrium phase diagram of Fe-Pd alloy [39].

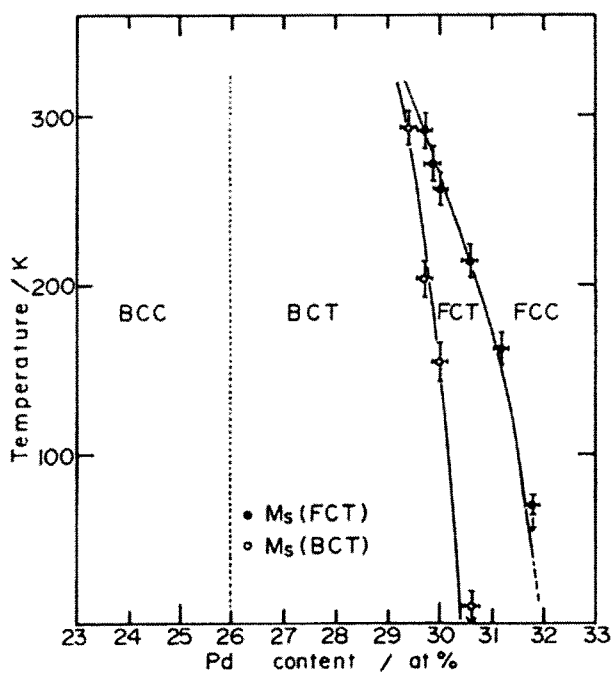

Fig. 1.8. Pd concentration dependence of FCC-FCT martensitic transformation temperature in Fe-Pd alloys [36].

The thermally-induced FCC-FCT MT in an Fe-Pd alloy has been extensively investigated especially in 1980s [15,36,40]. During this transformation, the cubic structure undergoes contraction in the *c*-axis and expansion in the *a*-axes. Three variants are introduced in the martensite phase; and a simple sketch of the transformation is shown in Fig. 1.9(a). Below the transformation temperature, the lattice distortion (1-*c*/*a*) increases gradually with decreasing temperature. Figs. 1.9(b) and (c) show the lattice parameters and the lattice distortion of an Fe-30.0Pd (at.%) alloy as a function of temperature [40], respectively.

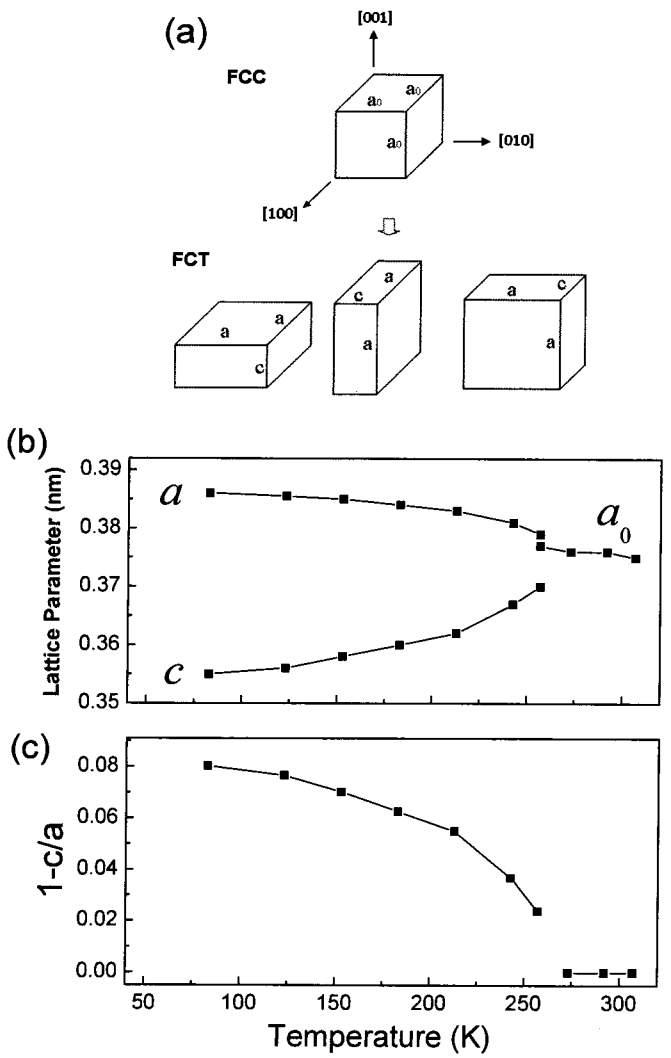

Fig. 1.9. (a) A schematic illustration of FCC structure and FCT structures with three variants. Temperature dependence on the lattice parameters (b) and the lattice distortion value (c) of an Fe-30.0Pd (at.%) alloy [40].

The lattice softening in the parent phase of Fe-Pd alloys is also reported, and the elastic constant C' [=(C_{11}-C_{12})/2] is found to show quite a low value near the transformation temperature due to the band Jahn-Teller effect [42]. Temperature dependence on the elastic constants of an Fe-30.0Pd (at.%) alloy [23] is shown in Fig. 1.10. It is found that the elastic constant C' decreases significantly on approaching the transformation temperature.

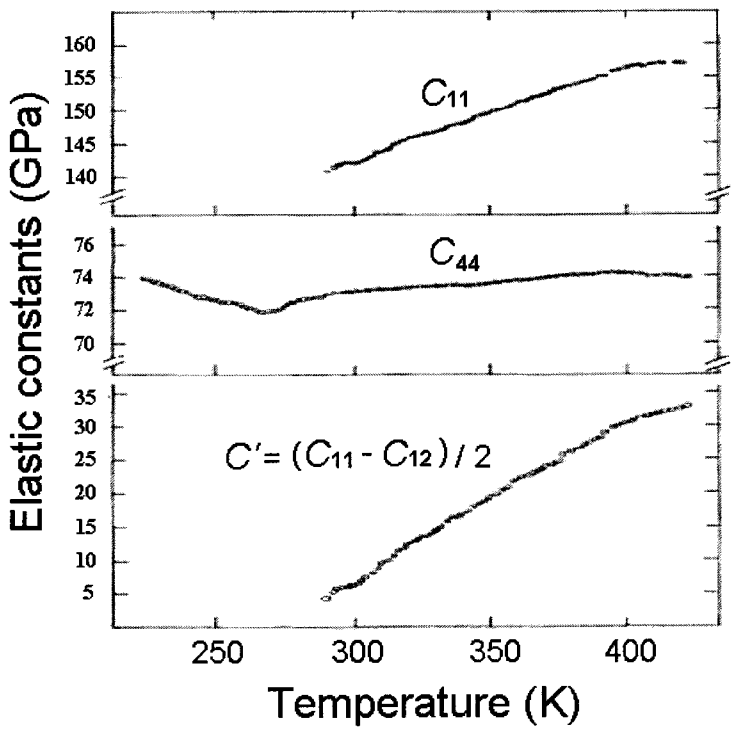

Fig. 1.10. Temperature dependence of the elastic constants of an Fe-30.0Pd (at.%) alloy [23].

When a single crystal is compressed in the [001] direction, a single variant with its *c*-axis in the compressive axis should be formed for the tetragonality is less than unity (c/a<1). Owing to the continuous change in lattice parameter and the lattice softening, we can expect that a large elastic-like strain with low Young's modulus in the [001] direction is obtained in this alloy. In chapter 3, we investigate the superelastic behavior in an Fe-31.2Pd (at.%) single crystal compressed in the [001] direction. It is also found that the elastic constant C_{44} is not so

sensitive to temperature. Considering that elastic constants depend strongly on temperature and orientation, the limit of the elastic strain in Fe-Pd alloys could significantly depend on these factors. In chapter 4, we consider the influence of various conditions on the limit of elastic deformation in Fe-Pd alloys. When an Fe-Pd single crystal is compressed in the [001] direction, the symmetry of the elastically deformed parent phase is the same as the martensite phase. In chapter 5, the existence of the critical point in Fe-Pd alloys is checked by compressive tests. The large elastocaloric effect caused by temperature significantly dependence of elastic constant C' is also confirmed in chapter 6. The dynamic mechanical behavior in Fe-Pd alloy is presented in chapter 7.

1.3 Outline of the thesis

In this thesis, we investigate the elastic behavior in Fe-Pd alloys exhibiting lattice softening and a second-order-like FCC-FCT MT. In chapter 1, the motivations and purposes of this research work are described. In chapter 2, influence of Pd content on FCC-FCT MT temperature of Fe-Pd alloys is studied. In chapter 3, the large elastic-like deformation of an Fe-31.2Pd (at.%) single crystal by compressing in the [001] direction is studied. In addition, the structural change in the elastically deformed specimen and defects in the plastically deformed specimen are studied in details. In chapter 4, the limit of the elastic deformation under different conditions such as temperature, compressive direction and grain boundary are considered. In chapter 5, the stress-temperature phase diagram of Fe-30.8 and 31.2Pd (at.%) single crystals is constructed, and the existence of the critical point (end point of the equilibrium phase curve) is confirmed. In chapter 6, the elastocaloric effect in an Fe-31.2Pd (at.%) single crystal due to the significant temperature dependence on the elastic constant C' is studied. In chapter 7, the dynamic mechanical behavior and energy dissipation in the loading and unloading processes are also studied. In chapter 8, the results of the present study are summarized.

References

[1] S. Miyazaki, K. Otsuka and Y. Suzuki, *Scr. Metall.*, **15** (1981) 287.

[2] T. Saburi, S. Nenno, Y. Nishimoto and M. Zeniya, *J. Iron and Steel Inst. Japan*, **72** (1986) 571.

[3] K. Otsuka, C. W. Wayman, K. Nakai, H. Sakamoto and K. Shimizu, *Acta. Metall.*, **24** (1976) 207.

[4] H. Horikawa, S. Ichinose, K. Morri, S. Miyazaki and K. Otsuka, *Metall. Trans.*, **19A** (1988) 915.

[5] S. J. Murray, M. Marioni, S. M. Allen, R. C. O'Handley and T. A. Lograsso, *Appl. Phys.Lett.*, **77(6)** (2000) 886.

[6] T. Krenke, M. Acet, E. F. Wassermann, X. Moya, L. Manosa, A. Planes, *Phys. Rev. B*, **72(1)** (2005) 014412.

[7] T. Krenke, E. Duman, M. Acet, E. F. Wassermann, X. Moya, L. Manosa, A. Planes, *Nature Mater.*, **4(6)** (2005) 450.

[8] J. S. Bowles, C. S. Barrett and L. Guttman, *Trans. AIME,* **188** (1950) 1478.

[9] Z. S. Basinski and J. W. Christian, *Acta. Metall.*, **2** (1954) 101.

[10] M. W. Burkar and T. A. Read, *Trans. AIME*, (1953) 1516.

[11] F. T. Worrell, *J. Appl. Phys.*, **19** (1948) 929.

[12] J. A. Hedley, *Mater. Sci. J.*, **2** (1968) 129.

[13] R. Oshima, S. Sugimoto, M. Sugiyama, T. Hamada and F. E. Fujita, *Trans. JIM*, **26** (1985) 523.

[14] S. Muto, R. Oshima and F. E. Fujita, *Metall. Trans.*, **19A** (1988) 2723.

[15] T. Sohmura, R. Oshima and F. E. Fujita, *Scr. Metall.*, **14** (1980) 855.

[16] M. Matsui, H. Yamada and K. Adachi, *J. Phys. Soc. Jpn.*, **48** (1980) 2161.

[17] K. Otsuka and C. W. Wayman, *Shape Memory Materials*, (Cambridge University Press, Cambridge 1998).

[18] T. Saburi and S. Nenno, *Proc. Int. Conf. on Solid-Solid Phase Transformations*, (AIME, NY, 1982) 1455.

[19] O. Nittono and Y. Koyama, *J. J. Appl. Phys.*, **21** (1982) 680.

[20] D. J. Gunton and G. A. Saunders, *Solid State Commun.*, **14** (1974) 865.

[21] K. Sugimoto, T. Mori and S. Shiode, *Met. Sci. J.*, **7** (1973) 103.

[22] H. C. Ling and W. S. Owen, *Acta. Metall.* **31** (1983) 1343.

[23] S. Muto, R. Oshima and F. E. Fujita, *Acta. Metall.*, **38** (1990) 685.

[24] N. Nakanishi, *Prog. Mater. Sci.*, **24** (1980) 143.

[25] L. Landau and E. Lifshitz, *Statistical Physics*, (Pergamon Press 1990) part 1, 3rd ed.

[26] H. B. Callen, *Thermodynamics and an Introduction to Thermostatistics,* (Jonn Wiley & Sons, 1985).

[27] E. Bonnot, R. Romero, L. Manosa, E. Vives, and A. Planes, *Phys. Rev. Lett.*, **100** (2008) 125901.

[28] J. San. Juan and M. L. Nó, *J. Alloys Comp.*, **355** (2003) 65.

[29] J. E. Bidaux, R. Schaller and W. Benoit, *Acta. Metall.*, **37** (1989) 803.

[30] J. Van. Humbeeck, J. Stoiber, L. Delaey and R. Gotthardt, *Z. Metalkd.* **86** (1995) 1976.

[31] S. H. Chang and S. K. Wu, *Scr. Mater.*, **55** (2006) 311.

[32] Y. Liu, J. Van Humbeeck, R. Stalmans, L. Delaey, *J. Alloys Compd.*, **247** (1997) 115.

[33] S. K. Wu and H. C. Lin, *J. Alloys Comp.*, **355** (2003) 72.

[34] J. Van. Humbeeck, *J. Alloys Comp.*, **355** (2003) 58.

[35] S. H. Chang, *Mater. Lett.*, **64** (2010) 93.

[36] M. Sugiyama, R. Oshima and F. E. Fujita, *Trans. JIM.*, **25** (1984) 585.

[37] Y. Ma, M. Zink and S. G.. Mayr, *Appl. Phys. Lett.*, **96** (2010) 213703.

[38] J. Cui, T. W. Shield and R. D. James, *Acta. Mater.*, **52** (2004) 35.

[39] B. Massalski, J. L. Murray, L. H. Bennett and H. Baker: *Binary alloy phase diagrams*, Metals Park, Ohio, American Society for Metals (1986).

[40] F. E. Fujita, *Mater. Sci. Eng. A.*, **127** (1990) 243.

[41] T. Okazaki, Y. Iwai, Y. Furuya, *Mater. Trans.* **49** (2008) 360.

[42] O. Ingo, K. Koepernik, U. Nitzsche and M. Richter, *Appl. Phys. Lett.*, **94** (2009) 072508.

Chapter 2

Concentration dependence of FCC to FCT martensitic transformation in Fe-Pd alloys

2.1 Introduction

As mentioned in chapter 1, the FCC-FCT transformation temperature in Fe-Pd alloy is an important factor to investigate superelastic behaviors and related phenomena. In this chapter, therefore, the Pd concentration dependence of FCC-FCT MT temperature in Fe-Pd alloys is investigated, and the structural change and latent heat during the transformation are also studied.

2.2 Experiments

Ingots of Fe-30.0~33.6Pd (at.%) were prepared by arc melting from with high purity Fe rod (99.998%) and Pd sheet (99.9%) starting materials. The ingots were homogenized at 1373 K for 24 h followed by quenching in ice water to keep the disordered parent phase. The Pd concentration of Fe-Pd alloys is measured by an Inductively Coupled Plasma (ICP) method, and the results are listed in Table. 2.1. It is found that the detected Pd concentration deviates from the nominal concentration less than 0.1%.

Table. 2.1. The results of the ICP measurements.

Nominal Pd content (at.%)	31.6	32.0	32.4	32.6	32.8	33	33.1	33.2	33.6
Pd content by ICP analysis	31.59	32.02	32.32	32.47	32.82	33.08	33.16	33.25	33.52
Deviation	-0.01	+0.02	-0.08	-0.13	+0.02	+0.08	+0.06	+0.05	-0.08

The FCC-FCT martensitic transformation temperature was determined by a magnetic susceptibility measurement under the magnetic field of 0.05 T with a constant cooling and heating rate of 2 K/min by using a Superconducting Quantum Interference Device (SQUID) magnetometer. Latent heat measurements were performed by a Differential Scanning Calorimeter (DSC) NETZSCH model 200F3 at a cooling and heating rate of 10 K/min. An Fe-33.2Pd (at.%) single crystal was made by the floating zone method at a growth rate of 3 mm/h. Plate-shaped specimens composed of $(100)_P$, $(010)_P$ and $(001)_P$ planes (the subscript "P" represents parent phase) were cut from this single crystals. After homogenization at 1373 K, the Fe-33.2Pd (at.%) single crystal was quenched in ice water. Temperature dependence of the lattice parameters of the Fe-Pd single crystal was obtained by an *in-situ* X-ray diffraction using Cu-K_α radiation.

2.3 Results and discussion

Figure 2.1 shows magnetic susceptibilities of Fe-Pd alloys measured under the magnetic field of 0.05 T. The magnetization measured in the cooling process exhibits a sudden decrease in alloys with Pd content of 33.0 at.% and less, which is caused by the FCC→FCT transformation. The correspondence between the decrease in magnetic susceptibility and phase transformation has been confirmed in an Fe-31.2Pd (at.%) alloy by X-ray diffraction [1]. It is found that the

temperature hysteresis in the MT is quite small due to the characteristic of the second-order-like MT. The sudden decrease in magnetization does not appear in alloys with Pd content of 33.1 at.% and more. Probably, these alloys do not show any MT.

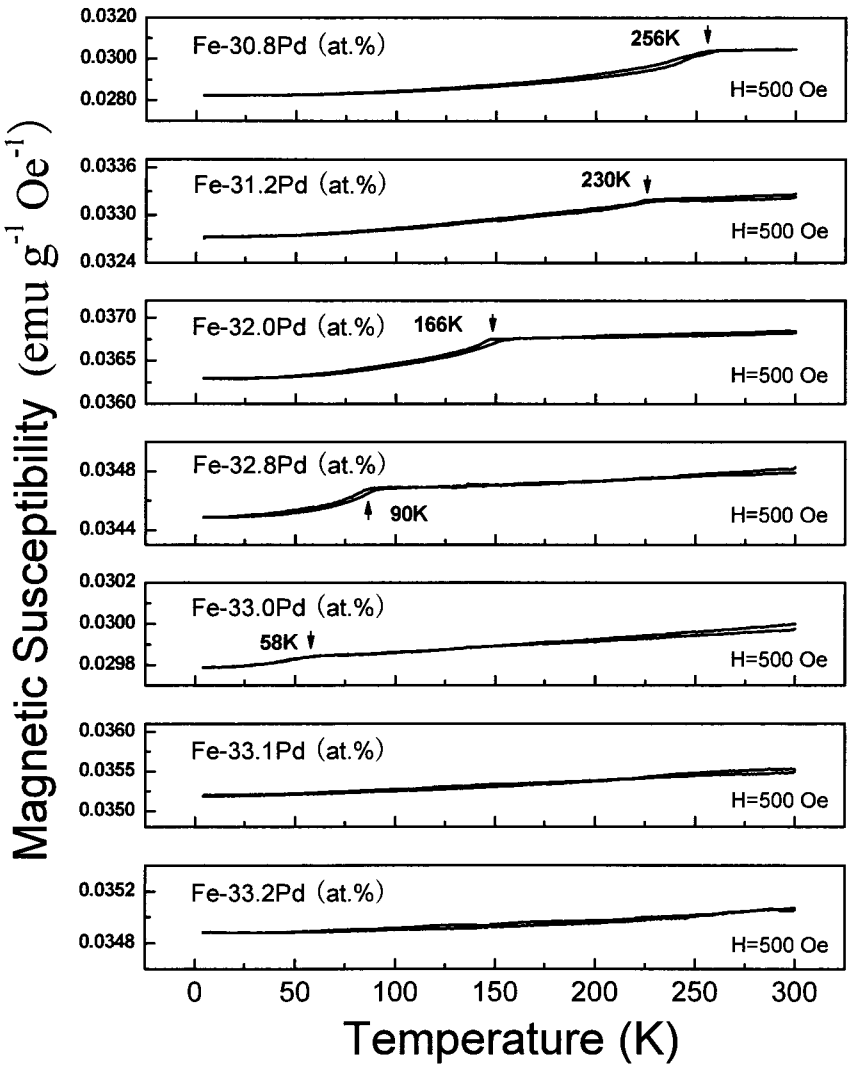

Fig. 2.1. Temperature dependence of the magnetic susceptibility of Fe-Pd alloys.

In order to confirm that MT does not occur in alloys with Pd content 33.1 at.% and more, we have made an *in-situ* X-ray experiment for the Fe-33.2Pd (at.%) single crystal. Figure 2.2 shows the change in the profile of (400) X-ray spectra measured in the cooling process from 290 K to 10 K. There is no peak separation at any temperature examined, which confirms that there is no

FCC→FCT martensitic transformation in an Fe-33.2Pd (at.%) alloy. This result is consistent with the result obtained by magnetic susceptibility measurement. The lattice parameter of the Fe-33.2Pd (at.%) alloy obtained by the diffraction pattern is plotted as a function of temperature in Fig. 2.3 together with the results of an Fe-31.2Pd (at.%) alloy, which shows the FCC-FCT martensitic transformation, previously reported [1].

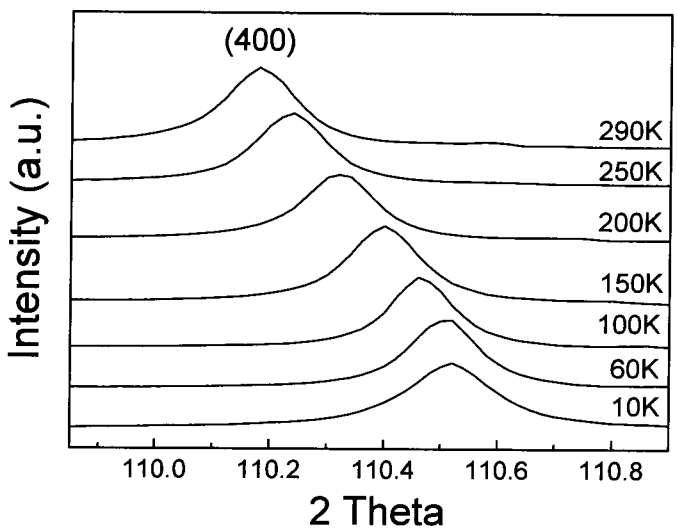

Fig. 2.2. The change of (400) X-ray spectra of an Fe-33.2Pd (at.%) single crystal with decreasing temperature. $K_{\alpha 2}$ reflections are removed by a software.

The lattice parameter of the Fe-33.2Pd (at.%) alloy increases gradually with increasing temperature. The corresponding thermal expansion coefficient α of the Fe-33.2Pd (at.%) alloy is 1□ 10^{-6} K^{-1} from 10 K to 60 K; it is 9□ 10^{-6} K^{-1} from 60 K to 290 K. This value is significantly smaller than that of pure iron (12□ $10^{-6}K^{-1}$) [2], but is much larger than that of the Invar alloy Fe-36.0Ni (at.%) (1.2□ $10^{-6}K^{-1}$) [3]. The thermal expansion coefficient α of the Fe-33.2Pd (at.%) alloy in our work is consistent with the result of an Fe-32.0Pd (at.%) alloy reported by M. Matsui et al. [4]. The Full-Width Half-Maximum (FWHM) of the diffraction peaks in Fig. 2.2 is evaluated; it increases with decreasing temperature below 90 K as shown in Fig. 2.4. The broadening of the diffraction peaks might be attributed to the pre-transformation.

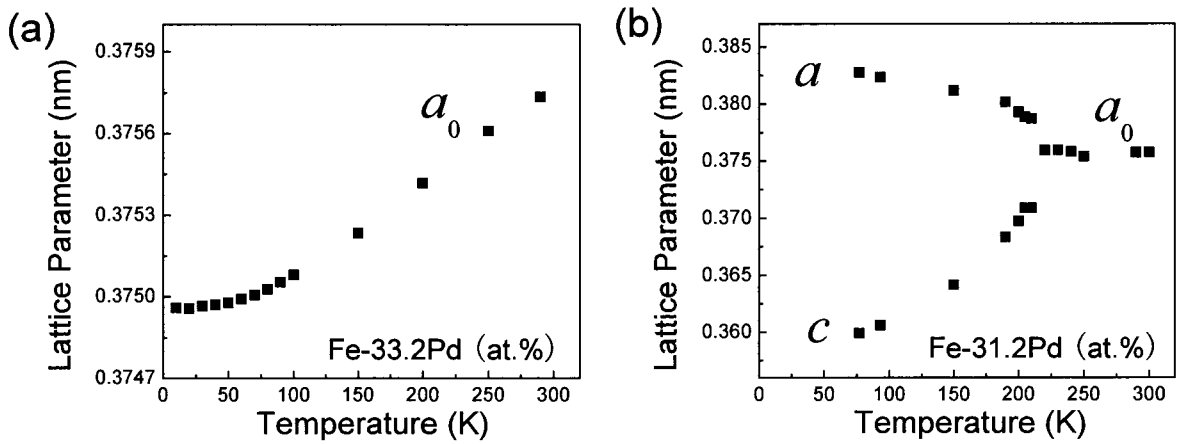

Fig. 2.3. Temperature dependence of the lattice parameters of (a) an Fe-33.2Pd (at.%) alloy and (b) an Fe-31.2Pd (at.%) alloy [1].

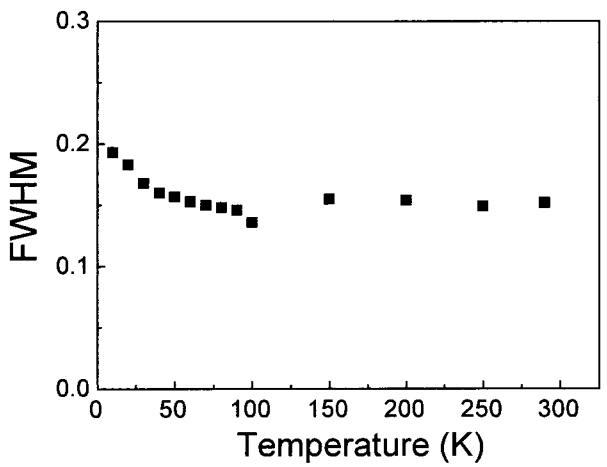

Fig. 2.4. The change of Full-Width Half-Maximum (FWHM) in (400) diffraction peaks of an Fe-33.2Pd (at.%) single crystal with decreasing temperature.

The transformation start temperature obtained by a magnetic susceptibility measurement is plotted as a function of Pd content in Fig. 2.5 (triangle). It is noted in the figure that the transformation temperature decreases by approximately 10 K per 0.1 at.% of Pd, which means the transformation temperature is very sensitive to the Pd concentration. The transformation temperatures in our work are slightly higher than those reported by Sugiyama et al. [5] with the same composition. The reason may be attributed to the different methods of determining the

transformation temperatures. The method used by Sugiyama et al. was optical microscope observation. Presumably, magnetic susceptibility measurement is more sensitive to detect the initiation of structure change than optical microscope observation.

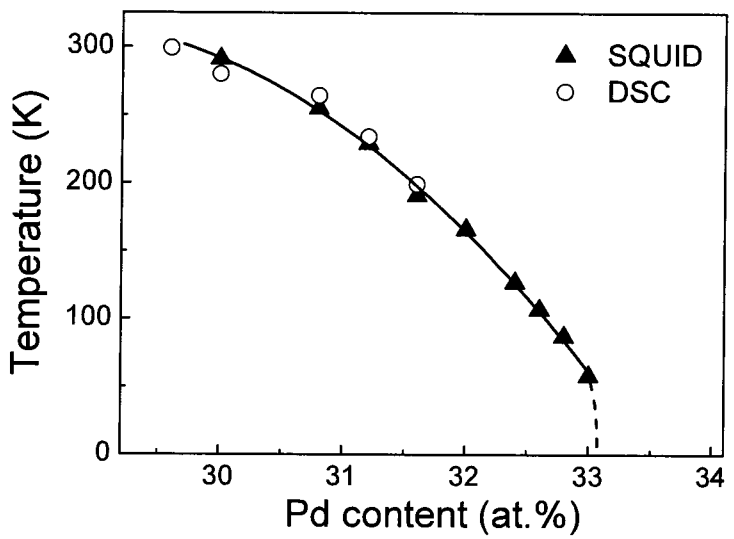

Fig. 2.5 FCC-FCT martensitic transformation temperature of Fe-Pd alloys obtained by magnetic susceptibility and DSC measurements.

Figure 2.6 shows the DSC heat flow of Fe-Pd alloys with Pd concentrations of 30.0 at.%, 30.8 at.%, 31.2 at.% and 31.6 at.%. The DSC cooling curve shows one exothermic peak corresponding to the FCC→FCT martensitic transformation. Also, the DSC heating curve shows one endothermic peak corresponding to the FCT→FCC reverse martensitic transformation. No obvious latent heat is detected when the palladium concentration is 32.0 at.%Pd and more. The FCC→FCT martensitic transformation start temperature M_S obtained from Fig. 2.6 are summarized in Table 2.2. Also M_S is plotted as a function of temperature in Fig. 2.6. The transformation temperatures obtained by DSC method coincide well with those obtained by magnetic susceptibility measurements. The electrical resistivity is another method to determine the martensitic transformation temperature with high sensitivity. Unfortunately, there is no obvious change in electrical resistivity during the transformation in the presented alloys [5].

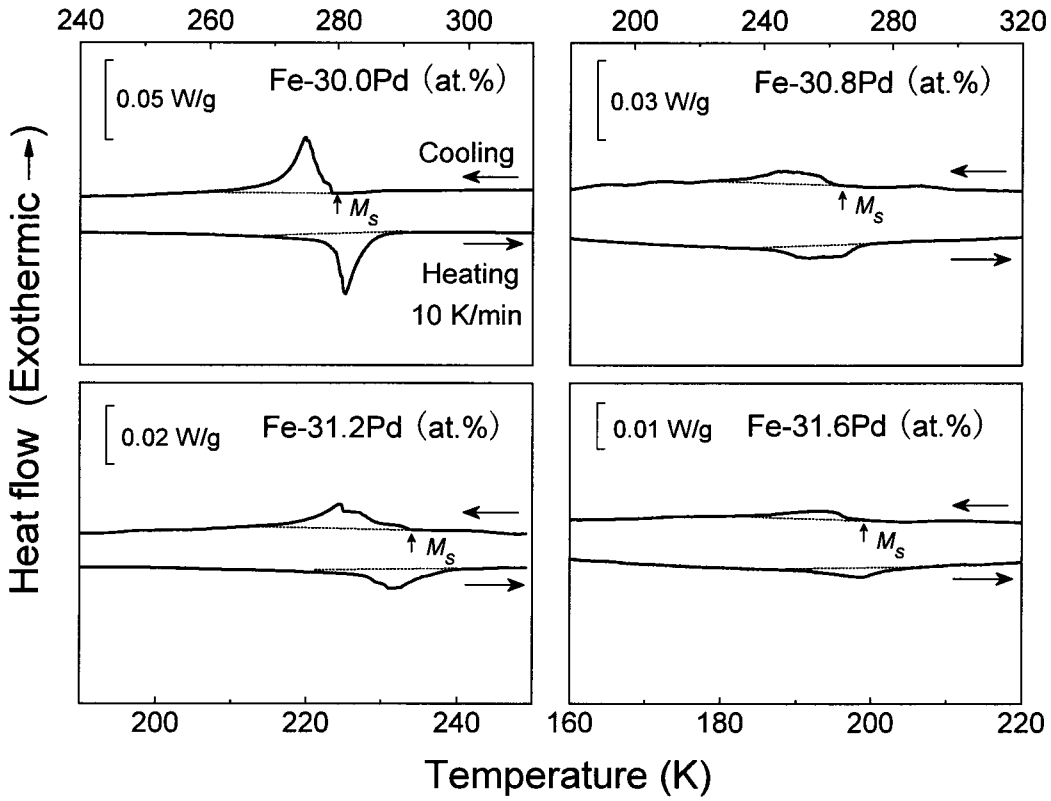

Fig. 2.6 DSC curves of Fe-Pd alloys with Pd concentration of 30.0 at.%, 30.8 at.%, 31.2 at.% and 31.6 at.%.

Table 2.2 FCC-FCT martensitic transformation temperatures and latent heat obtained by DSC measurements.

	M_S (K)	ΔH (J·mol^{-1})
Fe-30.0Pd (at.%)	280	70
Fe-30.8Pd (at.%)	264	38
Fe-31.2Pd (at.%)	234	21
Fe-31.6Pd (at.%)	199	5

The latent heat (ΔH) is obtained as the average area of the DSC peak during heating and cooling, which is also shown in Table 2.2. The value of the latent heat in Fe-Pd alloys is quite small compared with that in other shape memory alloys such as Ti-Ni (995 J/mol [6]) and Cu-Al-Ni (395 J/mol [7]). Such small latent heat in Fe-Pd alloy could be attributed to the characteristic of the second-order-like FCC-FCT martensitic transformation.

2.4 Conclusions

The FCC-FCT martensitic transformation temperature of Fe-Pd alloys decreases with increasing Pd content up to 33.0 at.%Pd and the transformation is suppressed in alloys including 33.1 at.%Pd and more. The latent heat of Fe-Pd alloy decreases with increasing Pd content, and is much lower than that in other shape memory alloys, which could be attributed to the characteristic of the second-order-like FCC-FCT martensitic transformation.

References

[1] T. Fukuda *et al.*, *Mater. Trans.*, **45** (2004) 188.

[2] F. C. Nix and D. MacNair, *Phys. Rev.*, **60** (1941) 597.

[3] Ch. E. Guillaume and C. R. Acad. *Sci. Paris.*, **125** (1987) 235.

[4] M. Matsui *et al.*, *J. Magn. Magn. Mater.*, **15-18** (1980) 1201.

[5] M. Sugiyama, R. Oshima, F. E. Fujita, *Trans. JIM.* **25** (1984) 585.

[6] G. P. Johari, J. G. McAnanama and G. Sartor, *Phil. Mag. B.*, **74** (1996) 243.

[7] J. Cui, T. W. Shield, R. D. James, *Acta Mater*, **52** (2004) 35.

Chapter 3

Large elastic-like deformation in the Fe-31.2Pd (at.%) single crystals

3.1 Introduction

As introduced in chapter 1, a large elastic-like deformation with low Young's modulus is expected to be obtained in an Fe-Pd single crystal because of the lattice softening in the parent phase and continuous change of lattice parameter in the martensite phase. In this chapter, we check this behavior by compressing the Fe-31.2Pd (at.%) single crystals in the $[001]_P$ direction. The structure change under stress is studied. The largest elastic strain and defects in the plastically deformed specimens are also investigated.

3.2. Experiments

3.2.1 Specimen preparation

Fe-31.2Pd (at.%) single crystals were prepared by the method mentioned in chapter 2. Parallelepiped specimen composed of $(100)_P$, $(010)_P$ and $(001)_P$ planes with a size of $3.4\ mm \times 3.4\ mm \times 11.4\ mm$ and $2.4\ mm \times 2.3\ mm \times 6.6\ mm$ were cut from the single crystals. After homogenization at 1375 K for 24 h, the specimens for compressive testing were quenched in ice water to keep the disordered parent phase. The FCC-FCT MT temperature of the present

31.2Pd (at.%) specimen was approximately 230 K, being the same temperature as mentioned in chapter 2.

3.2.2 Compressive tests

Compressive tests of Fe-Pd single crystals were performed using a SHIMADZU AG-I 50kN MODEL M1 at a strain rate of 5×10^{-5} s^{-1}. This strain rate is selected to ensure isothermal conditions. During the compressive tests, the specimen was mounted in a dice and stress was applied to the specimen through a piston as shown in Fig. 3.1(a). The longitudinal strain ε_{33} in the $[001]_P$ direction and transverse strain ε_{11} in the $[100]_P$ (or $[010]_P$) direction were measured by strain gages (KYOWA, KFL-02-120-C1-11) as shown in Fig. 3.1(b). The strain gages were stuck on the surface of the specimen by a PC-6 glue.

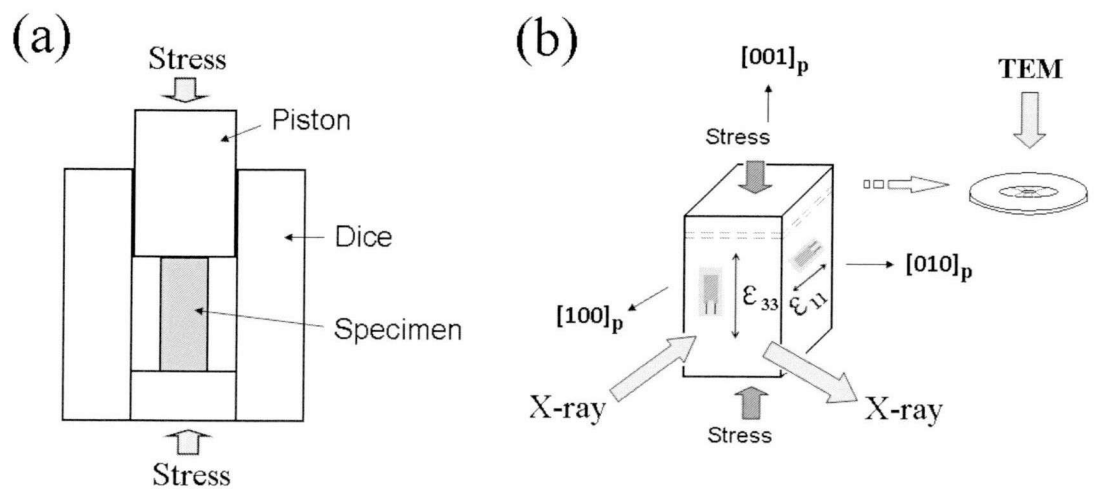

Fig. 3.1. Arrangement of the specimen in (a) compressive tests and (b) *in-situ* XRD and TEM.

The strain gage is connected with a DB-120P bridge box through a Wheatstone bridge circuit as shown in Fig. 3.2. The strain ε can be evaluated from the electric resistance change of the strain gage ΔR :

$$\varepsilon = \frac{\Delta l}{l_0} = \frac{\Delta R}{K \cdot R}, \tag{3.1}$$

where l_0 is the length of the specimen, Δl is the length change of specimen, K is the constant factor and R is the electric resistance of the strain gage. The small change of electric resistance is indicated by an amplified output voltage by a DYNAMIC STRAIN AMPLIFIER (DPM-711B). The strain ε and the output voltage e_0 have a relationship as:

$$e_0 = \frac{1}{4} K \varepsilon E = \frac{1}{B} \varepsilon E, \tag{3.2}$$

where E is the bridge voltage (input), B is the calibration coefficient when the bridge voltage E=1 V and output voltage $e_0 = 1$ μV. In the present study, the coefficient is 5×10^{-3}. Due to the limitation of the strain gage, the strain over 4% was obtained by calibrating the crosshead displacement.

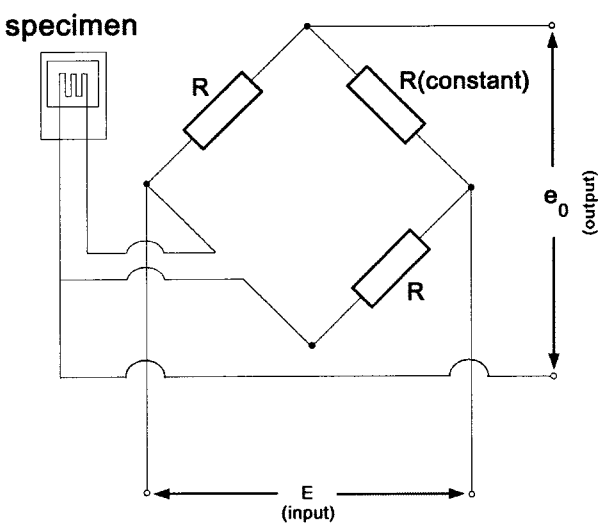

Fig. 3.2 Wheatstone bridge for the measurement of a strain by one-gage method.

3.2.3 Structural investigation

The change in crystal structure under stress was monitored by an *in-situ* XRD using Cu-K_α radiation. The compressive direction is $[001]_P$ and the reflection plane of the X-ray is $(200)_P$

(or $(020)_P$) as shown in Fig. 3.1(b). After a plastic deformation, the surface relief was observed under an optical microscope. The structure of the specimen after the plastic deformation was also measured by XRD at 300 K. Defects in the plastically deformed specimen were studied by a transmission electron microscope (TEM). Disks for TEM observation were spark cut from the plastically deformed specimen such that the face normal was close to the $[001]_P$ direction. Thin foils were then prepared by jet-polished in an electrolyte composed of 85% acetic acid and 15% perchloric acid at 280 K. TEM observations were made at room temperature using a HITACHI H-800. The operation was made at an accelerating voltage of 200 kV.

3.3. Results

3.3.1 Elastic-like deformation

Figure 3.3 shows stress-strain curves of the Fe-31.2Pd (at.%) single crystal compressed in the $[001]_P$ direction up to 100 MPa at the fixed temperatures indicated in the figure. The uniaxial stress σ_{33} are plotted as a function of the longitudinal strain ε_{33} in the $[001]_P$ direction (Fig. 3.3(a)) and the transverse strain ε_{11} in the $[100]_P$ (or $[010]_P$) direction (Fig. 3.3(b)). Noted that σ_{33} and ε_{33} are negative values, while ε_{11} is a positive value in compressive tests. The strains ε_{33} and ε_{11} are reversible and exhibit quite small stress hysteresis (less than 4 MPa), and the strains increase with decreasing temperature. The small stress hysteresis may have been caused by the friction between the dice and piston used for measurement. At 240 K (near the transformation temperature), the strains $|\varepsilon_{33}|$ and ε_{11} under stress of 100 MPa reach 3.7% and 1.6%, respectively. At 240 K, relatively flat "plateau" appear in the stress-strain curves in the region from 4 MPa to 12 MPa extending across a strain of 1.2%

in $|\varepsilon_{33}|$ and that with a strain of 0.7% in ε_{11} as indicated by dashed lines in the figure. These strains are regarded as transformation strains, which we further described in section 3.4.2. Poisson's ratios ($|\varepsilon_{11}/\varepsilon_{33}|$) was calculated to be approximately 0.4 at all temperatures.

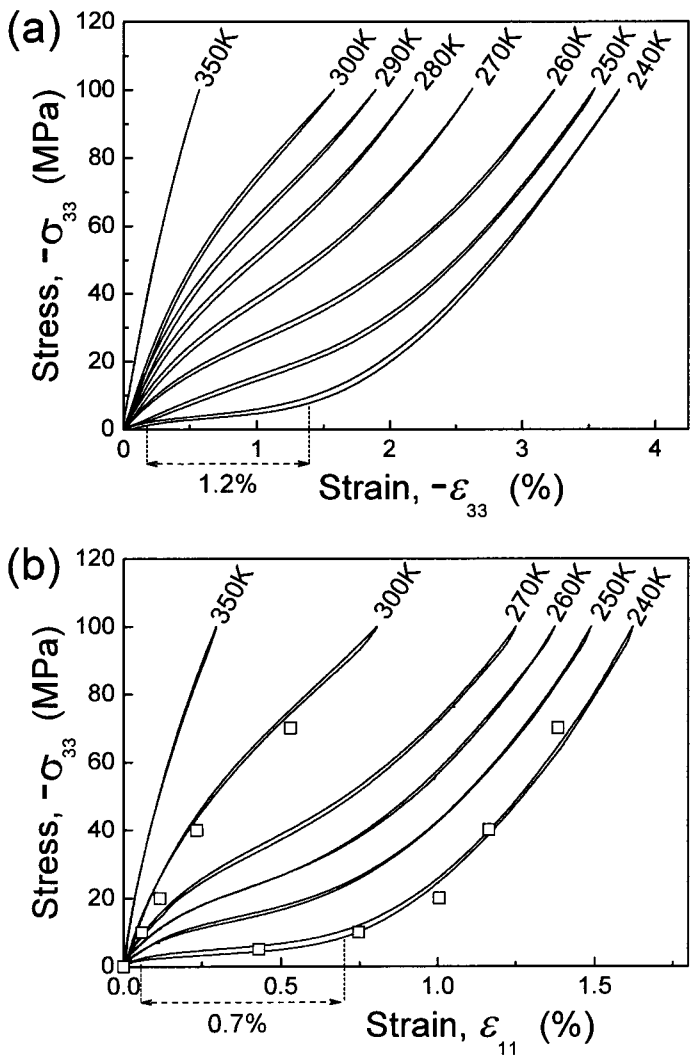

Fig. 3.3. Stress-strain curves of the Fe-31.2Pd (at.%) single crystal compressed in the $[001]_P$ direction at different fixed temperatures: (a) longitudinal strain $-\varepsilon_{33}$ versus the applied stress $-\sigma_{33}$ and (b) transverse strain ε_{11} versus the applied stress $-\sigma_{33}$. The ranges of dashed lines indicate the transformation strains at 240 K. The square marks in (b) represent the strains calculated from *in-situ* XRD.

Figure 3.4 presents the stress-strain curves of the Fe-31.2Pd (at.%) single crystal compressed in the $[001]_P$ direction up to 100 MPa at 226 K (a) and 126 K (b) (below the transformation temperature 230 K). The solid line presents loading and unloading processes of the fist cycle, and the dashed line is that of the second cycle. It is found that there is unrecovered strain after the first cycle. This is attributed to the difference in the fractions of three martensite variants between loading and unloading processes. It should be noted that, in the first cycle, the stress-strain in the unloading process is different from that of the conventional SMAs where the strain decreases almost linearly with decreasing the applied stress. The large recoverable strain in the Fe-Pd single crystal in the loading process may be attributed to the rotation of the magnetic domain accompanied with structural change or the experimental error of strain gages. In the second cycle, the strain becomes almost recoverable due to the single martensite variant in both processes. This behavior will be further discussed in section 3.3.2. The reversible stains at 226 K and 126 K under stress of 100 MPa in the second cycle reach approximately 3% and 2.2%, respectively.

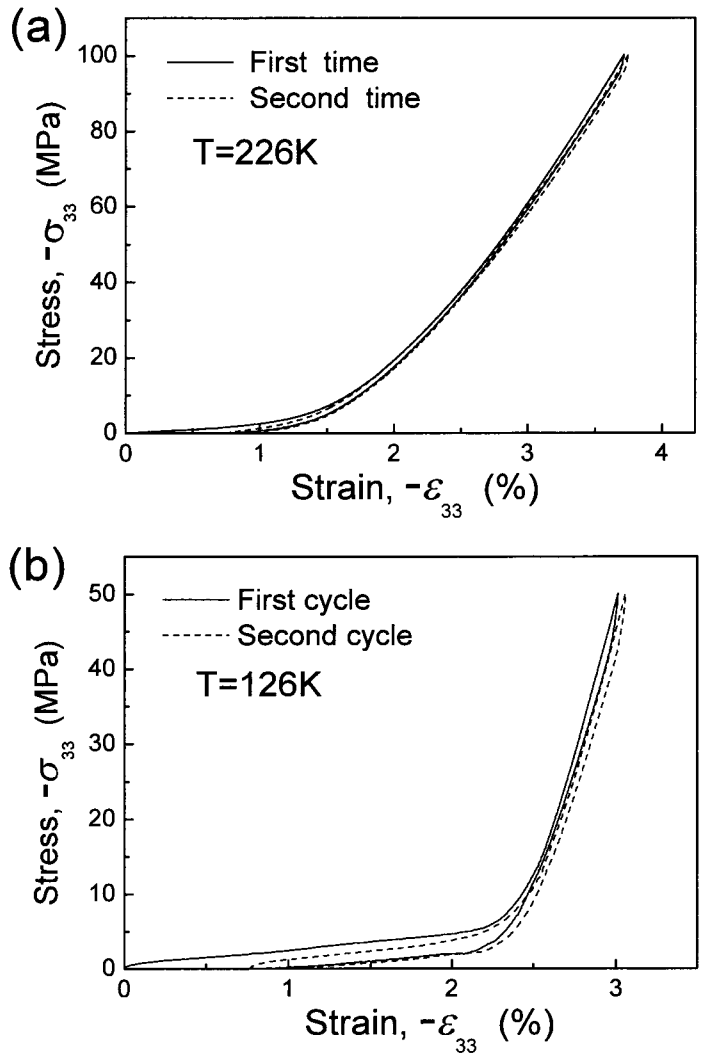

Fig. 3.4. Stress-strain curves of the Fe-31.2Pd (at.%) single crystal compressed in the $[001]_P$ direction at 226 K (a) and 126 K (b), where the solid line is the first cycle of loading and unloading process and the dash line is the second cycle.

From the results in Fig. 3.3(a) and 3.4, the Young's modulus in the $[001]_P$ direction $E_{[001]_P}$ is evaluated as a function of temperature as shown in Fig. 3.5. It should be noted that the Young's modulus above the transformation temperature is evaluated at the start point of the stress-strain curves, and that below the transformation temperature is evaluated from the linear part at the high stress region of the stress-strain curves. The $E_{[001]_P}$ in the parent phase significantly decreases with decreasing temperature, where its value is approximately 12.6 GPa

at 300 K and 1.5 GPa at 240 K. This behavior is consistent with the temperature dependence of the elastic constant C' [1]. In addition, the $E_{[001]_P}$ at 240 K is nearly two orders in magnitude lower than that of conventional metals such as copper (180 GPa) [2] and even one order in magnitude lower than that of polymer materials such as nylon (3 to 10 GPa) [3].

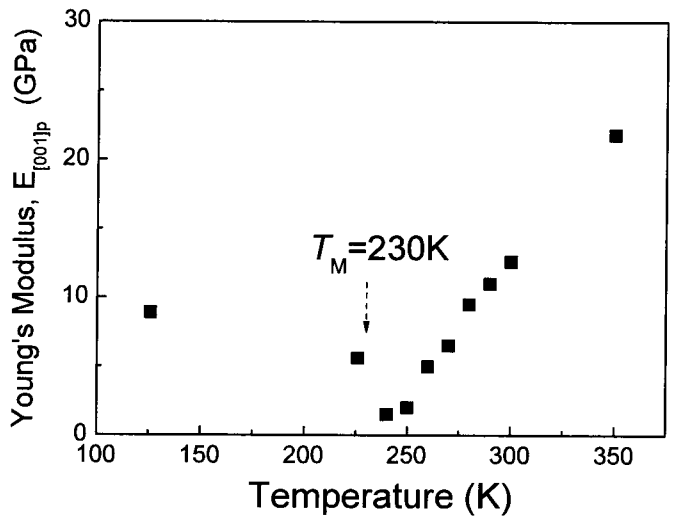

Fig. 3.5. The Young's modulus of the Fe-31.2Pd (at.%) single crystal in the $[001]_P$ direction $E_{[001]_P}$ as a function of temperature.

3.3.2 Crystal structure under a uniaxial stress

The results of XRD measurements under various different compressive stresses at 300 K, 240 K and 226 K using the method described in section 3.2.2 are shown in Figs. 3.6(a), (b) and (c). Peaks in the profiles correspond to (200) of the Fe-Pd single crystal.

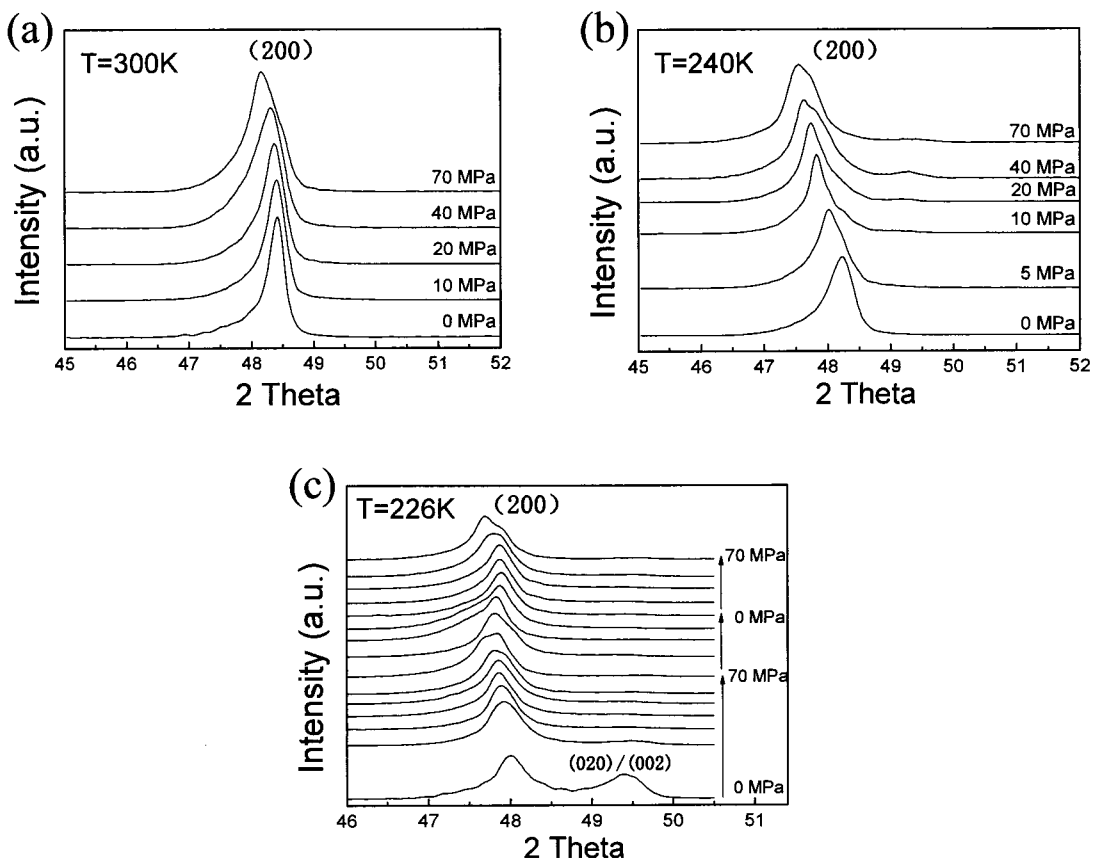

Fig. 3.6. The change of XRD spectra of the Fe-31.2Pd (at.%) single crystal under compressive stress in the $[001]_P$ direction at 300 K (a), 240 K (b) and 226 K (c).

At 300 K (Fig. 3.6(a)), the peak position gradually shifts to a lower angle with increasing the applied stress and no other peak appears. This result implies that no first-order MT occurs at 300 K under the stress up to 70 MPa. This shift of peak is attributed to the expansion of the specimen in the $[100]_P$ and $[010]_P$ directions, which are perpendicular to the compressive direction. The corresponding lattice parameter, *a*, calculated from the peak position is plotted as solid triangles in Fig. 3.7 with solid square.The lattice parameter increases almost linearly with increasing the applied stress. In terms of symmetry, however, the specimen changes from a cubic structure to a tetragonal structure and the lattice distortion gradually increases with increasing the applied stress, as further discussed in section 3.4.1.

At 240 K (Fig. 3.6(b)), the peak position also gradually shifts to a lower angle with

increasing the applied stress. The corresponding lattice parameter, a, calculated from the XRD profile is plotted as solid triangles in Fig. 3.7. The increase in the lattice parameter is particularly large below 20 MPa, where the stress-induced MT should occur. However, the peak separation expected from the coexistence of the parent phase and the martensite phase is not clearly observed in this range possibly due to the broadness of the peak. When the applied stress is 20 MPa and higher, the lattice parameter increases almost linearly with increasing applied stress, which is caused by the elastic deformation in a single martensite variant. Incidentally, a small peak appearing near 2θ=49.3° under applied stress of 40 MPa is thought to originate from other martensite variants, and may have been caused by inhomogeneous stress in the specimen during the XRD measurement.

Values of ε_{11} were calculated from the change in the lattice parameter under uniaxial stress at 300 K and 240 K shown in Fig. 3.7 and are plotted in Fig. 3.3(b) square marks. The good agreement between the values obtained by X-ray measurement and the results of compressive tests confirms that the strains in Fig. 3.3 are essentially due to the continuous change in the lattice parameter.

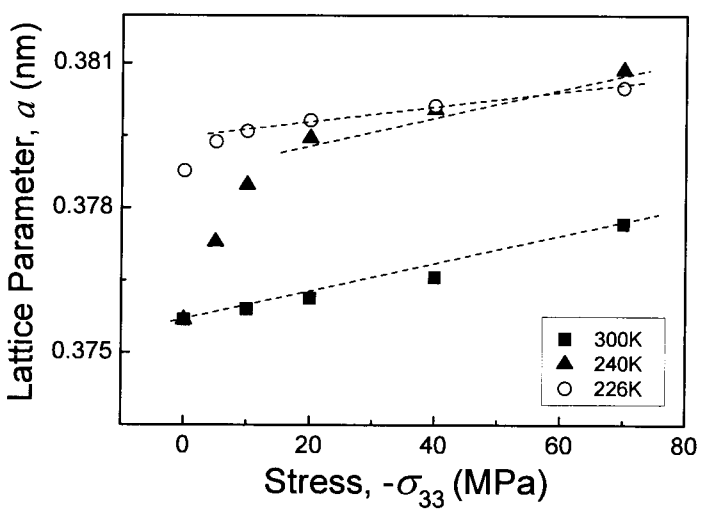

Fig. 3.7. The lattice parameter, a, of the Fe-31.2Pd (at.%) single crystal as a function of the compressive stress in the $[001]_P$ direction at 300 K, 240 K and 226 K.

At 226 K (Fig. 3.6(c)), two peaks appears under zero applied stress due to the multi martensite variants below the transformation temperature (230 K). The peak in the right hand corresponds to the (020)/(002) of the martensite variants with the long-axis in the compressive direction, and that in the left hand is the (200) of the martensite variant with the short axis along the compressive direction. With increasing the applied stress, the (020)/(002) peak gradually disappears due to the reduction of variants responsible for the peak. This behavior explains the unrecoverable strain in the first cycle of Fig. 3.4(a). The position of (200) peak shifts to a lower angle with increasing the applied stress, and gradually returns back to the origin position in the unloading process. In the second loading process, there is only a single martensite variant, which is similar to that above the transformation temperature. The corresponding lattice parameter, a, calculated from the XRD profile in the first loading process is also marked in Fig. 3.7 as a circle. The lattice parameter a increases almost linearly after 10 MPa, which explains the elastic-like deformation in the second cycle shown in Fig. 3.4(a).

3.3.3 Largest reversible strain and plastic deformation

In order to investigate the largest reversible strain in the Fe-Pd single crystal in the $[001]_P$ direction, higher stress is applied at 240 K. At a stress of 250 MPa, the reversible strain was 6.5% with a quite small stress hysteresis as seen in Fig. 3.8(a). The yield point appears at 285 MPa at a strain of 7.3% as shown in Fig. 3.8(b), with residual strain of approximately 2.7% obtained after removing the stress. This was not recovered by heating back to 300 K which is 70 K above the transformation temperature. However, when the specimen is annealed at 1273 K for 12 h, the residual strain reduced to 1.4%. In other words, part of the residual stress (1.3%) was recovered by annealing. In order to understand this behavior, the structure of the plastically deformed specimen is studied by an XRD. The X-ray reflection plane is (200) (or (020)) and measurement temperature is 300 K. The results are shown in Fig. 3.9 with the processes applied to the specimens shown beside each figure.

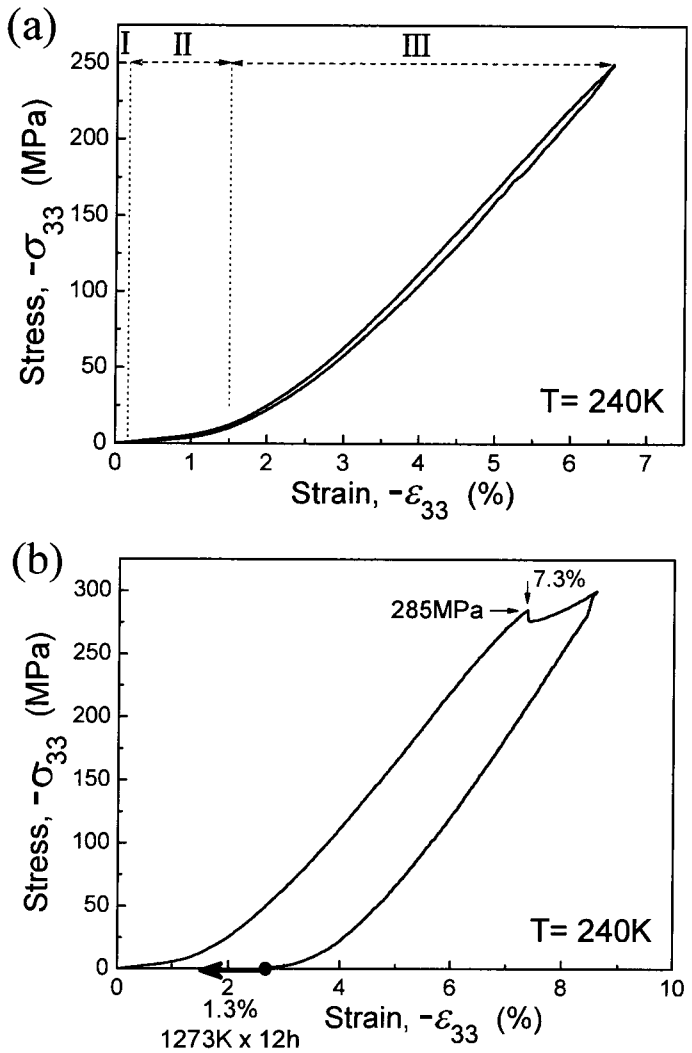

Fig. 3.8. The stress-strain curve of the Fe-31.2Pd (at.%) single crystal under compressive stress in the $[001]_P$ direction at 240 K up to 250 MPa (a) and 300 MPa (b). The arrow in (b) indicates the recovery strain (1.3%) by annealing at 1273 K for 12 h.

The structure of the specimen before the deformation at 300K is the parent phase (FCC structure) as shown in Fig. 3.9(a). After the loading and unloading processes at a compressive stress of 300 MPa at 240 K, the structure of the specimen was measured again at 300 K. The peak was found to shift to a lower angle as shown in Fig. 3.9(b). This means that the FCT structure remains at 300 K even though this is 70 K higher than the transformation temperature. The remaining FCT structure is probably due to stabilization of the FCT phase by residual

internal stress in the plastically deformed specimen. After annealing at 1273 K for 12 h, the FCT structure returns back to the FCC structure as shown in Fig. 3.9(c). From the shift in the peak position between Figs. 3.9(b) and (c), the recovered strain in the $[100]_P$ (or $[010]_P$) direction is calculated to be approximately 0.6%. Taking Poisson's ratio (0.4) into account, the recovered strain in the $[001]_P$ direction is estimated to be approximately 1.5%, which is consistent with the actual recovered strain of 1.3% shown in Fig. 3.8(b). From the peak position in Fig. 3.9(b) and the stress-strain curves at 300 K in Fig. 3.3(b), the typical value of residual internal stress after plastic deformation is estimated to be approximately 40 MPa at room temperature.

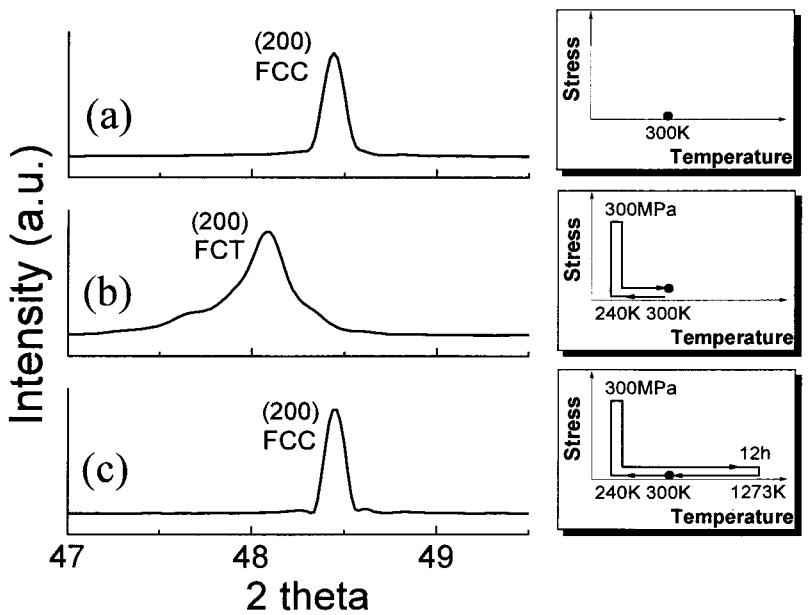

Fig. 3.9. XRD profile of the Fe-31.2Pd (at.%) single crystal at 300 K: (a) before compressive test; (b) after plastic deformation at 240 K; (c) after annealing the plastically deformed specimen at 1273 K for 12 h.

Figure 3.10 shows the stress-strain curve compressed in the $[001]_P$ direction up to 450 MPa at 300 K. A yield point appears at approximately 310 MPa at a strain approximately 4.6%. The defects in these plastically deformed specimens at 240 K and 300 K are further investigated in section 3.3.4.

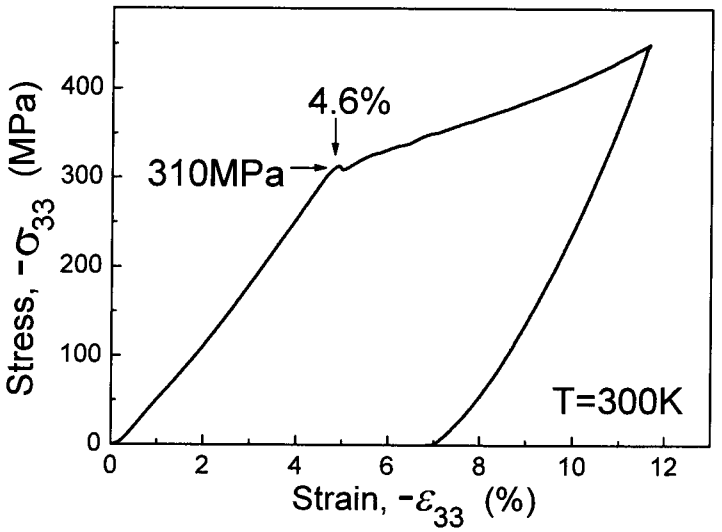

Fig. 3.10. The stress-strain curves of the Fe-31.2Pd (at.%) single crystals compressed in the $[001]_P$ direction at 300 K.

3.3.4 Observation of defects

Figure 3.11 shows a sketch of a plastically deformed specimen (after compression of 300 MPa at 240 K) and images of the surface reliefs observed by optical microscope at room temperature. Parallel traces are apparent on the surface of the plastically deformed specimen. A two-surface trace analysis suggests that the plastic deformation occurs on {111} planes. The result of the plastically deformed specimen (after compression of 450 MPa at 300 K) is similar to that at 240 K shown in Fig. 3.11.

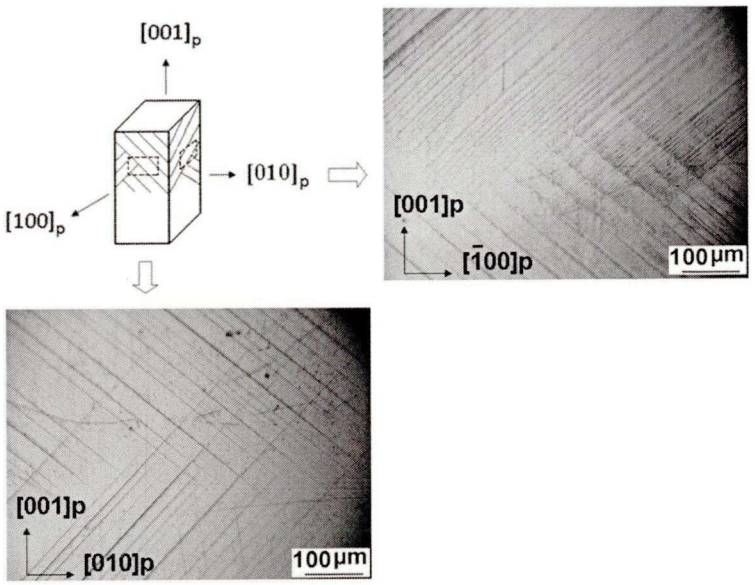

Fig. 3.11. A simple sketch of the plastically deformed Fe-31.2Pd (at.%) single crystal (after compression of 300 MPa at 240 K) and the surface reliefs observed by an optical microscope.

To study details of the defects, the plastically deformed specimen (at 240 K) was investigated by TEM. Figure 3.12(a) shows a typical bright-field image of a deformed region, with (b) and (c) showing diffraction patterns taken in the vicinity of the regions indicated by B and C, respectively. The selected-area diffraction (SAD) pattern in Fig. 3.12(b) indicates that the matrix area (B) has a FCC structure for the beam direction of $[114]_P$. Near the band area (C), the twin pattern for the beam direction of $[110]_T$ appears overlapped with the pattern of the matrix as shown in Fig. 3.12(c), which is identical to the simulated electron diffraction pattern of (111) twin in FCC crystal structure [4]. The dark-field image shown in Fig. 3.12(d) taken by using the $(\bar{1}11)_T$ reflection confirms the twinned structure in the band area. The thickness of the twinned band is approximately 200 to 300 nm with twin boundary $(111)_P$, which is consistent with the trace observed by optical microscope shown in Fig. 3.11. Although the XRD profile after the plastic deformation exhibits a FCT profile (Fig. 3.9(b)), most part of the specimen is FCC in the TEM specimen. The reason for the disappearance of the FCT structure

in the TEM specimen is probably because the internal stress was relieved through the process of preparing the TEM specimen, with the FCT structure relaxing back to the FCC structure. In addition to the twinned structure, perfect dislocations are also observed as shown in Fig. 3.13(a). The Burgers vector of the dislocation was determined to be $a/2<110>$ by a contrast analysis. The contrast obtained by exciting $(2\bar{2}0)_P$ is shown in Fig. 3.13(b) as an example. This $a/2<110>$ is a conventional Burgers vector for FCC materials.

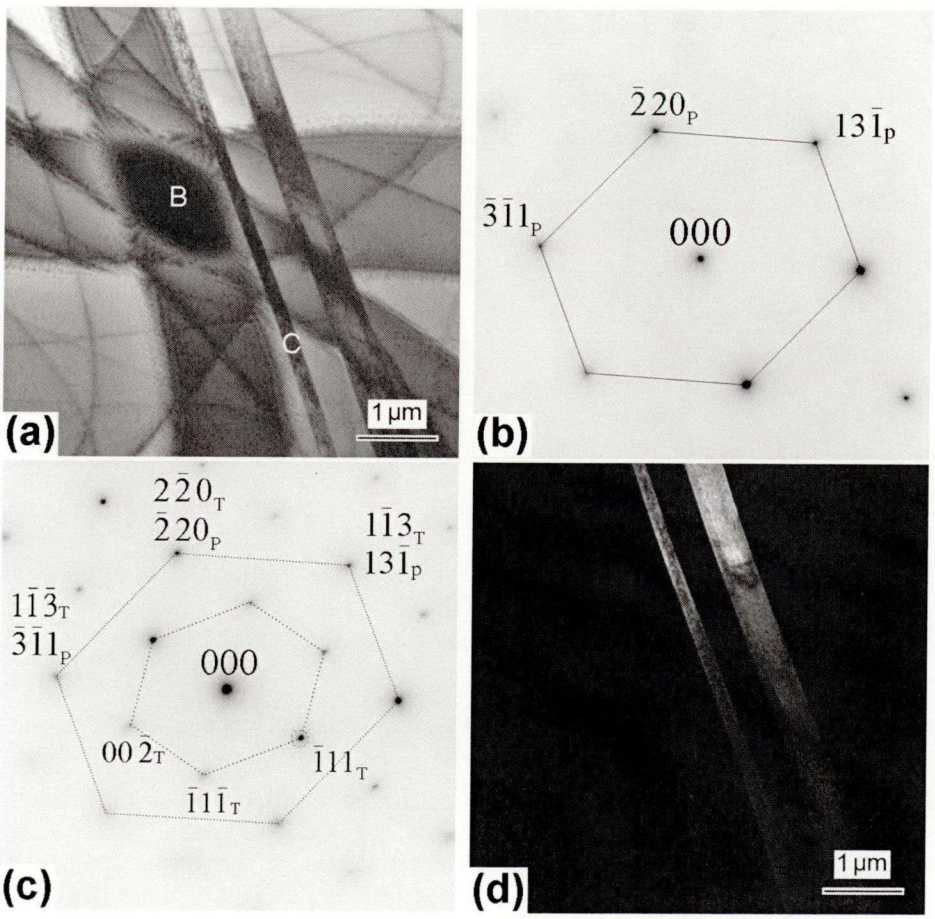

Fig. 3.12. TEM micrograph of a typical plastically deformed (after compression at 240 K) area: (a) bright field image; (b) selected-area diffraction pattern from matrix area B; (c) selected-area diffraction pattern from twinned band area C; (d) dark image of the twinned region taken by using $(\bar{1}11)_T$ reflection marked by a circle.

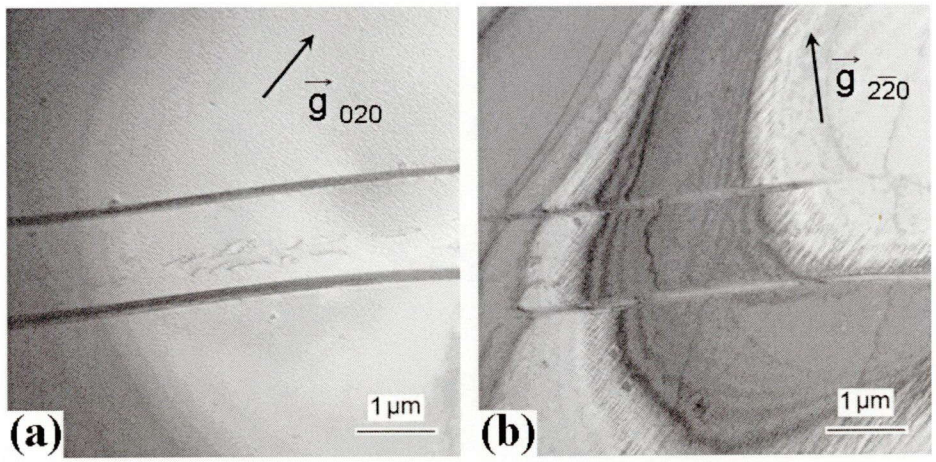

Fig. 3.13. Dislocations near the twinned bands (plastically deformed at 240 K). (a) is taken by exciting $(200)_P$ reflection, and (b) is taken by exciting $(2\bar{2}0)_P$ reflection.

Figure 3.14(a) shows TEM results for a heavily deformed area. Two characteristic regions indicated by B and C can be seen with region B characterized by parallel bands and the region C by zigzag bands. The SAD pattern of region B shown in Fig. 3.14(b) is indexed as the FCT structure for the beam direction of $[121]_{FCT}$. In the tetragonal structure, the angle between $(20\bar{2})_{FCT}$ and $(\bar{1}1\bar{1})_{FCT}$ reflections is given by

$$\cos\theta = \frac{1-(c/a)^2}{\sqrt{(1+(c/a)^2)(2+(c/a)^2)}}, \tag{3.3}$$

where a and c are the lattice parameters of the martensite phase. In the present case, the angle θ is approximately 92°. Using the equation (3.3), the tetragonality c/a is calculated to be approximately 0.96, which is consistent with the XRD results in Fig. 3.9(b).

Incidentally, the SAD pattern from the region C (zigzag bands) in Fig. 3.14(c) is indexed by the BCC structure with the beam direction of $[111]_{BCC}$. However, the BCC structure is not detected in the deformed specimen by XRD (Fig. 3.9(b)). This may be attributed the BCC region having a small volume fraction.

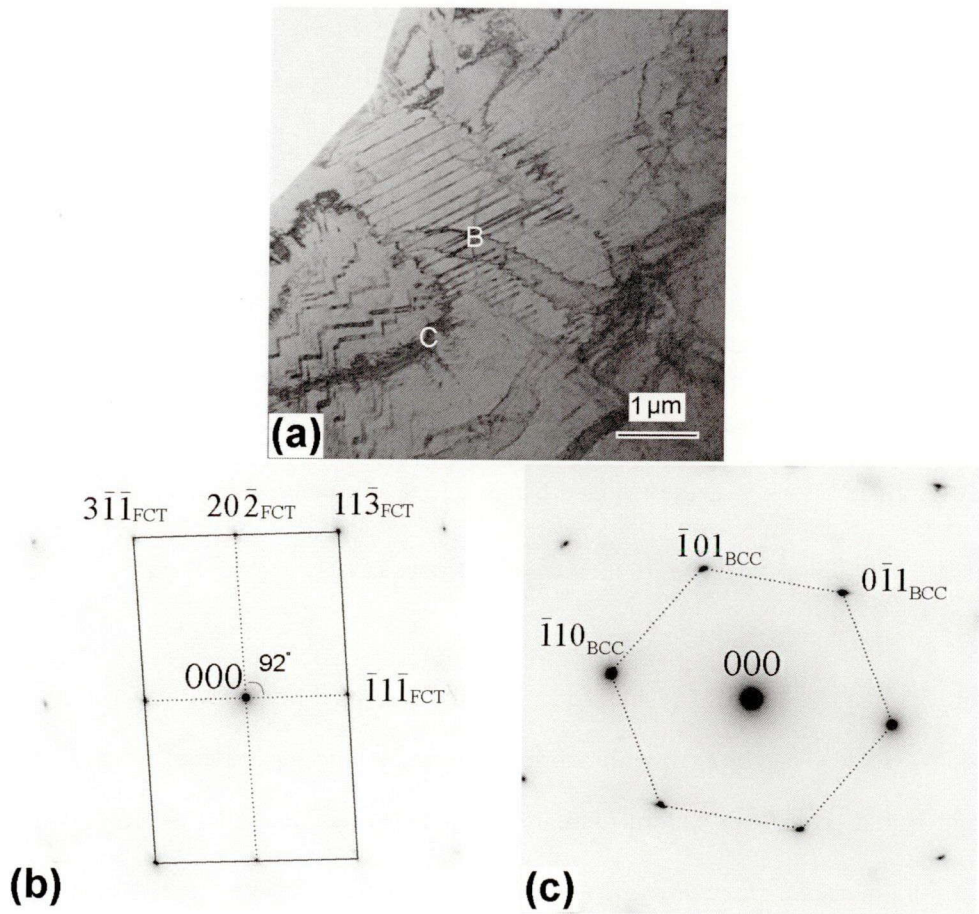

Fig. 3.14. TEM observation of a heavily plastically deformed (at 240 K) area: (a) bright-field image; (b) selected-area diffraction pattern of FCT structure from the area B; (c) selected-area diffraction pattern of BCC structure from the area C.

The main defect in the deformed specimen (at 300 K) is also the mechanical twinning $\{111\}/\frac{1}{6}<112>$. Figure 3.15(a) is a typical bright-field image of a deformed region, and (b) and (c) are diffraction patterns taken in the vicinity of the regions indicated by B and C, respectively. The selected-area diffraction (SAD) pattern in Fig. 3.15(b) indicates that the matrix area (B) has FCC structure for the beam direction of $[114]_P$. Near the band area (C), the twin pattern for the beam direction of $[110]_T$ appears overlapped with the pattern of the matrix as shown in Fig. 3.15(c). The dark-field image in Fig. 3.15(d) taken by using $(\bar{1}11)_T$ reflection confirms the twinned structure in the band area. The perfect dislocation is also observed as shown in Fig.

3.16. The Burgers vector of the dislocation is determined to be $a/2<110>$, which is similar to the results of the plastically deformed specimen (after compression at 240 K).

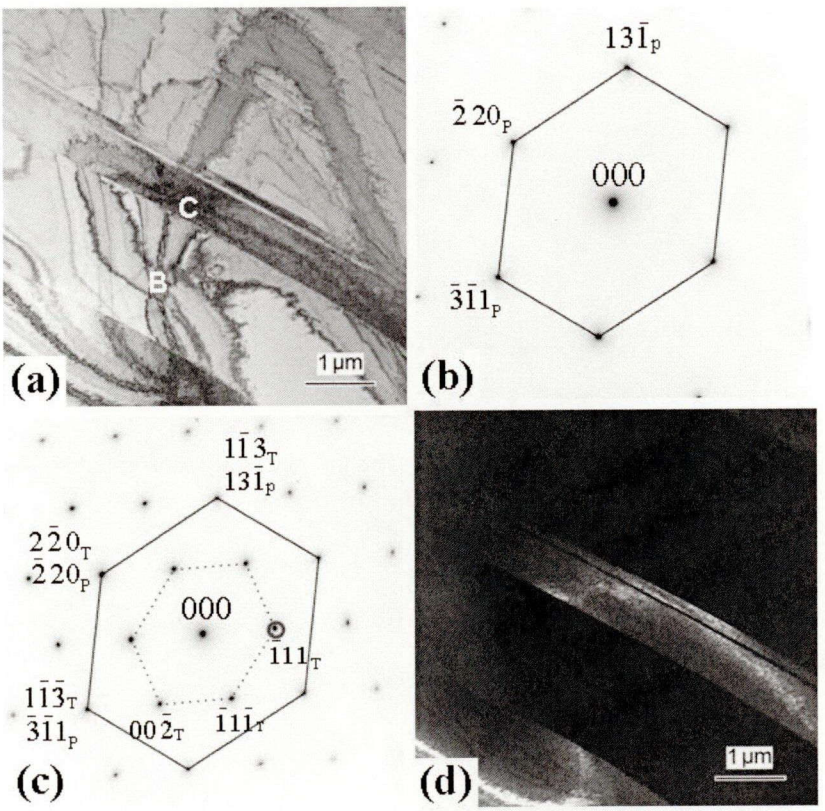

Fig. 3.15. TEM micrograph of a typical plastically deformed (after compression at 300 K) area: (a) bright field image; (b) selected-area diffraction pattern from matrix area B; (c) selected-area diffraction pattern from twinned band area C; (d) dark image of the twinned region taken by using $(\bar{1}11)_T$ reflection marked by a circle.

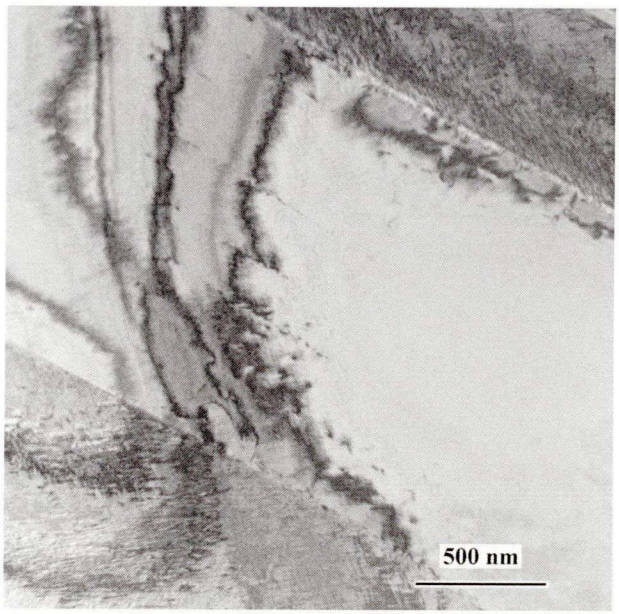

Fig. 3.16. Dislocations near the twinned bands (after the plastically deformed at 300 K).

3.4. Discussion

3.4.1 Transformation strain and elastic strain

In most metals, the elastic deformation persists up to a strain of only approximately 0.5% [5]. In an Fe-31.2Pd (at.%) single crystal, however, a large elastic-like strain of more than 6% was observed in the present study. To understand this behavior, the stress-strain curves in Fig. 3.3(a) were further analyzed. Young's modulus (or the modulus of elasticity) is usually determined from the initial slope of a stress-strain curve. However, since the slope varies significantly with stress in an Fe-Pd single crystal the values of $d\sigma_{33} / d\varepsilon_{33}$ in Fig. 3.3(a) at 300 K and 240 K are evaluated as a function of the applied stress $-\sigma_{33}$. Calculations are made on the loading process with the results shown in Fig. 3.17.

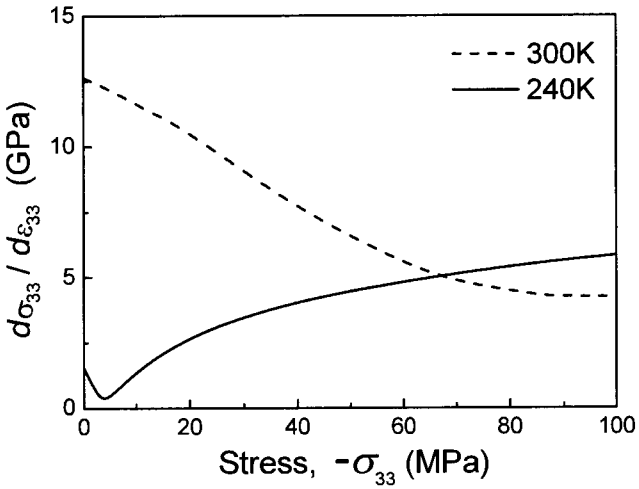

Fig. 3.17. The value of $d\sigma_{33}/d\varepsilon_{33}$ calculated from Fig. 3.2(a) as a function of the applied stress $-\sigma_{33}$ at 300 K and 240 K.

The initial value of $d\sigma_{33}/d\varepsilon_{33}$ can be regarded as the Young's modulus in the $[001]_P$ direction $E_{[001]_P}$, which has been discussed in section 3.31. At 240 K, the value of $d\sigma_{33}/d\varepsilon_{33}$ initially decreases with increasing applied stress, then exhibits a minimum near 4 MPa, and begins increaseing. The decrease in $d\sigma_{33}/d\varepsilon_{33}$ has also been reported in Cu-Al-Ni SMAs [6], and this behavior was interpreted as the stress-induced lattice softening of the parent phase. The increase in $d\sigma_{33}/d\varepsilon_{33}$ after the minimum is a property of the stress-induced martensite phase. Although it is not easy to exactly determine the start stress for inducing MT, the value is expected to be a little lower than the stress where $d\sigma_{33}/d\varepsilon_{33}$ exhibits the minimum (4 MPa). This critical stress is much lower than that of conventional SMAs. For example, the stress for that induces MT in a Ni-Ti alloy is approximately 100 to 300 MPa (at 10 K above A_f) [7,8], which is much higher than the present result. At 300 K, the value of $d\sigma_{33}/d\varepsilon_{33}$ decreases monotonically with increasing applied stress. This result implies that no stress-induced MT occurs at this temperature, but that softening of the parent phase does occurs. Consequently, the tetragonal structure at 300 K under compressive stress up to 100 MPa should be regarded as the elastically deformed parent phase. The agreement between the elastic strain obtained from the

strain gage (Fig. 3.3(b)) and from *in-situ* XRD (Fig. 3.6(a)) also supports the elastic deformation of the parent phase.

Considering the dependence of $d\sigma_{33}/d\varepsilon_{33}$ on applied stress, we can classify the large elastic-like strains at 240 K in Figs. 3.3 and 3.8(a) into three parts: (I) the elastic strain of the parent phase, (II) the transformation strain and (III) the elastic strain of the martensite phase. From the start point ($|\sigma_{33}| = 0$ MPa) to the starting stress for inducing MT ($|\sigma_{33}| \approx 4$ MPa), the specimen undergoes the elastic deformation in the parent phase. Due to the quite low value of the critical stress for inducing MT at 240 K, the elastic strain in the parent phase is small ($|\varepsilon_{33}| \approx 0.2\%$ and $\varepsilon_{11} \approx 0.1\%$) despite the small value of Young's modulus in the $[001]_P$ direction.

When the applied stress exceeds the start stress for inducing MT, the stress-induced martensite phase appears. The coexistence of two phases detected by an *in-situ* XRD confirms the stress-induced MT. The transformation strains $|\Delta\varepsilon_{33}|$ and $|\Delta\varepsilon_{11}|$ evaluated from Fig. 3.3 was approximately 1.2% and 0.7%, respectively. The transformation strains can also be calculated from the change in the lattice parameters at the transformation temperature as

$$|\Delta\varepsilon_{33}| = (a_0 - c)/a_0 \quad \text{and} \quad |\Delta\varepsilon_{11}| = (a - a_0)/a_0, \tag{3.4}$$

where a_0 is the lattice parameter in the parent phase, and a and c are the lattice parameters in the martensite phase. Temperature dependence of the lattice parameters of an Fe-31.2Pd (at.%) alloy [9] is shown in Fig. 3.18. Near the transformation temperature, the lattice parameter $a = 0.3787$ nm, $c = 0.3709$ nm and $a_0 = 0.3759$ nm, and the calculated result of $|\Delta\varepsilon_{33}|$ and $|\Delta\varepsilon_{11}|$ are approximately 1.3% and 0.8%, respectively. These values are consistent with the ranges of the relatively flat "plateaus" in the stress-strain curves in Fig. 3.3.

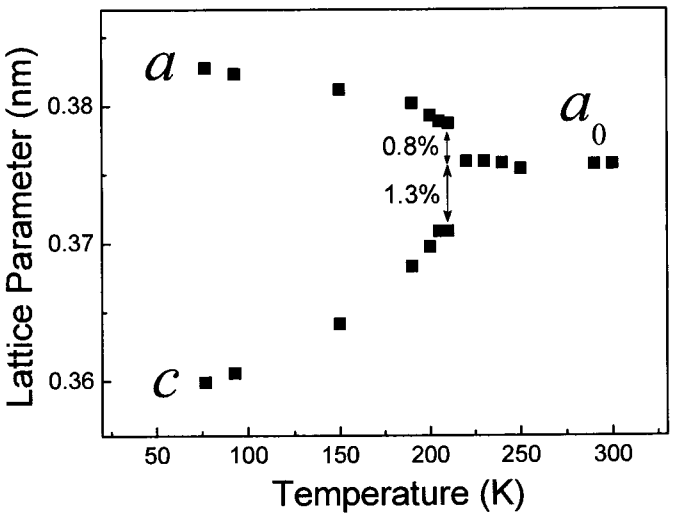

Fig. 3.18. Temperature dependence of the lattice parameter of an Fe-31.2Pd (at.%) alloy [9].

After the transformation strains, the large reversible strains with negligible stress hysteresis appears. They are caused by the elastic deformation in the martensite phase. The agreement between the elastic strains obtained from the strain gage (Fig. 3.3(b)) and from an *in-situ* XRD (Fig. 3.6(b)) confirms the elastic deformation of a single martensite variant. The continuous increase in lattice distortion ($1-c/a$) with increasing the applied stress in the single martensite variant is essential for the large elastic-like strain. As the applied stress increases the elastic strain of the martensite phase reaches approximately 5% as shown in Fig. 3.8(a).

In conventional SMAs that have a typical first order MT, the reversible strain mainly comes from the transformation strain (II). In the present case, however, the large reversible strain mainly comes from the elastic strain in the martensite phase (III). In addition, compared with other SMAs such as Ti-Ni [7,10] and Fe-Ni-Co-Al-Ta-B alloys [11] exhibiting a typical first-order MT, the stress hysteresis in the stress-strain curves of Fe-Pd single crystal is negligibly small. This means the energy dissipation during the loading and unloading process is extremely small, which is characteristic to an elastic deformation.

3.4.2 Near-ideal shear strength

TEM observation (Fig. 3.11 and 3.15) of the plastically deformed Fe-Pd single crystals has revealed that the plastic deformation is mainly caused by the mechanical twinning with the $\{111\}/\frac{1}{6}<112>$ deformation system. Mechanical twinning is frequently observed in FCC metals at cryogenic temperatures and low strain rates [12,13]. However, this kind of large elastic-like strain is rarely observed in metallic materials except for some whiskers [14,15] or nanoscale materials [16]. In these materials, the shear strengths are reported to be close to the ideal values. In the following, we compare the shear strength of the Fe-31.2Pd (at.%) single crystal with the ideal shear strength.

The critical resolved shear stress τ_{CRSS} is given by the Schmid's law

$$\tau_{CRSS}=\sigma_Y \cos\phi\cos\lambda, \tag{3.5}$$

where σ_Y is the yield stress and $\cos\phi\cos\lambda$ is Schmid factor. The yield stress of an Fe-31.2Pd (at.%) single crystal in the $[001]_P$ direction at 240 K and 300 K is 285 MPa and 310 MPa, respectively. In the present study, the plastically deformed specimen is tetragonal structure, and the Schmid factor for the $\{111\}/\frac{1}{6}<112>$ deformation system is given by

$$\cos\phi\cos\lambda=\frac{\sqrt{2}(c/a)}{(2(c/a)^2+1)}, \tag{3.6}$$

where the tetragonality *c/a* of the plastically deformed Fe-31.2Pd (at.%) single crystal at 240 K and 300 K is evaluated to be approximately 0.89 and 0.93, respectively. Then τ_{CRSS} at 240 K and 300 K is calculated to be 139 MPa and 149 MPa, respectively.

The ideal shear stress τ_{IDEAL} of a perfect Fe-Pd single crystal is give by the Frenkel model as [17]

$$\tau_{IDEAL}=\frac{Gb}{2\pi d}, \tag{3.7}$$

where G is the shear modulus on the slip plane, b is the slip distance and d is the spacing distance between the slip planes. In the case of the $\{111\}/\frac{1}{6}<112>$ twinning system, b and d

are $a/\sqrt{6}$ and $a/\sqrt{3}$, respectively, where a is the lattice parameter of the FCC structure. The shear modulus G on the $\{111\}$ plane is expressed as $(2C'+C_{44})/3$ regardless of the shear direction [18], where C' is the shear modulus in the $<1\bar{1}0>$ direction on the $\{110\}$ planes and C_{44} is the shear modulus in the $<010>$ direction on the $\{001\}$ plane. In a cubic system, the relationship between the elastic constant C' and Young's modulus in certain direction E is [18]:

$$\frac{1}{E}=\frac{1}{9K}+\frac{1}{3C'}+(\frac{1}{C_{44}}-\frac{1}{C'})(l^2m^2+m^2n^2+n^2l^2), \tag{3.8}$$

where $K=(C_{11}+2C_{12})/3$ is the bulk modulus and l, m, n are the direction cosines of the uniaxial stress. In the case of compression in the $[001]_P$ direction, the elastic constant C' can be further expressed as:

$$C'=\frac{3E_{[001]_P}K}{9K-E_{[001]_P}}, \tag{3.9}$$

where the bulk modulus K of the Fe-30.0Pd (at.%) alloy is reported to be approximately 120 GPa [1]. We regard this value is the same with that of the Fe-31.2Pd (at.%) alloy. Using the average value of Young's modulus $E_{[001]_P}\approx 6$ GPa in the stress region above 100 MPa at 240 K as shown in Fig. 3.11, the elastic constant C' at 240 K is calculated to be approximately 2 GPa. The elastic constant C' at 300 K is calculated to be approximately 3.4 GPa, with the Young's modulus $E_{[001]_P}\approx 10$ GPa in the beginning region.

Using the Voigt approximation, the elastic constant C_{44} can be expressed by in terms of the Young's modulus of polycrystal E_{POLY} and the elastic constant C' [19,20]:

$$C_{44}=\frac{5E_{Poly}K+E_{Poly}C'/3-3KC'}{9K-E_{Poly}}. \tag{3.10}$$

We measured Young's modulus of an Fe-31.2Pd (at.%) polycrystal at 240 K and 300 K, and the

value is approximately 25.1 GPa and 40 GPa (see chapter 4), respectively. From the obtained elastic constant C' mentioned above and the bulk modulus K ($\approx$120 GPa [1]), the elastic constant C_{44} at 240 K and 300 K is calculated to be 14.1 GPa and 21.9 GPa, respectively. So, the shear modulus $(2C'+C_{44})/3$ in the $\{111\}/\frac{1}{6}<112>$ shear system at 240 K and 300 K is approximately 6 GPa and 9.6 GPa, respectively. Then the ideal shear strength τ_{IDEAL} of a perfect Fe-31.2Pd (at.%) single crystal at 240 K and 300 K is evaluated to be approximately 660 MPa and 1 GPa. From above calculations for the Fe-31.2Pd (at.%) single crystal, we find that the ideal shear stress τ_{IDEAL} (660 MPa) is nearly five times as large as the critical resolved shear stress (139 MPa) at 240 K; the ideal shear stress τ_{IDEAL} (1 GPa) is nearly seven times as large as the critical resolved shear stress (149 MPa) at 300 K.

In most bulk metals, the experimentally measured critical resolved shear stress (τ_{CRSS}) is far below the ideal shear stress (τ_{IDEAL}) with the ratio τ_{IDEAL}/τ_{CRSS} ranging from 10^2 to 10^3 [21]. Low τ_{CRSS} in bulk materials mainly arises from the movement of dislocations in the specimen. Near-ideal strength could be obtained when there are no initial dislocations in a specimen, such as whiskers and nanoscale materials. However, bulk materials without dislocations are extremely hard to manufacture. To the best of our knowledge, the only reported bulk material with near-ideal strength is Gum Metals which has a BCC structure [20,22]. The Fe-31.2Pd (at.%) single crystals in this work is the first reported bulk metal with FCC structure exhibiting a near-ideal shear strength.

3.5. Conclusions

The deformation behavior in the Fe-31.2Pd (at.%) single crystals exhibiting a second-order-like FCC-FCT MT is investigated by compressive tests in the $[001]_P$ direction.

From the results, the following conclusions have been reached:

(1) A large elastic-like strain of more than 6.5% with quite small stress hysteresis appears slightly above the transformation temperature (240 K) under stress of 250 MPa. Most of the large elastic-like strain is caused by the continuous change of structure in a single variant martensite variant.

(2) A yield point appears when the strain exceeds 7.3% compressed at 240 K under stress of 285MPa, and the residual strain did not recover by heating to 300 K. A similar yield point appear under 310 MPa at a strain approximately 4.6% compressed at 300 K. Introduction of mechanical twinning with twin boundary {111} is the main reason of the residual strain for both the plastically deformed specimens at 240 K and 300 K. Stress-induced BCC structure also appears in heavily deformed area. The shear strength of the Fe-31.2Pd (at.%) single crystal is close to the ideal value, which is first reported in bulk materials with FCC structure.

Reference

[1] S. Muto, R. Oshima and F. E. Fujita, *Acta. Metall.*, **38** (1990) 685.

[2] C. R. Cupp and B. Chalmers, *Acta. Metall.*, **2** (1954) 803.

[3] T. D. Fornesa and D. R. Paul, *Polymer*, **44** (2003) 4993.

[4] H. J. Kestenbach, *Metallography*, **10** (1977) 189.

[5] William D. Calliter, Jr, *Materials science and engineering: an introduction*-3rd ed, (John Wiley & Sons, Inc, 1994) 117.

[6] X. Ding, J. Zhang, Y. Wang, Y. Zhou, T. Suzuki, J. Sun, K. Otuska and X. Ren, *Phys. Rev. B*, **77** (2008) 174103-1.

[7] S. Miyazaki, Y. Ohmi, K. Otsuka and Y. Suzuki, *J. Phys.*, **43** (1982) C4-255.

[8] T. Saburi, S. Nenno, Y. Nishimoto and M. Zeniya, *J. Iron and Steel Inst. Japan*, **72** (1986) 571.

[9] T. Kakeshita, T. Fukuda and T. Takeuchi, *Mater. Sci. Eng. A*, **12** (2006) 438.

[10] S. Miyazaki, K. Otsuka and Y. Suzuki, *Scr. Metall.*, **15** (1981) 287.

[11] Y. Tanaka, Y. Himuro, R. Kainuma, Y. Sutou, T. Omori and K. Ishida, *Science*, **327** (2010) 488.

[12] J. W. Christian and S. Mahajan, *Prog. Mater. Sci.*, **39** (1995) 1.

[13] X. L. Wu, X. Z. Liao, S. G.. Srinivasan, F. Zhou, E. J. Lavernia and R. Z. Valiev, *Phys. Rev. Lett.*, **100** (2008) 095701

[14] S. S. Brenner, *J. Appl. Phys.*, **27** (1956) 1484.

[15] S. S. Brenner, *Science*, **128** (1958) 569.

[16] G. Richter, K. Hillerich, D. S. Gianola, R. Monig, O. Kraft and C. A. Volkert, *Nano Lett.*, **9** (2009) 3048.

[17] J. Frenkel, *Zeit. Phys.*, **37** (1926) 572.

[18] N. Nakanishi, *Prog. Mater. Sci.*, **24** (1980) 143.

[19] R. Hill, *Proc. Phys. Soc (London)*, **65** (1952) 349.

[20] T. Saito *et al. Science*, **300** (2003) 464 (see supplemental material).

[21] T. Zhu and J. Li, *Prog. Mater. Sci.*, **50** (2010) 710.

[22] T. S. Li, J. W. Morris, Jr., N. Nagasako, S. Kuramoto and D. C. Chrzan, *Phy. Rev. Lett.*, **98** (2007) 105503.

Chapter 4

Influence of various conditions on the limit of elastic strain in Fe-Pd alloys

4.1. Introduction

As described in chapter 3, more than 6.5% elastic-like strain is obtained in the Fe-31.2Pd (at.%) single crystals in the $[001]_P$ direction at 240 K. Considering that Young's modulus strongly depends on temperature and compressive direction, we can expect that the limit of the elastic strain in Fe-Pd alloys also significantly depends on these factors. Therefore, in this chapter, we examine the influence of temperature, compressive direction and grain boundary on the limit of the elastic strain in the Fe-Pd alloys.

4.2. Experiments

In this chapter, we use two alloys, Fe-31.2Pd (at.%) and 30.8Pd (at.%). The polycrystalline and single crystal specimens were prepared as described in chapter 2. The details of the specimens and compressive direction are listed in Table 4.1. The FCC-FCT MT temperature of the present Fe-31.2 (at.%) and 30.8Pd (at.%) alloys are approximately 230 K and 250 K, being the same temperature as mentioned in chapter 2. The grain size of the polycrystalline specimens

is approximately 150 to 350 μm. The compressive tests were conducted under the same condition mentioned in chapter 3.

Table 4.1. Details of the specimens for the compressive tests.

Composition (at.%)	Size of the specimen	Compressive direction
Fe-31.2Pd	3.4 $[100]_p$ mm × 3.4 $[010]_p$ mm × 11.4 $[001]_p$ mm	$[001]_P$
Fe-31.2Pd	2.4$[100]_p$ mm × 2.3$[010]_p$ mm × 6.6$[001]_p$ mm	$[001]_P$
Fe-31.2Pd	2.7 mm × 2.7 mm × 13.9 mm (polycrystal)	—
Fe-30.8Pd	3.3 $[100]_p$ mm × 3.4 $[010]_p$ mm × 11.0 $[001]_p$ mm	$[001]_P$
Fe-30.8Pd	2.7 $[100]_p$ mm × 2.7 $[010]_p$ mm × 7.0 $[001]_p$ mm	$[011]_P$

4.3. Results and discussion

4.3.1 The influence of temperature on the limit of the elastic strain

Figure 4.1 shows the stress-strain curves of the Fe-31.2Pd (at.%) single crystals compressed in the $[001]_P$ direction at 240 K (a) and 300 K (b), respectively. The dashed lines indicate the elastic deformation, and solid lines are the plastic deformation. A clear yield point appears in the stress-strain curve of single crystal. The yield stress in the $[001]_P$ direction is 285 MPa at 240 K and that is 310 MPa at 300 K; the corresponding elastic strains are 7.3% and 4.6%, respectively. As mentioned in chapter 3, the plastic deformation of the Fe-31.2Pd (at.%) single crystals compressed in the $[001]_P$ direction at 240 K and 300 K is mainly caused by the

mechanical twinning system $\{111\}/\frac{1}{6}<112>$.

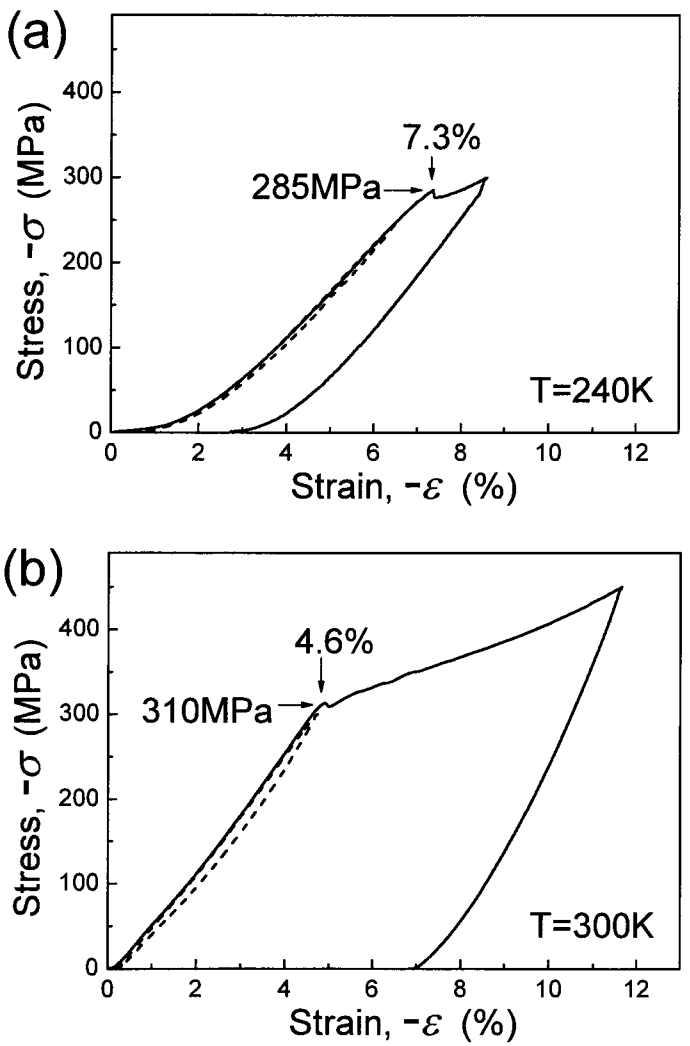

Fig. 4.1. The stress-strain curves of the Fe-31.2Pd (at.%) single crystals compressed in the $[001]_P$ direction at 240 K (a) and 300 K (b). The dashed lines indicate the elastic deformation.

4.3.2 Influence of orientation on the limit of the elastic strain

Figures 4.2(a) and (b) present the stress-strain curves of the Fe-30.8Pd (at.%) single crystals compressed in the (a) $[001]_P$ and (b) $[011]_P$ directions at different fixed temperatures (above the transformation temperature) indicated in the figures. The elastic-like strain in the $[001]_P$

direction also reaches approximately 3.7% under 100 MPa at 255 K. Owing to the similar Pd concentration, the elastic-like strain of the Fe-30.8Pd (at.%) single crystal in the $[001]_P$ direction is almost same as that of the Fe-31.2Pd (at.%) single crystal shown in chapter 3. However, the elastic strain in the $[011]_P$ direction is much smaller than the value in the $[001]_P$ direction at the same temperature and stress. The corresponding Young's modulus of the Fe-30.8Pd (at.%) single crystals in the $[001]_P$ and $[011]_P$ directions are evaluated in Fig. 4.2(c). Comparing with these two Young's modulus, we found that the Young's modulus in the $[001]_P$ direction is approximately eight times as large as that in the $[011]_P$ direction.

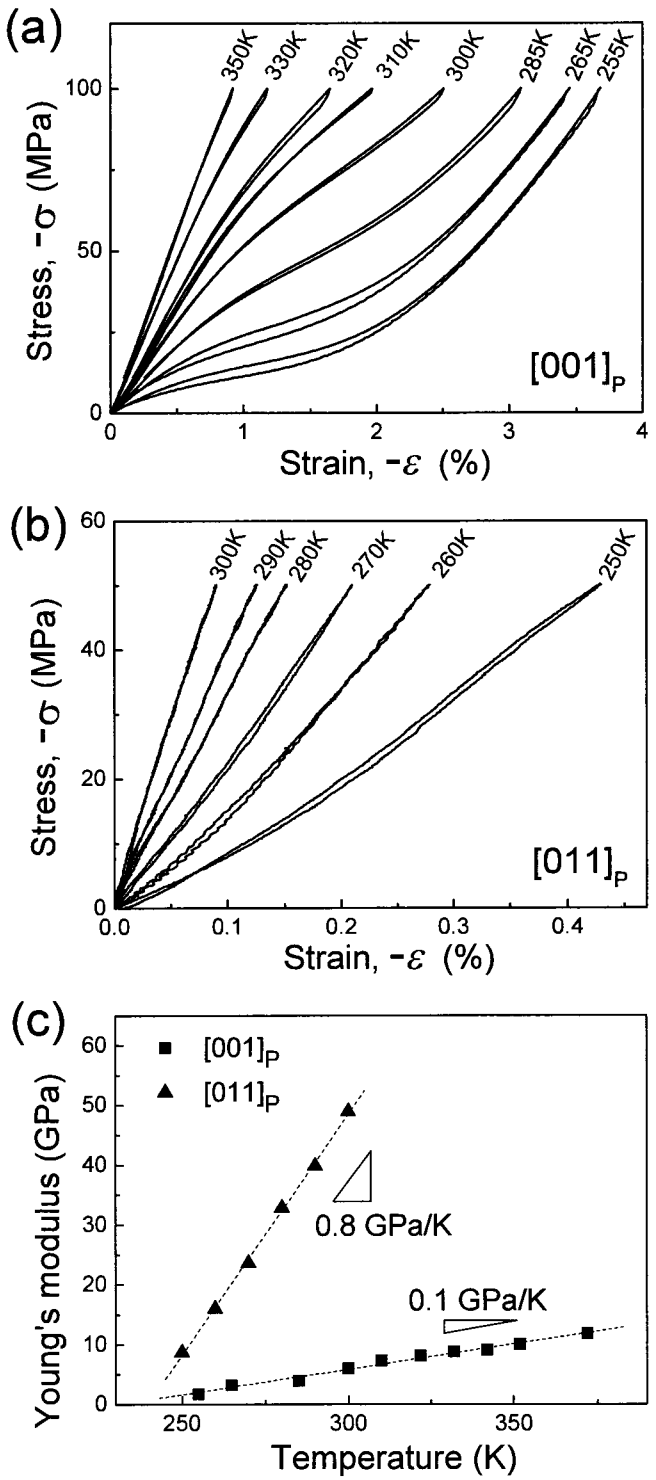

Fig. 4.2. The stress-strain curves of the Fe-30.8Pd (at.%) single crystals compressed in the (a) $[001]_P$ and (b) $[011]_P$ directions at different fixed temperatures indicated in the figures. (c) The temperature dependence of Young's modulus in the $[001]_P$ and $[011]_P$ directions.

Figure 4.3 shows the limit of the elastic strains of the Fe-30.8Pd (at.%) single crystals in the (a) $[001]_P$ and (b) $[011]_P$ directions at 255 K obtained by applying a larger stress. The dashed lines indicate the elastic deformation, and the solid lines are the plastic deformation. A clear yield point also appears in the stress-strain curve of single crystal. The yield stress in the $[001]_P$ direction is 270 MPa and that in the $[011]_P$ direction is 295 MPa; the corresponding elastic strains are 7.5% and 1.6%, respectively. The limit of the elastic strain in the $[001]_P$ direction of the Fe-30.8Pd (at.%) single crystal reaches approximately 7.5%, which is almost the same as that of the Fe-31.2Pd (at.%) single crystal. However, the limit of the elastic deformation in the $[011]_P$ direction is much shorter than that in the $[001]_P$ direction. This means that the limit of the elastic strain of the Fe-Pd single crystal significantly depends on the compressive direction. This behavior should be attributed to the large elastic anisotropy in Fe-Pd alloy, which will be further described in section 4.3.3.

The deformation system of the Fe-30.8Pd (at.%) single crystal compressed in the $[001]_P$ direction at 255 K should be the mechanical twinning $\{111\}/\frac{1}{6}<112>$, being the same as that of the plastically deformed Fe-31.2Pd (at.%) single crystal at 240 K. The critical resolved shear stress τ_{CRSS} is calculated to be 131 MPa. In the case of the Fe-30.8Pd (at.%) single crystal compressed in the $[011]_P$ direction at 255 K, the τ_{CRSS} in the mechanical twinning system $\{111\}/\frac{1}{6}<112>$ is calculated by a modified Schmid factor:

$$\cos\phi\cos\lambda = \sqrt{2}(c/a)/(2(c/a)^2+1), \tag{4.2}$$

where the tetragonality c/a in this case is approximately 0.98. The corresponding τ_{CRSS} is evaluated to be 140 MPa. It is also found that the τ_{CRSS} under compressive stress in the $[011]_P$ direction is close to that in the $[001]_P$ direction. This means plastic deformation may occurs in the mechanical twinning system $\{111\}/\frac{1}{6}<112>$ when compressed in the $[011]_P$ direction.

Further TEM experiments are needed to confirm the plastic deformation system in the $[011]_P$ direction.

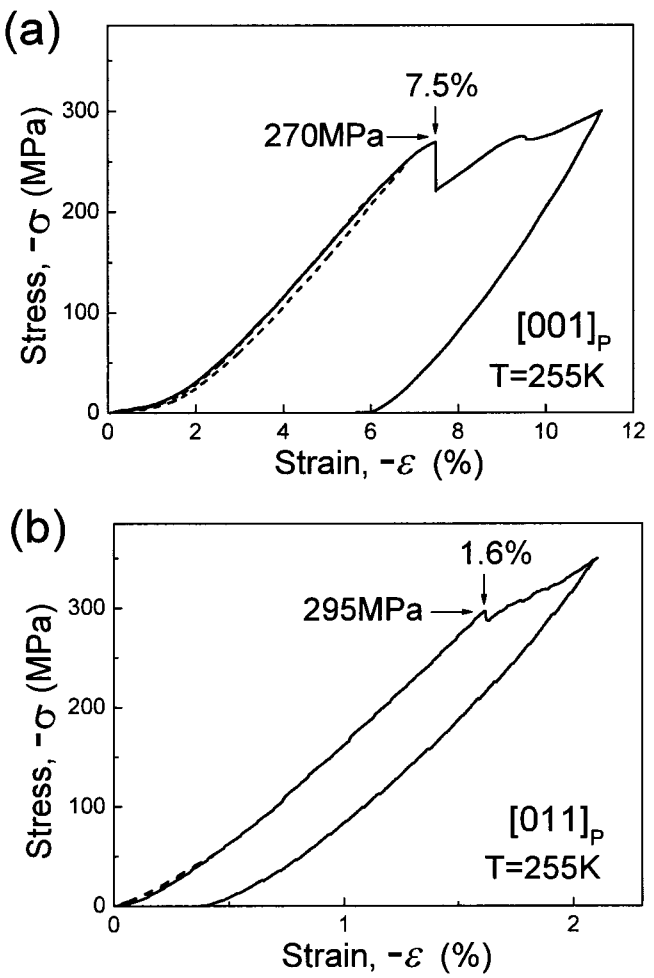

Fig. 4.3. The stress-strain curves of the Fe-30.8Pd (at.%) single crystals compressed in the (a) $[001]_P$ and (b) $[011]_P$ directions at 255 K. The dash lines indicate elastic deformation.

4.3.3 Influence of grain boundary on the limit of the elastic strain

Figure 4.4 shows the stress-strain curves of the Fe-31.2Pd (at.%) polycrystal compressed up to 50 MPa at different fixed temperatures as indicated in the figure.

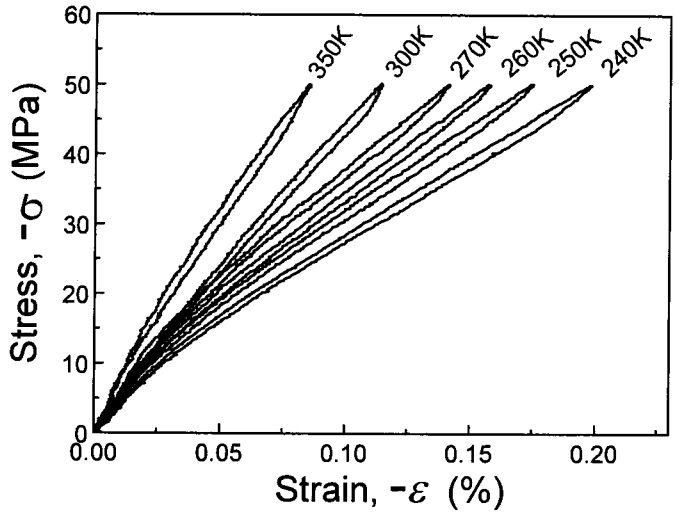

Fig. 4.4. The stress-strain curves of the Fe-31.2Pd (at.%) polycrystal compressed up to 50 MPa at different fixed temperatures indicated in the figure.

The corresponding Young's modulus is evaluated in Fig. 4.5(a). It is found that the Young's modulus of the polycrystal is much higher than that of the single crystal in the $[001]_P$ direction. Based on the Young's modulus in the $[001]_P$ direction and of polycrystal, the elastic constant C' and C_{44} of an Fe-31.2Pd (at.%) alloy can be evaluated. As mentioned in chapter 3, the elastic constant C' can be expressed as [1]:

$$C' = \frac{3E_{[001]_P}K}{9K - E_{[001]_P}}, \tag{4.3}$$

where the bulk modulus K is assumed to be approximately 120 GPa [2] in present study. Using the Young's modulus in the $[001]_P$ direction shown in Fig. 4.5(a), the elastic constant C' is evaluated in Fig. 4.5(b). The elastic constant C_{44} can also be expressed by the Young's modulus of polycrystal E_{POLY} and the elastic constant C' [3,4]:

$$C_{44} = \frac{5E_{Poly}K + E_{Poly}C'/3 - 3KC'}{9K - E_{Poly}}. \tag{4.4}$$

Using this formula, the elastic constant C_{44} is also evaluated in Fig. 4.5(b), which is much

higher than the elastic constant C'.

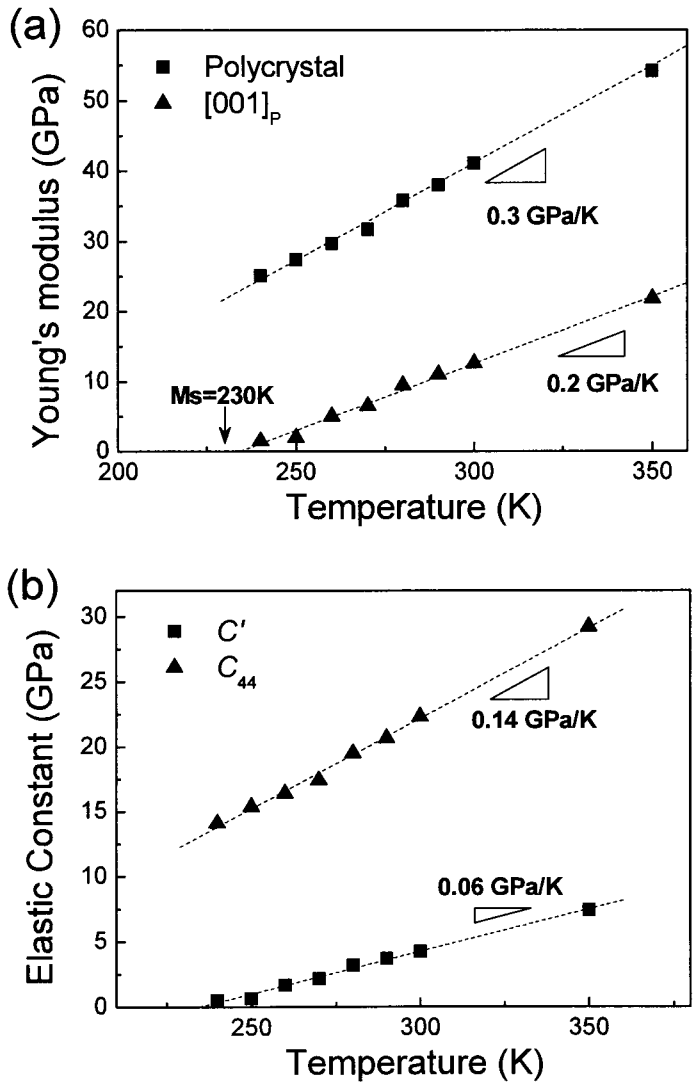

Fig. 4.5. (a) The Young's modulus of the Fe-31.2Pd (at.%) polycrystal compared with the values in the $[001]_P$ direction. (b) Temperature dependence of the calculated elastic constants C' and C_{44}.

The limit of the elastic strain of poly crystal at 240 K is also examined, and the result is presented in Fig. 4.6. The yield stress is approximately 150 MPa, and corresponding elastic strain is approximately 0.75%. These values are consistent with those reported in an Fe-30.5Pd (at.%) polycrystal [5]. If we assume the largest Schmid factor (0.5), the critical resolved shear

stress τ_{CRSS} turns out to be 75 MPa. It is found that the limit of elastic strain and the τ_{CRSS} are both much lower than that of the single crystals, especially the limit of elastic strain. This is mainly attributed to the large elastic anisotropy ($C_{44}/C' \approx 28$ for an Fe-31.2Pd (at.%) alloy at 240 K). Due to this large elastic anisotropy, the elastic strains generated in the grains with different orientations are quite different, and the imcompatibility of these elastic strains leads to high stress concentration at grain boundary. So, the plastic deformation occurs at relative low stress with small strain. This behavior is also reported in Cu-based SMAs with the large elastic anisotropy (e.g. $C_{44}/C' \approx 13$ [6] for Cu-Al-Ni alloy and $C_{44}/C' \approx 15$ [7] for Cu-Zn-Al alloy). However, the polycrystalline Ti-Ni SMAs exhibiting a low elastic anisotropy (approximately 2) show well superelastic behaviors [8,9].

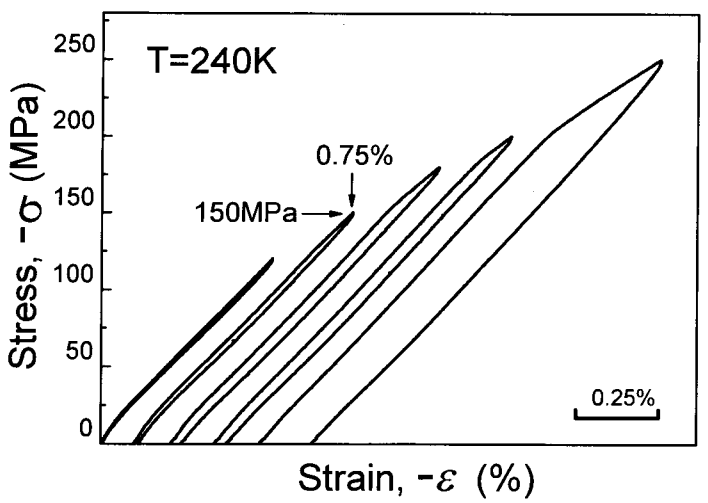

Fig. 4.6 The stress-strain curves of an Fe-31.2Pd (at.%) polycrystal at 240 K.

4.4. Conclusions

The influence of various conditions on the limit of the elastic strain in Fe-Pd alloys is investigated. The limit of the elastic strain of Fe-Pd alloys significantly depends on temperature,

which is probably attributed to the strong temperature dependence of elastic constant C'. The limit of the elastic strain is also significantly influenced by compressive direction and grain boundary because of the large elastic anisotropy in Fe-Pd alloy. On the other hand, the critical resolved shear stress is not significantly influenced by temperature and compressive direction; however, it is largely decreased by the existence of grain boundaries.

References

[1] S. S. Brenner, *J. Appl. Phys.*, **27** (1956) 1484.

[2] S. Muto, R. Oshima and F. E. Fujita, *Acta. Metall.*, **38** (1990) 685.

[3] S. S. Brenner, *Science*, **128** (1958) 569.

[4] G. Richter, K. Hillerich, D. S. Gianola, R. Monig, O. Kraft and C. A. Volkert, *Nano Lett.*, **9** (2009) 3048.

[5] H. Kato, Y. C. Liang and M. Taya, *Scr. Mater.*, **46** (2002) 471.

[6] M. Suezawa and K. Sumino, *Scr. Metall.* **10** (1976) 789.

[7] G. Guénin, M. Morin. P. F. Gobin, W. Dejonghe and L. Delaey, *Scr. Metall.*, **11** (1977) 1071.

[8] S. Miyazaki, Y. Ohmi, K. Otsuka and Y. Suzuki, *J. Phys.*, **43** (1982) C4-255.

[9] T. Saburi, S. Nenno, Y. Nishimoto and M. Zeniya, *J. Iron and Steel Inst. Japan*, **72** (1986) 571.

Chapter 5

Stress-temperature phase diagram of Fe-Pd single crystals with a critical point

5.1 Introduction

As introduced in chapter 1, a critical point is expected to be obtained in an Fe-Pd single crystal by compressing in the $[001]_P$ direction. We can expect the critical point because the symmetry of the elastically deformed parent phase is the same as that of the martensite phase. In addition, the tetragonality of an elastically deformed Fe-31.2Pd (at.%) single crystal reaches approximately 0.98~0.93 under compressive stress of 100 to 300 MPa in the $[001]_P$ direction, which reaches the tetragonality of the martensite phase with 0.98 to 0.94 at 220 to 77 K, as described in chapter 3 and 4. Such critical point has been reported in the liquid-gas phase diagram of water due to the same symmetry of these phases [1,2]. So, in this chapter, the stress-temperature phase diagrams of Fe-30.8 and 31.2Pd (at.%) single crystals are constructed by compressive tests in the $[001]_P$ direction, and the corresponding critical points are checked. The related behaviors are analyzed in the frame work of the Landau theory.

5.2 Experiments

The single crystals of Fe-30.8 and 31.2Pd (at.%) were prepared as described in chapter 2.

Parallelepiped specimens composed of $(100)_P$, $(010)_P$ and $(001)_P$ planes with size of 3.3 mm×3.3 mm×11.0 mm (30.8 at.%Pd) and 3.4 mm×3.4 mm×11.4 mm (31.2 at.%Pd) were cut from the single crystals. The FCC-FCT MT temperatures of the present single crystals are the same as the temperature mentioned in chapter 2. The compressive tests were conducted under the same condition mentioned in chapter 3. The strain-temperature curves were obtained by thermal cycle tests in the temperature range between 150 K and 360 K with the cooling and heating rate of 1 K/min under constant compressive stresses 0 to 80 MPa in the $[001]_P$ direction.

5.3 Results

5.3.1 Stress-strain curves

Figure 5.1(a) shows stress-strain curves of an Fe-31.2Pd (at.%) single crystal compressed up to 100 MPa in the $[001]_P$ direction at fixed temperatures indicated in the figure. As confirmed in chapter 3, the stress-induced MT occurs at 240 K, and the stress for inducing MT can be determined by the minimum in the curve of $d\sigma_{33}/d\varepsilon_{33}$ as a function of the applied stress. In order to investigate the stress for inducing MT at different temperatures, the stress-strain curves in the loading process are further analyzed by the curve of $d\sigma_{33}/d\varepsilon_{33}$ as a function of the applied stress $-\sigma_{33}$ shown in Fig. 5.1(b). It is found that a minimum appears in the temperature range between 240 K and 290 K. This minimum corresponds to the stress for inducing the MT which is between the start and finish stresses for inducing MT. However, the stress-induced MT does not occur when the temperature above 280K, which will be further described in section 5.4. From the minimums in Fig. 5.1(b), the stress for inducing MT as a function of temperature is drawn in Fig. 5.1(c)

According to the Clausius-Clapeyron relationship, the equilibrium stress at temperature T

between the parent and martensite phases is given as:

$$\frac{d\sigma}{dT} = -\frac{\Delta S}{\Delta \varepsilon} = -\frac{\Delta H}{T\Delta \varepsilon}, \tag{5.1}$$

where σ is the stress for inducing MT, ΔS is the change of the entropy, ΔH is the latent heat from MT, T is the transformation temperature, $\Delta \varepsilon$ is the transformation strain in the $[001]_P$ direction at the MT temperature. For the Fe-31.2Pd (at.%) single crystal, ΔH at 230 K is approximately 25 J/mol, which is obtained from DSC measurement in chapter 2. The transformation strain $\Delta \varepsilon$ at 230 K is approximately 1.3% as calculated in chapter 3. By substituting the above values into eq. (5.1), the $d\sigma/dT$ is calculated to be approximately 1.1 MPa/K. This result is consistent with the slope 1.2 MPa/K in Fig. 5.1(c). Therefore, we may regard the minimum in Fig. 5.1(b) as the stress for inducing MT.

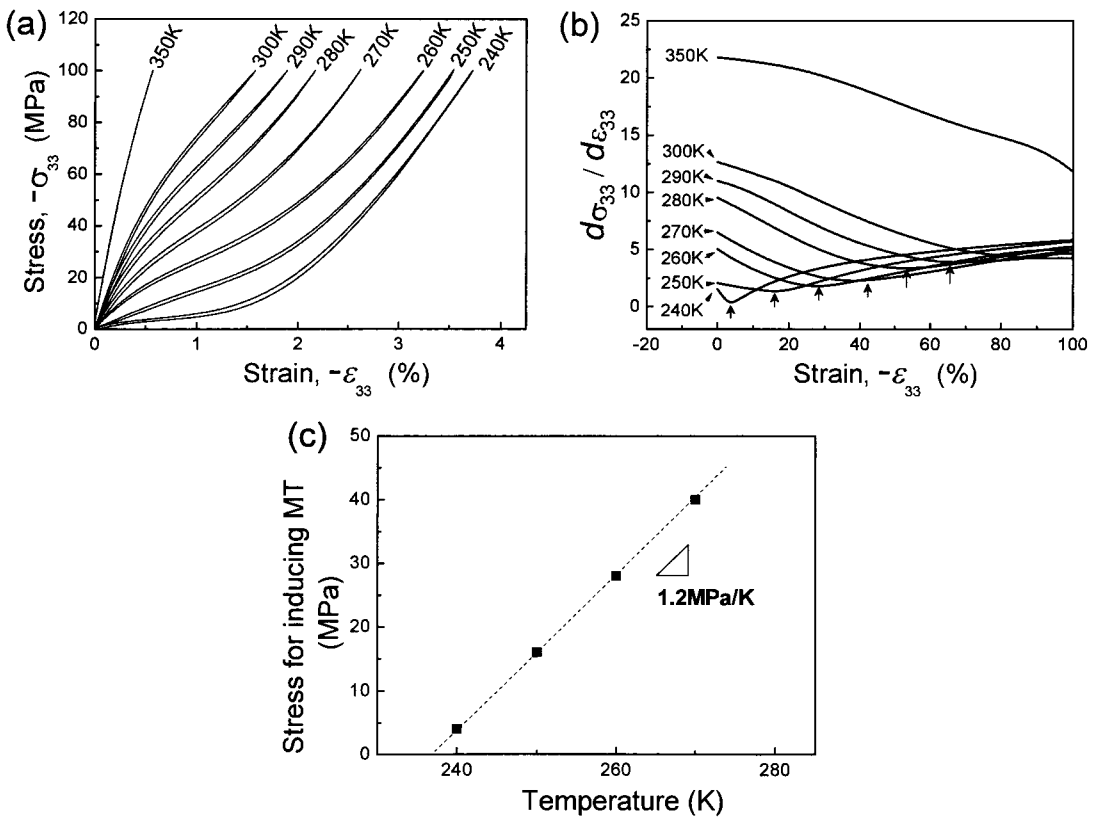

Fig. 5.1. (a) The stress-strain curves of Fe-31.2Pd (at.%) single crystal compressed in the $[001]_P$ direction at different fixed temperatures indicated in the figure. (b) The $d\sigma_{33} / d\varepsilon_{33}$ calculated from (a) as a function of the applied stress $-\sigma_{33}$ at different temperatures. (c) Temperature dependence of the stress for inducing MT (between the start and finish stresses for inducing MT).

5.3.2 Strain-temperature curves

The strain-temperature curves of an Fe-31.2Pd (at.%) single crystal are obtained by thermal cycling tests under different constant stresses as shown in Fig. 5.2(a). The stress-induced MT temperature M_s^σ and A_f^σ are determined by a tangent method, and the transformation strain $\Delta\varepsilon$ is determined from the difference in strain between the cooling and heating processes at M_s^σ. These methods are illustrated in a magnified figure in Fig. 5.2(b). Dependence of the applied stress in the $[001]_P$ direction on the stress-induced transformation temperatures M_s^σ and A_f^σ is shown in Fig. 5.2 (c). M_s^σ and A_f^σ linearly increase with increasing the applied stress, and the points are fitted in lines with slopes of 1.2 and 1.0 K/MPa, respectively. The slope of M_s^σ curve is almost consistent with that obtained from stress-strain curves shown in Fig. 5.1(c). With increasing the applied stress, the temperature hysteresis between M_s^σ and A_f^σ decreases, and disappear under 36 MPa.

With extending these two lines, a crossing point appears at (36 MPa, 280 K). At this stress, M_s^σ is expected to coincide with A_f^σ. The agreement between M_s^σ and A_f^σ implies that the point (36 MPa, 280 K) could be a critical point. On the other hand, the transformation strain $\Delta\varepsilon$ dependence of the applied stress $-\sigma_{33}$ is shown in Fig. 5.2(d). It is found that $\Delta\varepsilon$ decreases with increasing the applied stress. The points in Fig. 5.2(d) are also fitted in a line with a slope of -0.04 %/MPa. With extending the line, the transformation strain becomes zero under 37 MPa, which is consistent with the critical stress in Fig. 5.2(c).

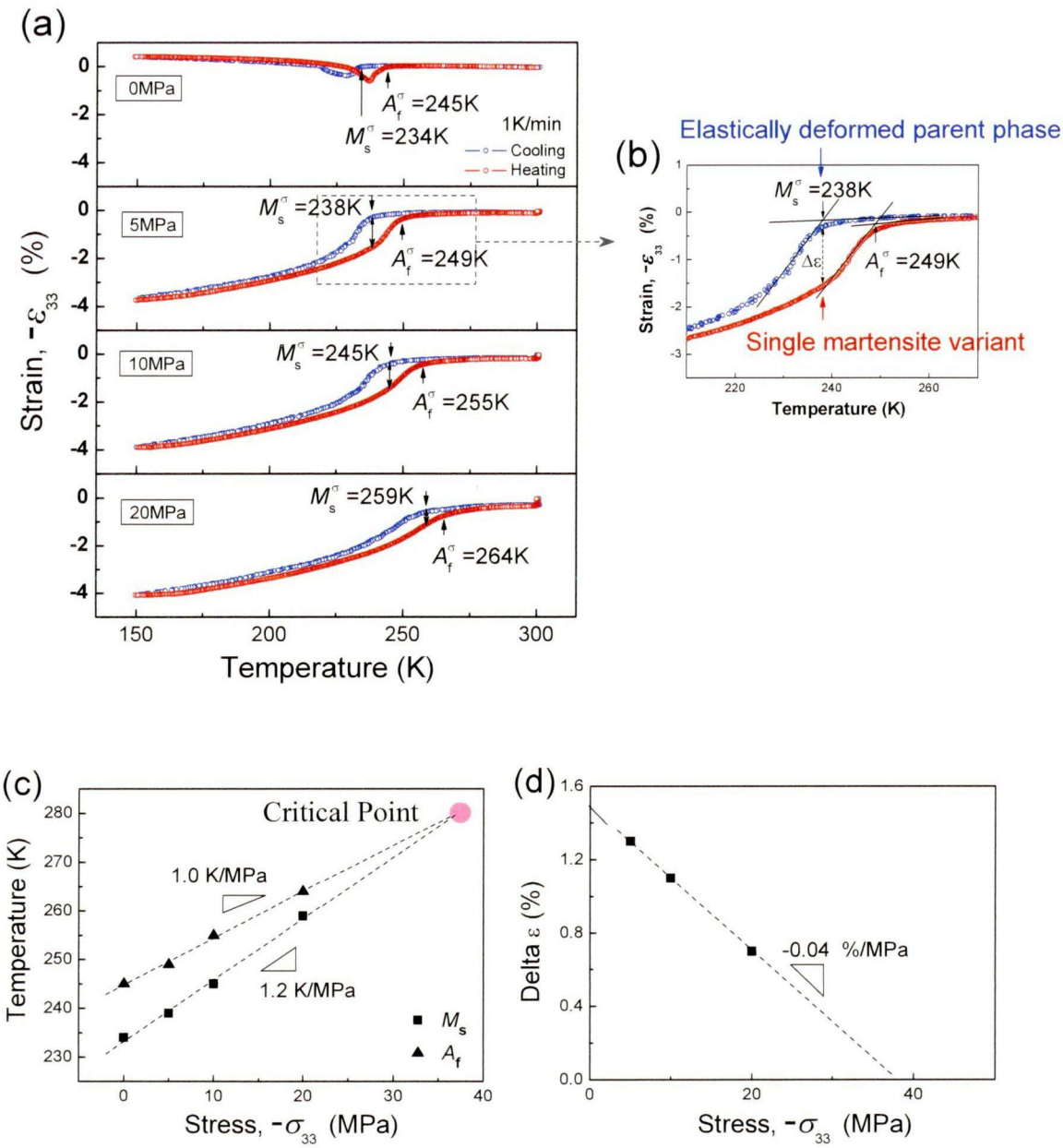

Fig. 5.2. (a) The strain-temperature curves of an Fe-31.2Pd (at.%) single crystal under different constant stresses in the temperature range between 150 K and 320 K, (b) the methods of determining stress-induced MT temperatures M_s^σ and A_f^σ and the transformation strain $\Delta\varepsilon$, (c) the stress-induced MT temperatures M_s^σ and A_f^σ as a function of the applied stress $-\sigma_{33}$, (d) the transformation strain $\Delta\varepsilon$ as a function of the applied stress $-\sigma_{33}$.

The similar strain-temperature curves are also measured in an Fe-30.8Pd (at.%) single crystal, and the results are presented in Fig. 5.3. With extending the transformation temperature M_s^σ and A_f^σ curves, a crossing point appears at (100 MPa, 330 K). The corresponding transformation strain $\Delta\varepsilon$ also decreases with increasing the applied stress with a slop of -0.02 %/MPa. With extending the line, $\Delta\varepsilon$ becomes zero under approximately 100 MPa, which is consistent with the critical stress in Fig. 5.3(b).

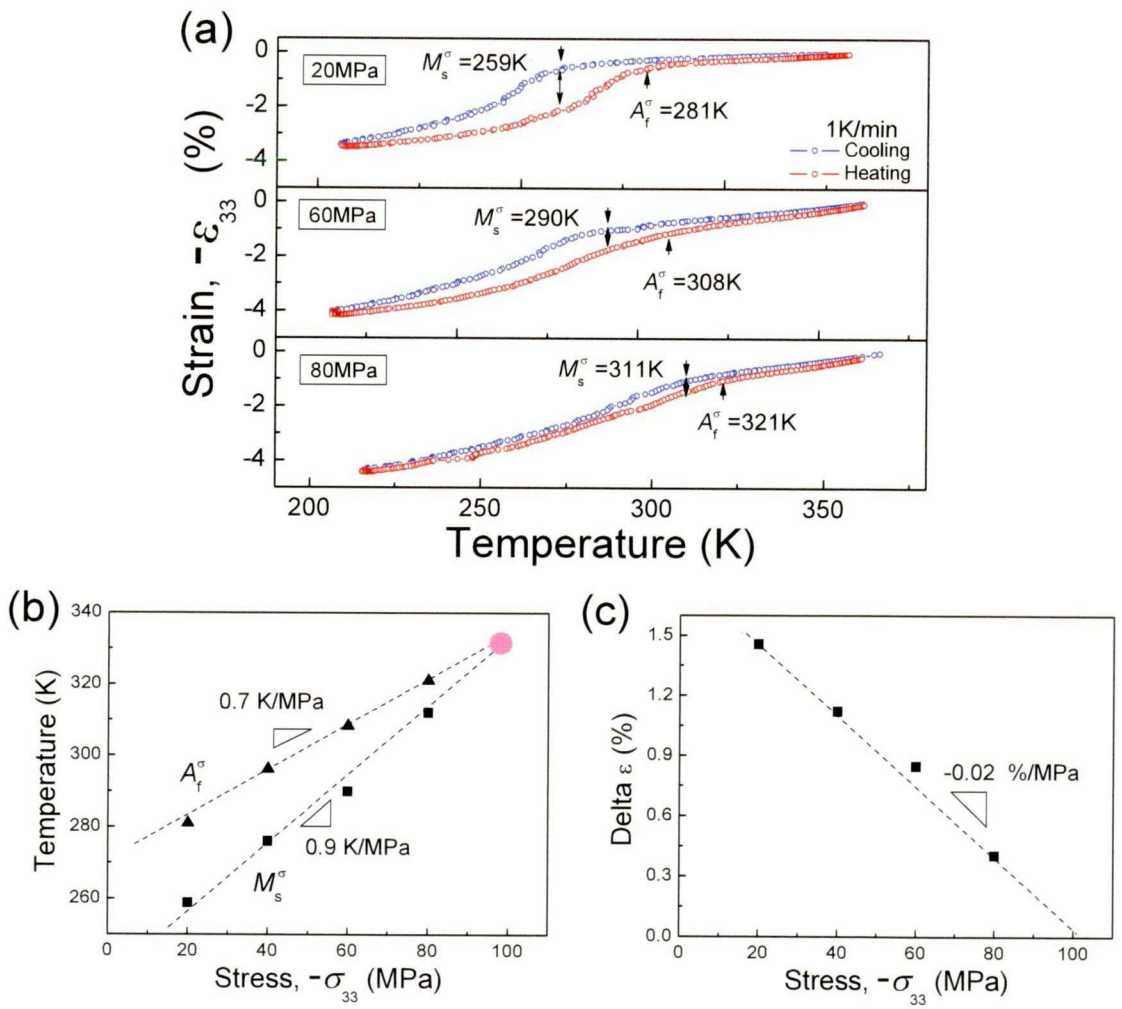

Fig. 5.3. (a) The strain-temperature curves of an Fe-30.8Pd (at.%) single crystal under different constant stresses in the temperature range between 200 K and 360 K, (b) the stress-induced MT temperatures M_s^σ and A_f^σ as a function of the applied stress $-\sigma_{33}$, (c) the transformation strain $\Delta\varepsilon$ as a function of the applied stress $-\sigma_{33}$.

5.4 Discussion

5.4.1 Landau theory for SMAs

The reversibility between the high symmetrical structure (the parent phase) and the low symmetrical structure (the martensite phase) indicates that this transformation could be analyzed in the framework of the Landau theory. In theory, the Gibbs free energy of SMAs could be expanded as a power series of spontaneous strain (order parameter). The difference in the Gibbs free energy between the phases can be given by [3-6]:

$$\Delta G = \frac{1}{2}\alpha(T - T_1)\varepsilon^2 + \frac{1}{3}B\varepsilon^3 + \frac{1}{4}C\varepsilon^4 - \sigma\varepsilon, \tag{5.2}$$

where $\alpha > 0$, $C > 0$ and $B < 0$, σ is the external uniaxial stress, ε is the corresponding spontaneous strain. The difference in Gibbs free energy ΔG as a function of the spontaneous strain ε is drawn in Fig. 5.4. The minimum of the Gibbs free energy at the original point represents the parent phase, and additional minimum of the Gibbs free energy corresponds to the martensite phase. The spontaneous strain ε of the stable or metastable phase is determined by the minimization of ΔG with respect to the strain:

$$\frac{\partial \Delta G}{\partial \varepsilon} = 0 \quad \text{and} \quad \frac{\partial^2 \Delta G}{\partial^2 \varepsilon} > 0. \tag{5.3}$$

When the external uniaxial stress is $\sigma = 0$, the ΔG as a function of the spontaneous strain ε at different temperature can be drawn as Fig. 5.4(a). In the high temperature range $T > T_2$ ($T_2 = T_1 + \frac{B^2}{4\alpha C}$), there only exists the parent phase with minimization of ΔG at the origin point. With decreasing temperature to the range of $T_2 > T > T_0$ ($T_0 = T_1 + \frac{2B^2}{9\alpha C}$), another minimization appears at $\varepsilon = -\frac{2B}{3C}$ which corresponds to the metastable martensite phase. When the temperature is above T_0, the parent phase is the stable phase with relative lower Gibbs free energy. With further decreasing the temperature to the range of $T_0 > T > T_1$, the parent phase becomes the metastable phase and the martensite phase becomes the stable phase. It is should noted that there is always energy barrier between the parent and the martensite phases in the temperature range between T_1 and T_2 as indicated in a magnified figure in

Fig. 5.4(a). When the temperature is below T_1, the parent phase becomes unstable and there only exists the martensite phase. Fig. 5.4(b) to (d) shows the ΔG as a function of the spontaneous strain ε under different external uniaxial stresses σ. It is found that the energy barrier between the parent phase and the martensite phase decreases with increasing the applied stress, and it disappears when the applied stress is above the critical stress σ_C $(=-\frac{B^3}{27C^2})$.

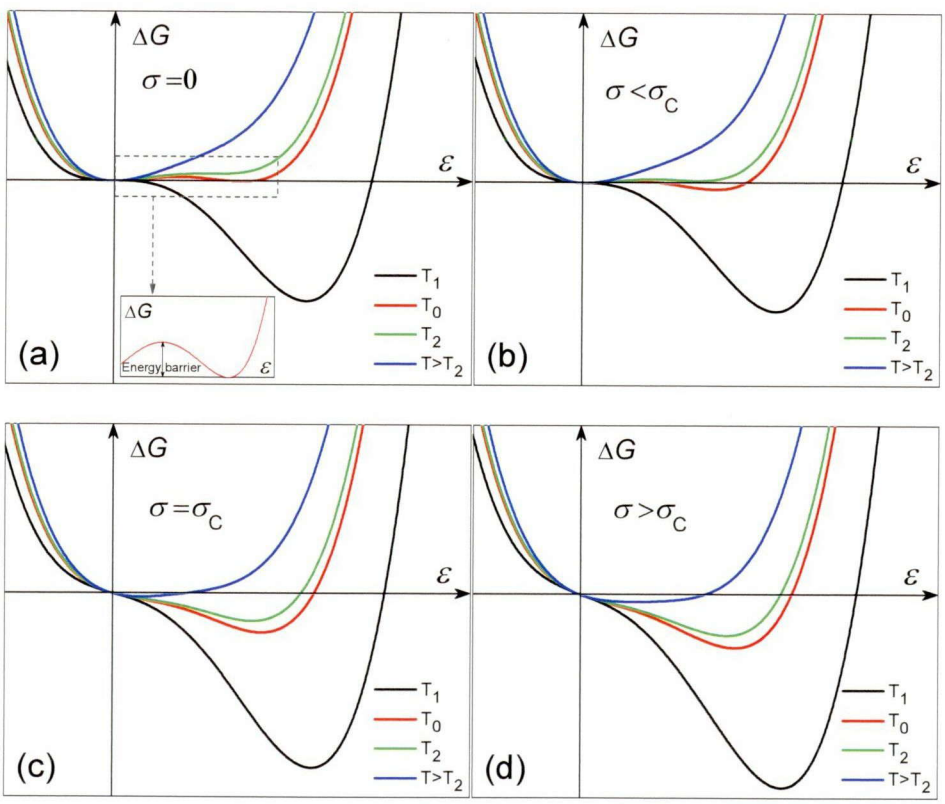

Fig. 5.4. The difference Gibbs free energy ΔG between the parent phase and the martensite phase as a function of spontaneous strain ε under different external uniaxial stress $\sigma = 0$ (a), $\sigma < \sigma_C$ (b), $\sigma = \sigma_C$ (c), $\sigma > \sigma_C$ (d).

The uniaxial stress σ is defined as derivative of the Gibbs free energy with respect to the spontaneous strain ε:

$$\sigma = \alpha(T - T_1)\varepsilon + B\varepsilon^2 + C\varepsilon^3 . \tag{5.4}$$

Figure 5.5(a) shows the calculated stress-strain curves under compressive stress at different

temperatures. The transformation strain $\Delta\varepsilon$ and stress hysteresis are the characteristics of a first-order MT. With increasing the temperature, these characteristics gradually decrease and disappear when the temperature reaches the critical temperature T_c ($=T_1+\frac{B^2}{3\alpha C}$). It should be noted that the inflexion point exists in the stress-strain curves even at temperatures above T_C. This can explain the appearance of minimum in the $d\sigma_{33}/d\varepsilon_{33}$ curve above the critical temperature (280 K) in Fig. 5.1(b).

From the stress-strain curves in Fig. 5.5(a), the strain-temperature curves under different constant stresses are also evaluated in Fig. 5.5(b). The discontinuous strain $\Delta\varepsilon$ (transformation strain) at M_s^σ and the corresponding hysteresis also gradually disappear when the external uniaxial stress reaches σ_c at T_c. At this critical point, the first-order MT changes into second-order MT. Above this critical point, there is no transformation and no difference between the parent and martensite phase.

The transformation strain $\Delta\varepsilon$ and corresponding stress-induced MT temperatures M_s^σ and A_f^σ as a function of the applied stress are shown in Fig. 5.5(c) and (d), respectively. The transformation strain decrease with increasing the applied stress, and a critical point (σ_c, T_c) appears at the crossed point of two transformation temperature curves. It is found that the experimental results of the Fe-30.8 and 31.2Pd (at.%) single crystals are consistent with the model simulated by the Landau theory.

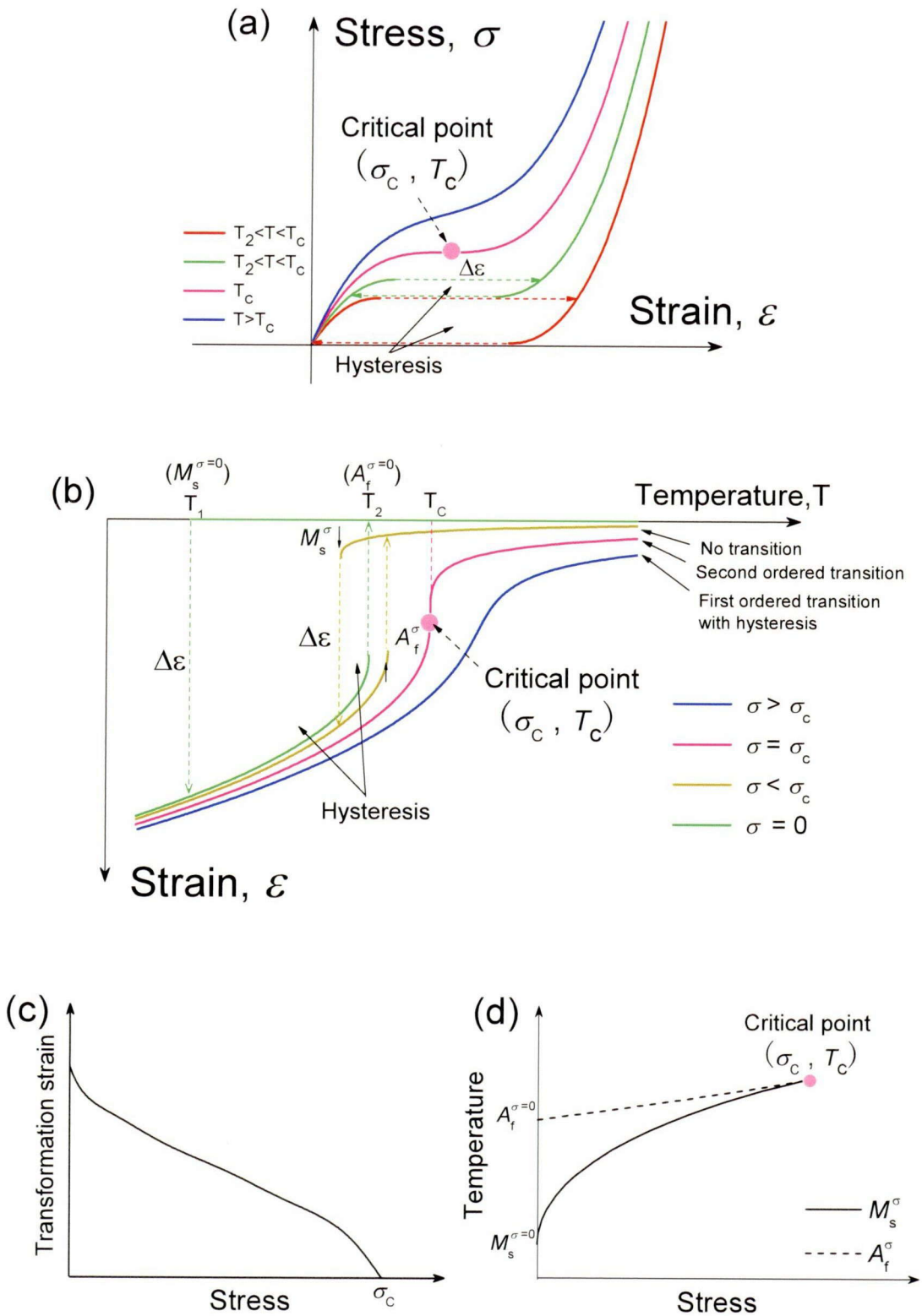

Fig. 5.5. (a) The simulated stress-strain curves at different fixed temperatures. (b) The simulated strain-temperature curves under different constant uniaxial stresses. The transformation strain (c) and transformation temperature M_s^σ and A_f^σ (d) dependence on the applied stress with a critical point (σ_c, T_c).

5.4.2 The stress-temperature phase diagram

From the experimental results, the stress-temperature phase diagram of Fe-30.8 and 31.2Pd (at.%) single crystals can be drawn as Fig. 5.6. The parent phase with FCC structure only appears when the temperature is above the transformation temperature T_M without external stress. Under external stress, the parent phase with FCC structure changes into the elastically deformed parent phase with a FCT structure. When the compressive temperature is between the transformation temperature T_M and the critical temperature T_C, the elastically deformed parent phase exhibits a stress-induced first-order MT. These behaviors were confirmed by *in-situ* X-ray experiments mentioned in chapter 3. But at the critical temperature, the parent phase continuously changes into the martensite phase, and the first-order transformation become second-order type. Above the critical point, there is no difference between the parent and martensite phase.

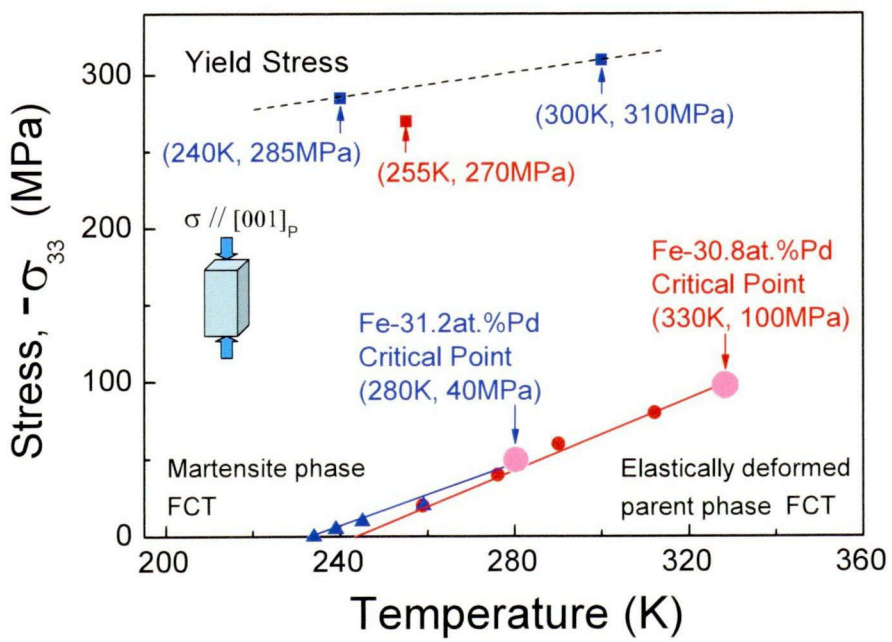

Fig. 5.6. The stress-temperature phase diagram of the Fe-30.8 and 31.2at.%Pd single crystal with the critical point at (330 K, 100 MPa) and (280 K, 40 MPa).

The essentially important condition for the appearance of the critical point in the Fe-Pd alloys is that the parent and the martensite phases have the same symmetry under a compressive stress in the $[001]_P$ direction. This situation is difficult to achieve in other tensile or compressive conditions. For example, in the case of tensile in the $[001]_P$ direction, the tetragonality of the elastically deformed parent phase is large than unity which is different from that of the martensite phase (less than unity). Also, when the Fe-Pd single crystal is compressed in the $[011]_P$ direction, the elastically deformed parent phase is orthorhombic and the elastically deformed martensite phase is monoclinic. The different symmetry between the elastically deformed parent phase and the martensite phase indicates that there is no critical point in these conditions.

On the other hand, it should be noted that the critical stresses of Fe-Pd single crystals are much lower than yield stress, which is mainly attributed to the large elastic anisotropy of Fe-Pd alloy mentioned in chapter 4. This is another reason that we can detect the critical point in the stress-temperature phase diagram of Fe-Pd alloys avoiding the plastic deformation.

5.5. Conclusions

The critical point in the stress-temperature phase diagram of SMAs is theoretically analyzed by the Landau theory and its existence has been confirmed in the Fe-30.8 and 31.2Pd (at.%) single crystals by compressed in the $[001]_P$ direction. The stress-temperature phase diagram of the Fe-Pd single crystals is constructed. The critical points appearing at (330 K, 100 MPa) for an Fe-30.8Pd (at.%) single crystal and at (280 K, 40 MPa) for an Fe-31.2Pd (at.%) single crystal are indicated in the stress-temperature phase diagram.

References

[1] L. Landau and E. Lifshitz, *Statistical Physics*, (Pergamon Press 1990) part 1, 3rd ed.

[2] H. B. Callen, *Thermodynamics and an Introduction to Thermostatistics*, (Jonn Wiley & Sons, 1985).

[3] F. Falk, *Acta Metallurgica*, **28** (1980) 1773.

[4] M. A. Fradkin, *Phy. Rev. B*, **50** (1994) 16326.

[5] F. Falk, *J. de Phys.*, **43** (1982) C4-3.

[6] V. A. L'vov, N. Matsishin, N. Glavatska, *Phase. Trans*, **83** (2010) 293.

Chapter 6

Large elastocaloric effect in an Fe-31.2Pd (at.%) single crystal

6.1 Introduction

As mentioned in chapter 1, a large elastocaloric effect in a wide temperature range is expected to be obtained in Fe-Pd alloys due to the significant temperature dependence of the elastic constant C'. Large elastic-like deformation and the significant temperature dependence of the Young's modulus in the $[001]_P$ direction are obtained in an Fe-31.2Pd (at.%) single crystal as mentioned in chapter 3. In this chapter, we check the elastocaloric effect in an Fe-31.2Pd (at.%) single crystal by compressive tests in the $[001]_P$ direction.

6.2 Experiments

Fe-31.2Pd (at.%) single crystal was prepared as mentioned in chapter 2. A parallelepiped specimen composed of $(100)_P$, $(010)_P$ and $(001)_P$ planes with a size of $3.3\ \text{mm} \times 3.3\ \text{mm} \times 6.9\ \text{mm}$ was cut from the single crystal. The compressive method is the same as the method introduced in chapter 3. The elastocaloric effect was examined by loading and unloading with a high strain rate of $0.13\ \text{s}^{-1}$ to realize an adiabatic condition. The temperature change of the specimen induced by the adiabatic stress change was monitored by a T-type thermocouple welded on the surface of the specimen.

6.3 Results and discussion

Figure 6.1(a) shows the stress-strain curves of the Fe-Pd single crystal compressed up to 100 MPa in the $[001]_P$ direction, which is also shown in chapter 3. Figure 6.1(b) presents the strain-temperature curves under some fixed stresses in the unloading process reproduced from Fig. 6.1(a). It is found that the strain under constant stress continuously increases with decreasing temperature in a wide temperature range. This behavior is also confirmed by the strain-temperature curves mentioned in chapter 5. So, we can calculate the isothermal entropy change and the adiabatic temperature change from the results of Fig. 6.1 as follows.

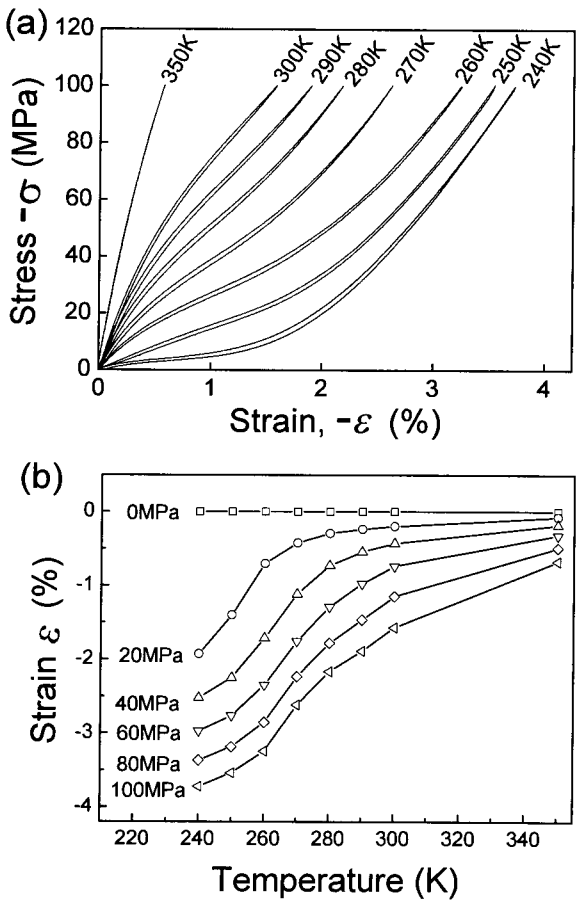

Fig. 6.1. (a) The stress-strain curves of the Fe-31.2Pd (at.%) single crystal compressed in the $[001]_P$ direction under 100 MPa at the fixed temperatures indicated in the figure, (b) the strain-temperature curves under different constant stresses during the unloading process reproduced from (a).

The isothermal entropy change ΔS_{iso} induced by an uniaxial stress σ is given by [1]

$$\Delta S_{iso}(0 \rightarrow \sigma) = \int_0^{\sigma} \left(\frac{\partial S}{\partial \sigma} \right)_T d\sigma . \tag{6.1}$$

Using the generalized Maxell's relationship $\left(\frac{\partial S}{\partial \sigma} \right)_T = \left(\frac{\partial \varepsilon}{\partial T} \right)_\sigma$, the isothermal entropy change is further given by

$$\Delta S_{iso}(0 \rightarrow \sigma) = \int_0^{\sigma} \left(\frac{\partial \varepsilon}{\partial T} \right)_\sigma d\sigma \ , \tag{6.2}$$

where ε is the strain induced by the applied stress σ. Meanwhile, the temperature change ΔT_{adi} caused by adiabatic stress application is given as

$$\Delta T_{adi} = -\int_0^{\sigma} \frac{T}{C_p} \left(\frac{\partial \varepsilon}{\partial T} \right)_\sigma d\sigma , \tag{6.3}$$

where C_p is heat capacity which is roughly approximately equal to $3R$ (R=8.314 J/(mol·K)) in the present study. The isothermal entropy change and adiabatic temperature change are simply illustrated in Fig. 6.2.

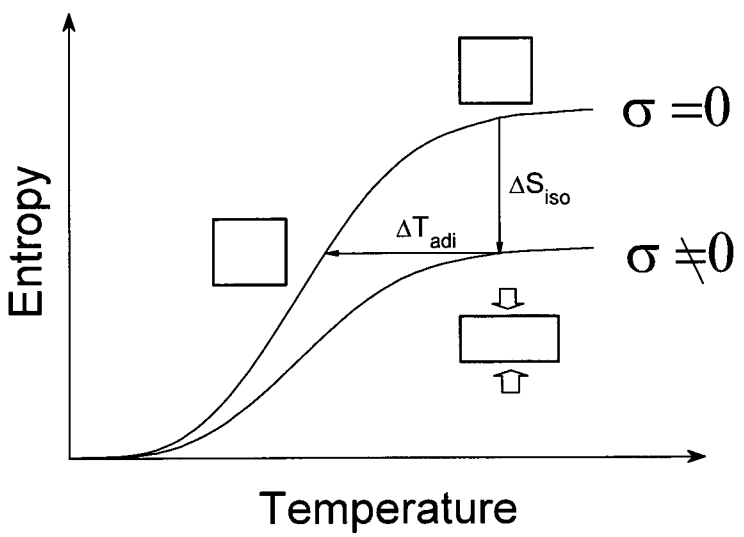

Fig. 6.2. An illustration showing the isothermal entropy change ΔS_{iso} and adiabatic temperature change ΔT_{adi} in an elastocaloric effect.

Using the value of $\left(\frac{\partial \varepsilon}{\partial T}\right)_{\sigma}$ in Fig. 6.1(b), the isothermal entropy change ΔS_{iso} and the adiabatic temperature change ΔT_{adi} of the Fe-Pd single crystal with the applied stress of 100 MPa are evaluated, and the results are presented in Fig. 6.3. We notice that ΔS_{iso} is larger than 0.1 J/(mol·K) and $|\Delta T_{adi}|$ is larger than 1 K in a wide temperature range (below 300 K). It should be noted that the temperature change $|\Delta T_{adi}|$ of 2 K is a thousand times larger than that in a pure Fe under the same condition [2].

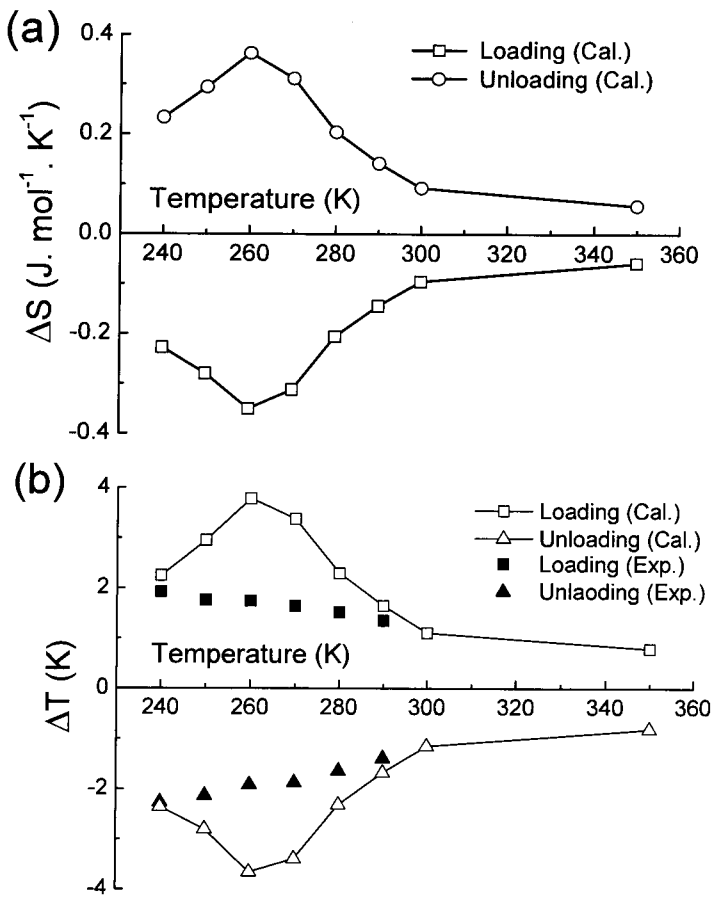

Fig. 6.3. The calculated isothermal entropy changes (a) and the calculated adiabatic temperature changes (b) of the Fe-31.2Pd (at.%) single crystal with the compressive stress of 100 MP in the $[010]_P$ direction based on the stress-strain curves in Fig. 6.1(a). The solid points in (b) represent the experimental temperature change induced by the adiabatic stress change up to 100 MP at different temperatures.

In order to certify the temperature change, we have made the compressive tests of the Fe-Pd single crystal with a high strain rate. Figure 6.4(a) shows the applied compressive stress as a function of time at 240 K (furnace temperature), and the corresponding temperature change of the specimen as a function of time is shown in Fig. 6.4(b). The temperature increases by 1.9 K in the loading process up to 100 MPa, and decreases by 2.3 K in the unloading process. The same experiments were made at other temperatures, and the results are drawn in Fig. 6.3(b). From 240 K to 290 K, the experimental temperature decrease induced by the adiabatic stress removal is approximately 2 K, which is the same order as the calculated values. The deviation between the experimental and the calculated values is possibly caused by the insufficient adiabatic condition. It should be noted that the temperature range of the large elastocaloric effect in the Fe-Pd single crystal (over 50 K) is much larger than that reported in Cu-based SMAs (approximately 15 K [1]) with a first-order MT and that of magnetocaloric effect in Gd-based or Mn-based compounds (approximately 20 to 30 K [3-5]) with a first-order magnetostructural transformation.

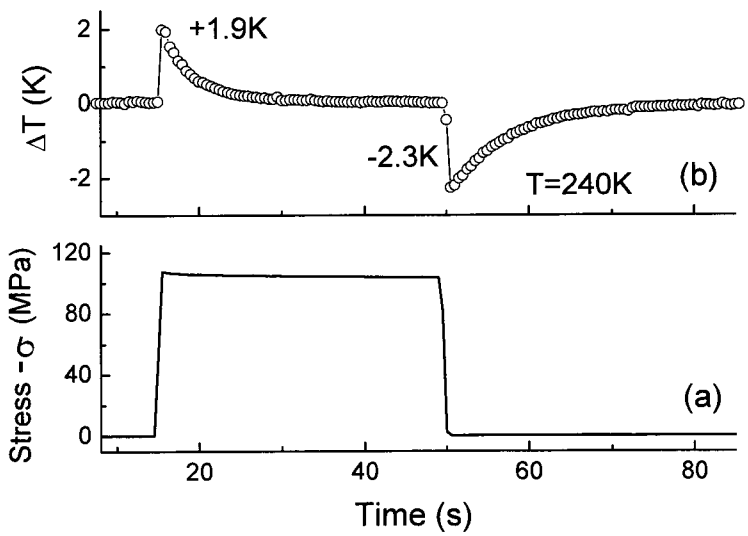

Fig. 6.4. The experimental temperature change in the Fe-31.2Pd (at.%) single crystal by the adiabatic compressive in the $[010]_P$ direction at 240 K: the applied stress (a) and the corresponding temperature change (b) as a function of time.

As mentioned in chapter 4, the yield stress of an Fe-31.2Pd (at.%) single crystal in the $[001]_P$ direction at 240 K is approximately 285 MPa, and that at 300 K is approximately

310 MPa. This means that we can apply the stress up to approximately 280 MPa, and higher temperature change can be obtained. So, the adiabatic temperature changes under different stresses at 240 K are examined, and the results are present in Fig. 6.5. With increasing the applied stress, the temperature change induced by adiabatic stress change increases almost linearly, and the temperature decrease under 200 MPa is over 3 K.

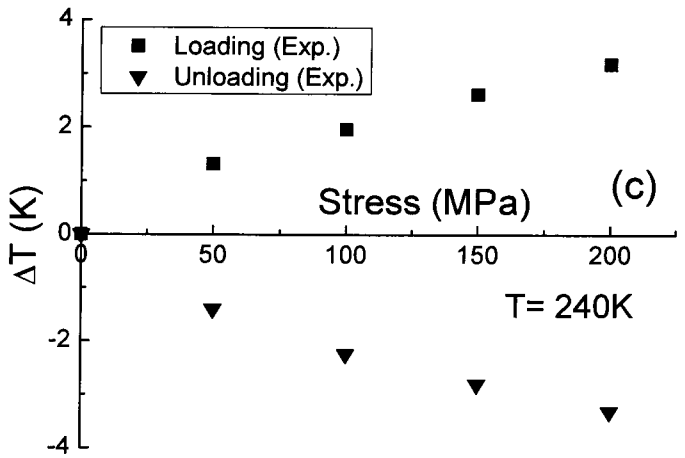

Fig. 6.5.The compressive stress in the $[010]_P$ direction dependence of the experimental temperature change.

Beside the maximum temperature decrease induced by adiabatic stress removal, the refrigerant capacity (RC) and the energy dissipation are important factors to be considered [4]. The RC is frequently used as a key value of refrigerant materials. It is defined as [6,7]

$$\mathrm{RC} = \int_{\Delta T} \Delta S_{\mathrm{iso}}(T) dT, \tag{6.4}$$

where ΔT is the useful working temperature range, which is usually defined as the range where ΔS_{iso} is larger than the half of its maximum. As seen in Fig. 6.3(a), this range corresponds to between 240 K and 290 K in the present work. Putting the values shown in Fig. 2(a) into eq. (6.4), the RC value of the Fe-Pd single crystal in the unloading process from 100 MPa is calculated to be approximately 2 MJ/m^3. This value is comparable with materials exhibiting magnetocaloric effect such as $La(Fe_{1-x}Mn_x)Si1_{1.3}$ or $Gd_5Ge_2Si_2$ compounds [4,6]. With increasing the applied stress, the RC value can be double or even triple. The energy

dissipation of the Fe-Pd single crystal can be evaluated from the stress hysteresis in the stress-strain curves (Fig. 6.1(a)), and the average hysteretic loss is approximately 0.04 MJ/m^3 in the temperature range between 240 K and 290 K. The energy dissipation of the Fe-Pd single crystal is much smaller than that of conventional SMAs with a typical first-order MT (e.g. approximately 20 MJ/m^3 for NiTi alloys [8,9]). Because of the large elastocaloric effect and the low hysteretic loss in a wide temperature range, Fe-Pd single crystal is a candidate material for an environmentally friendly refrigerator system.

6.4 Conclusions

Large elastocaloric effect has been detected in the Fe-31.2Pd (at.%) single crystal by applying a compressive stress in the $[001]_P$ direction in the temperature range between 240 K and 290 K. The temperature decrease caused by an adiabatic stress removal is approximately 2 K when the applied stress is 100 MPa. With increasing the applied stress up to 200 MPa, the temperature decrease increases to over 3 K. The refrigeration capacity is expected to be 2 MJ/m^3 when the stress maximum is 100 MPa. Such large elastocaloric effect in a wide temperature range is essentially due to a significant temperature dependence of Young's modulus in the $[001]_P$ direction.

References

[1] E. Bonnot, R. Romero, L. Manosa, E. Vives, and A. Planes, *Phys. Rev. Lett.*, **100** (2008) 125901.

[2] J. A. Rayne and B. S. Chandrasekhar, *Phys. Rev.*, **122** (1961) 1714.

[3] O. Tegus, E. Brück, K. H. J. Buschow and F. R. de Boer, *Nature*, **415** (2002) 150.

[4] V. Provenzano, A. J. Shapiro, and R. D. Shull, *Nature*, **429** (2004) 853.

[5] H. Wada, Y. Tanabe, *Appl. Phys. Lett.*, **79** (2001) 3302.

[6] K. A. Gschneidner Jr, V. K. Pecharsky and A. O. Tsokol, *Rep. Prog. Phys.*, **68** (2005) 1479.

[7] M. E. Wood and W. H. Potter, *Cryogenics*, **25** (1985) 667.

[8] J. Cui, Y. Wu, J. Muehlbauer, Y. Hwang and R. Radermacher, *Appl. Phys. Lett.*, **101** (2012) 073904.

[9] S. Miyazaki, K. Otsuka and Y. Suzuki, *Scr. Metall.*, **15** (1981) 287.

Chapter 7

Damping property of the Fe-31.2Pd (at.%) alloy

7.1 Introduction

Large elastic-like strains with a low static strain rate (5×10^{-5} s^{-1}) are obtained in Fe-Pd alloy in chapter 3 and 4; and a large elastocaloric effect is also obtained in Fe-Pd alloy with a high static strain rate (0.13 s^{-1}) in chapter 6. It is noted that the mechanical behavior of Fe-Pd alloy under different strain rates exhibits different properties. Meanwhile, the energy dissipation caused by stress hysteresis is an important factor for a refrigeration system mentioned in chapter 6. The damping characteristic in Fe-Pd alloy is also important for the technological applications [1-3].

As mentioned in chapter 1, the internal friction (IF) spectrum during a typical first-order martensitic transformation is decomposed into three terms [2,4,5]: (1) IF_{Tr}, the transitory term (or kinetic term); (2) IF_{PT}, phase transition term (or isothermal term); (3) IF_{Int}, intrinsic term as shown in Fig. 7.1(a). In conventional SMAs exhibiting a typical first-order MT such as Ti-Ni-based [6-8] or Cu-based alloys [1,2,9], the high damping characteristic is mainly caused by the first term IF_{Tr}; it appears in a narrow temperature range between M_s and M_f. The inherent internal damping values (IF_{PT}+IF_{Int}) in these alloys is small under isothermal condition. An example of the internal friction in Ti-Ni SMA [6] is presented in Fig. 7.1(b). In the heterothermal cooling process, high damping peaks caused by IF_{Tr} appear at B2-R and R-B19' transformation temperature. In the isothermal cooling process, the high damping peaks disappear and the remained damping is mainly caused by IF_{PT}+IF_{Int}. However, the damping behavior in Fe-Pd

alloy exhibiting a second-order-like MT could be quite different. So, in this chapter, we investigate the dynamic mechanical behavior and the energy dissipation of the Fe-31.2Pd (at.%) alloy.

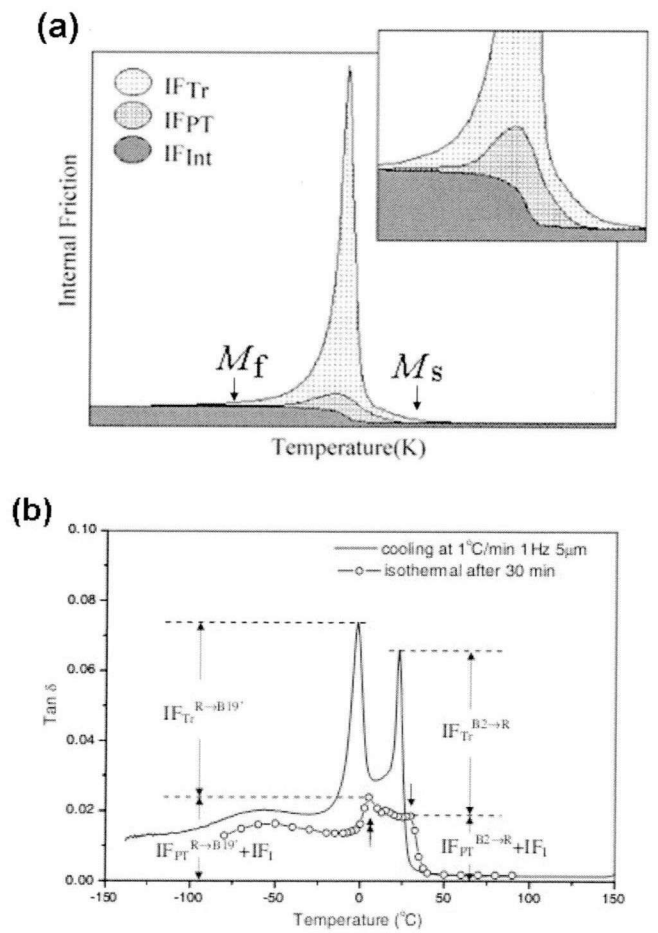

Fig. 7.1. (a) Schematic representation of the internal friction during a typical first-order martensitic transformation and its three contributions [3]. (b) The internal friction of Ti-Ni SMA under isothermal and heterothermal conditions [6].

7.2 Experiments

The polycrystals and single crystals of Fe-31.2Pd (at.%) were prepared as described in chapter 3. A parallelepiped specimen composed of $(100)_P$, $(010)_P$ and $(001)_P$ planes with a size of 3.3 mm×1.2 mm×17.5 mm was cut from the single crystal, and a polycrystal specimen with the same size was cut from the polycrystal. The FCC-FCT MT temperature of the specimens were measured by a magnetic susceptibility measurement under the magnetic field of 0.05 T with a constant cooling and heating rate of 2 K/min by using a Superconducting Quantum Interference Device (SQUID) magnetometer. The dynamic mechanical analyzers (DMA) experiments were performed on TA Q800 DMA equipment with single cantilever constant-strain mode by a multifrequency method, which is illustrated in Fig. 7.2. The strain amplitudes and the frequency were in the range of 15 to 90 μm and 0.2 to 10 Hz, respectively. Measurements were made under three different cooling/heating rates, which were 1 K/min, 2 K/min and 0 K/min. The final rate was realized by a step cooling/heating with keeping the specimen at every measuring temperature for 5 min [10]. The mechanism of the DMA is explained in the appendix.

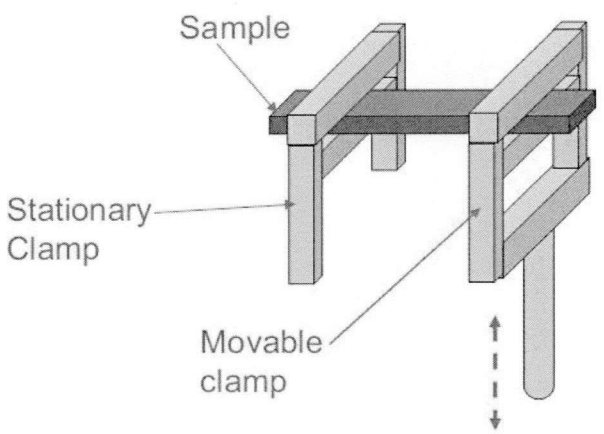

Fig. 7.2. Sketch of dynamic mechanical analyzers (DMA) with a single cantilever constant-strain mode.

7.3 Results and discussion

7.3.1 Different cooling/heating rates

Figure 7.3 presents temperature dependence of the internal friction in the Fe-31.2Pd (at.%) polycrystalline specimen (a-c) and single crystal specimen (d-f) at different cooling/heating rates. The damping behaviors are measured under constant strain amplitude 15 μm at 1 Hz. It is found that the internal friction increases slightly with increasing the cooling/heating rate. This means that the transitory term IF_{Tr} of the Fe-Pd alloy is small, and the high damping value mainly comes from IF_{PT} and IF_{Int}. It is also found that the temperature hysteresis in the cooling and heating processes significantly increases with increasing the cooling/heating rate. Here the temperature of the furnace is used for the horizontal axis. Consequently, the hysteresis is probably due to the difference between the temperature of the specimen and that of the furnace. The negligible temperature hysteresis is obtained by step cooling/heating, which is consistent with that of the magnetic susceptibility dependence on temperature mentioned in chapter 2. It is found that the behaviors mentioned above are almost same for the polycrystalline and single crystal specimens. In order to obtain thermal equilibrium condition, the step cooling/heating method is employed in the further study.

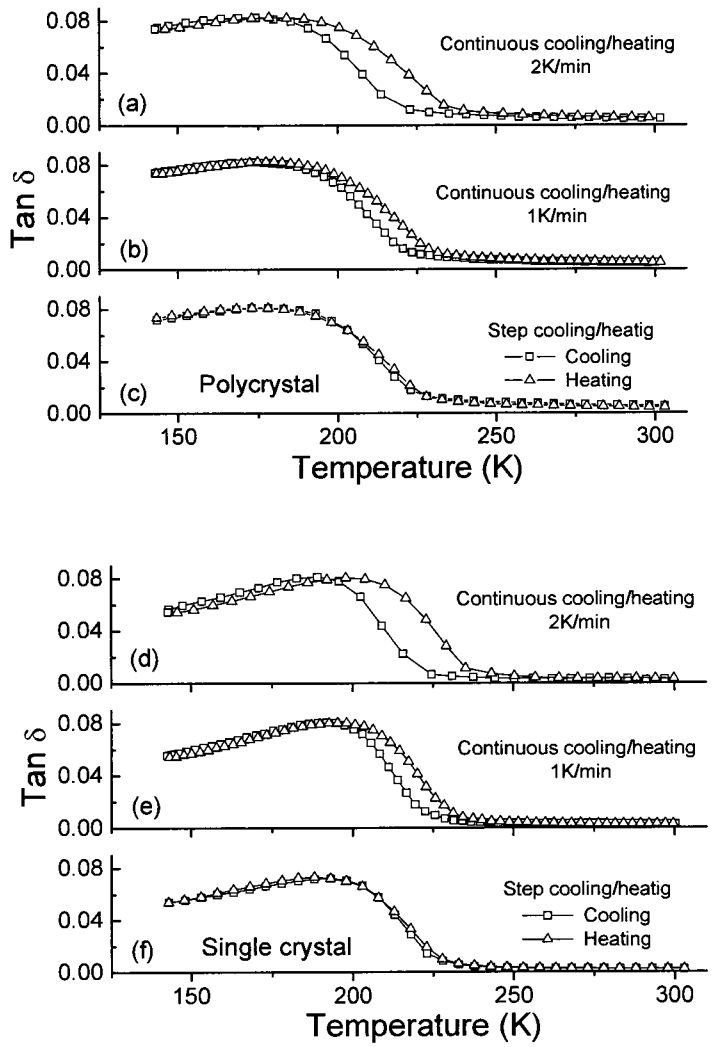

Fig. 7.3. Temperature dependence of the internal faction in the Fe-31.2Pd (at.%) polycrystal (a-c) and single crystal (d-f) at 1 Hz under strain amplitude 15 μm with continuous 2 K/min cooling/heating rate (a, d), continuous 1 K/min cooling/heating rate (b, e) and step cooling/heating rate (c, f).

7.3.2 Different frequencies

Figure 7.4 shows temperature dependence of the internal friction, the storage modulus and the magnetic susceptibility in Fe-Pd polycrystalline specimen (a-c) and single crystal specimen (d-f) in the cooling process. The damping behaviors are measured under constant strain amplitude 15 μm with different fixed frequencies. As confirmed in chapter 2, the bend in the

magnetic susceptibility curve corresponds to the FCC-FCT MT in Fe-Pd alloy. The transformation temperature of polycrystal and single crystal specimens are 225 K, which are consistent with the value reported in chapter 2. Above the transformation temperature, the storage modulus decreases with decreasing temperature, which is attributed to the lattice softening in the parent phase [11]. Then, the storage modulus increases with further decreasing temperature below the transformation temperature due to the appearance of the martensite phase. These behaviors are consistent with the trend of temperature dependence of the Young's modulus in the $[001]_P$ direction as mentioned in chapter 3. On the other hand, the internal friction keeps almost constant near-zero value above the transformation temperature, and a broad damping peak appears in the internal friction curves when the temperature is below transformation temperature. The near-zero damping value confirms the quite small stress hysteresis in the stress-strain curves and low energy dissipation mentioned in chapter 6. The high damping value below the transformation temperature is mainly attributed to the twined structure in the martensite phase which will be further discussed later. The height of the damping peak increases slightly with increasing the frequency in the polycrystal specimen, and that of the single crystal specimen is almost independence of frequency. In the temperature range between 140 K and 200 K, the average internal friction of the polycrystalline and single crystal specimens reaches approximately 0.08 and 0.07 at 10 Hz, respectively.

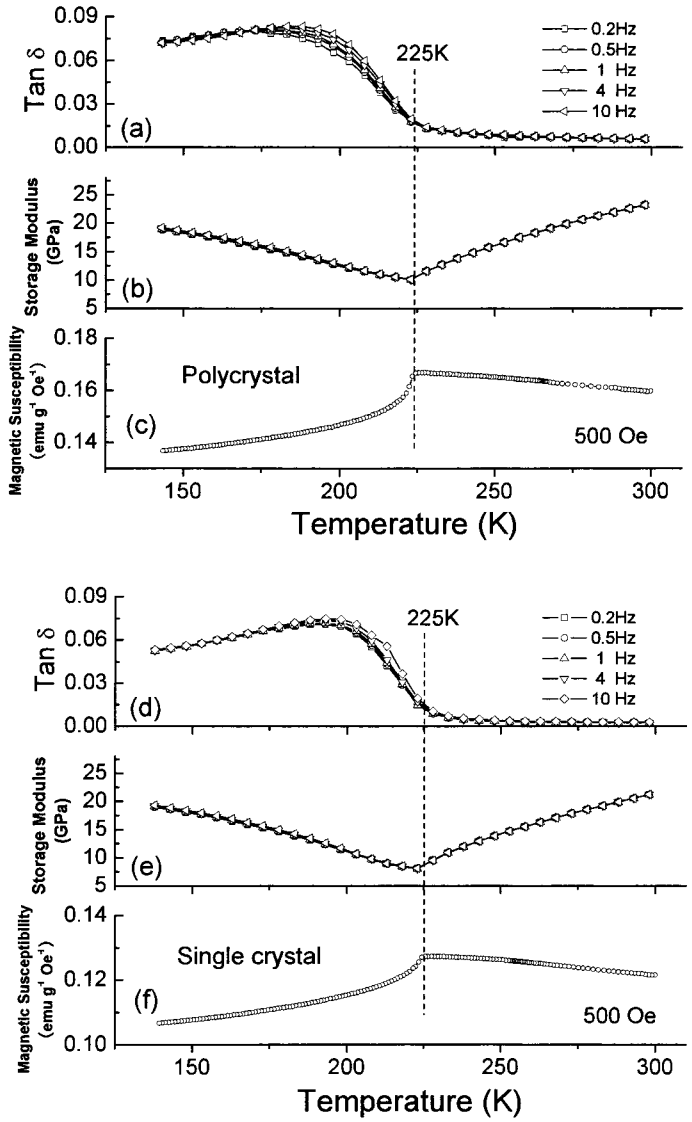

Fig. 7.4. Internal friction (a, d), storage modulus (b, e) and magnetic susceptibility (c, f) of the Fe-31.2Pd (at.%) polycrystalline specimen (a-c) and single crystal specimen (d-f) as a function of temperature in the cooling process. The damping behaviors are measured under constant strain amplitude 15 μm with frequency from 0.1 to 10 Hz.

7.3.3 Different strain amplitudes

Figure 7.5 presents the internal friction and the storage modulus of the polycrystalline (a,b) and single crystal (c,d) specimens under different fixed strain amplitude at 1Hz. It is found that,

above T_M, the storage modulus is independence of strain amplitude. But below T_M, it decreases with increasing the strain amplitude. This behavior may be caused by the movement of the martensite variants under the stress. On the other hand, the internal friction increases with increasing the strain amplitude in the martensite phase, in particular below 190 K. When the strain amplitude is 90 μm, the maximum internal friction of the polycrystalline and single crystal specimen reaches approximately 0.13 and 0.16, respectively.

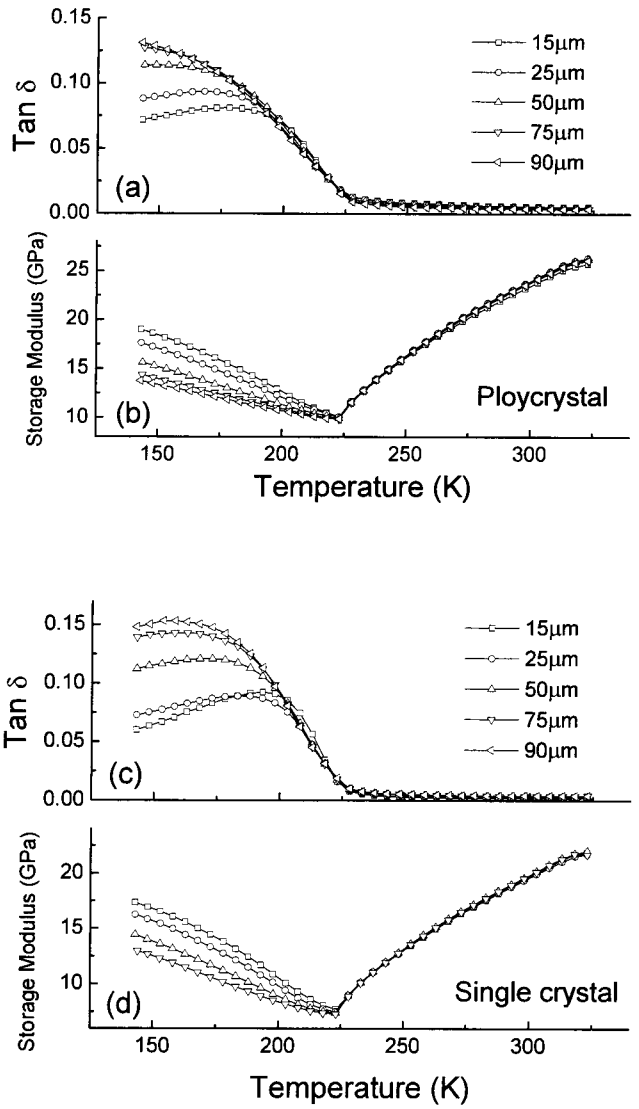

Fig. 7.5. Internal friction and storage modulus of the Fe-31.2Pd (at.%) polycrystalline (a,b) and single crystal (c,d) specimen as a function of temperature at different fixed strain amplitudes.

7.3.4 Stable damping behavior

As reported in previous papers [12,13], fine twined structures with {011} traces were frequently observed in the so-called FCT martensite phase. It is well known that the energy dissipation during the movement of the twined boundaries is an important source of high damping behaviors [1]. So, the high damping behavior is obtained in the Fe-Pd alloy under isothermal condition. Moreover, the density of the twined structures increases with decreasing temperature [12]. This could explain the continuous increase of the internal friction with decreasing temperature.

In order to further confirm the sustainability of this damping behavior, the holding tests are conducted. Figure 7.6 presents the results of the holding tests of the polycrystalline (a) and single crystal (c) specimen. The temperature change of the polycrystalline and single crystal specimens during the holding tests are indicated in Fig. 7.6(b) and (d), respectively. The holding tests are conducted at four different temperatures 223 K, 213 K, 193 K and 173 K under constant strain amplitude 15 μm at 1 Hz, and the holding time is one hour. It is found that the internal friction at these temperature have little change in the holding tests, which means the high damping behavior in the Fe-Pd alloy is quite stable. Through changing the Pd composition or adding other element [14-16], the MT temperature of an Fe-Pd alloy can be increased to room temperature or more, in other words, the stable high damping behavior can exist in a wider temperature range. Moreover, the ductility, high corrosion resistance, biocompatibility and weldability [17,18] of the Fe-Pd alloy enable it as a promising stable high damping material.

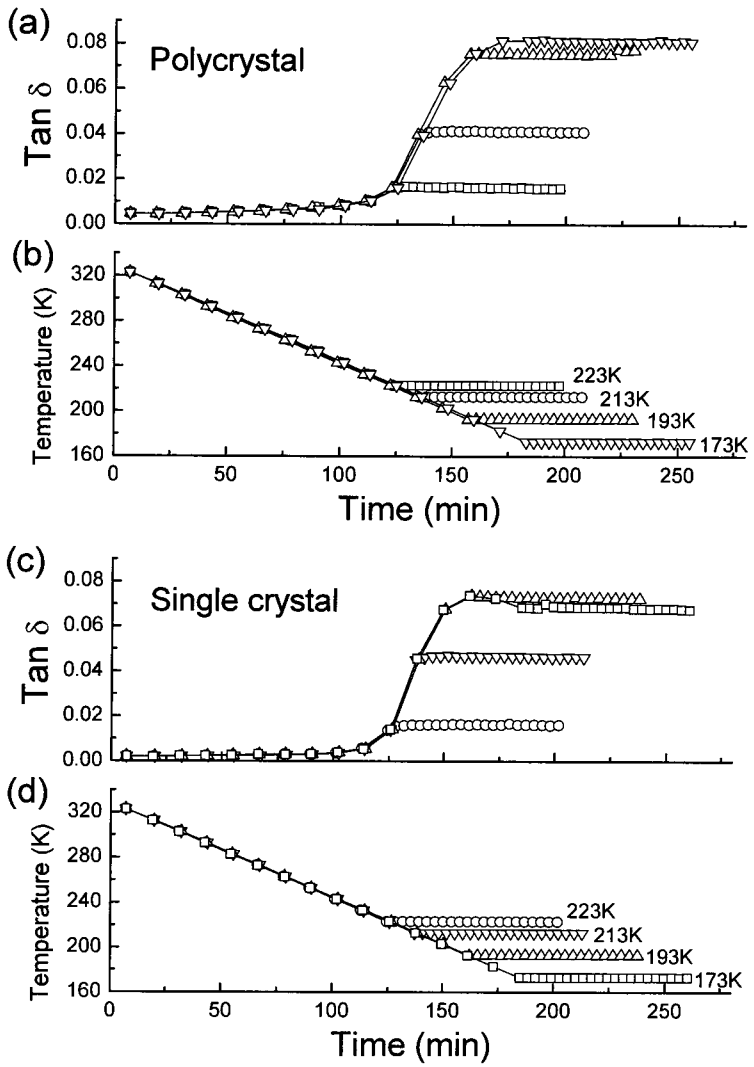

Fig. 7.6. Internal friction and temperature of the Fe-31.2Pd (at.%) polycrystalline (a,b) and single crystal (c,d) specimens as a function of time under constant strain amplitude 15 μm at 1 Hz. The holding temperatures are indicated in the figure.

7.4 Conclusions

The dynamic mechanical behavior is investigated in the Fe-31.2Pd alloy by a dynamic mechanical analyzer (DMA). It is found that the elastic modulus is independence of frequency. Also, small energy dissipation in the stress-strain curves is confirmed by low internal friction

value. A stable high damping behavior in a wide temperature range is also observed in the martensite phase.

Appendix

Dynamic mechanical properties refer to the response of a material as it is subjected to a periodic stress (or strain) [19,20]. In the present study, the stress resulting from a sinusoidal strain is considered. The sinusoidal strain can be expressed as

$$\varepsilon(t) = \varepsilon_0 \sin(\varpi t), \tag{A.1}$$

where ε_0 is the amplitude, and ϖ is the angular frequency. For an ideal solid material, the stress and strain obey Hooke's law: $\sigma(t) = \kappa\varepsilon(t)$. So, the resulting stress will be proportional to the amplitude of the applied strain with a phase lag $\delta = 0°$:

$$\sigma(t) = \kappa\varepsilon_0 \sin(\varpi t). \tag{A.2}$$

It is found that the stress amplitude σ_0 has a linear relationship with the strain amplitude: $\sigma_0 = \kappa\varepsilon_0$. For an ideal fluid which obeys Newton's law, the resulting stress is proportional to the strain rate: $\sigma(t) = \eta d\varepsilon / dt$. The resulting stress is given by

$$\sigma(t) = \eta\varepsilon_0\varpi \cos(\varpi t) = \eta\varepsilon_0\varpi \sin(\varpi t + \pi/2). \tag{A.3}$$

It is found that the stress is liner in the stain amplitude: $\sigma_0 = \eta\varepsilon_0\varpi$ depending on the angle frequency, and the phase lag between strain and stress is $\delta = 90°$. For a viscoelastic material, the resulting stress is given by

$$\sigma(t) = \sigma_0 \sin(\varpi t + \delta), \tag{A.4}$$

where the phase lag δ will lie somewhere between 0° and 90°. These behaviors are presented in Fig. A1(a), (b) and (c), respectively.

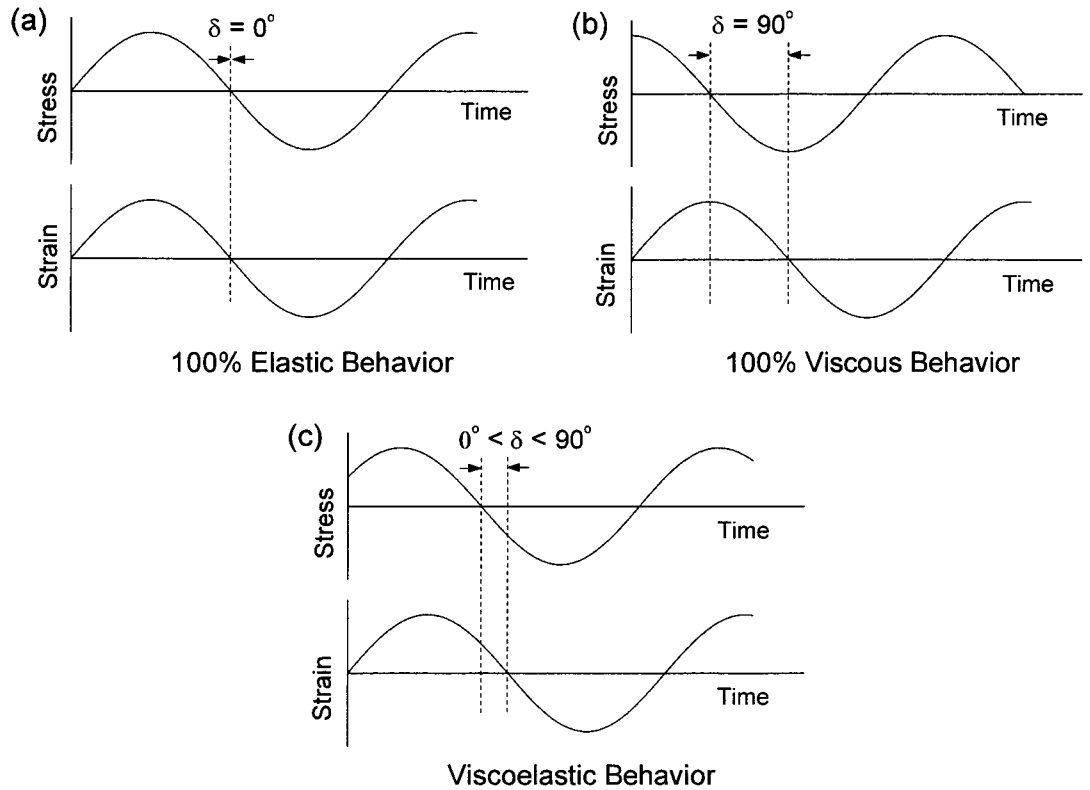

Fig. A.1. Time dependence of strain and resulting stress in a 100% elastic material (a), a 100% viscous material (b) and a viscoelastic material (c).

For the engineering application, it is common to use complex variable to describe the sinusoidal response of viscoelastic material. Thus the complex strain uses the form as:

$$\varepsilon^* = \varepsilon_0 \exp(i\varpi t), \tag{A.5}$$

and the resulting complex stress σ^* is expressed by

$$\sigma^* = \sigma_0 \exp(i(\varpi t + \delta)). \tag{A.6}$$

As the modulus is defined as the ratio of stress to strain (stress/strain), the complex modulus E^* is given by

$$E^* = \sigma^* / \varepsilon^* = \frac{\sigma_0}{\varepsilon_0}\exp(i\delta) = \frac{\sigma_0}{\varepsilon_0}\cos(\delta) + i\frac{\sigma_0}{\varepsilon_0}\sin(\delta). \tag{A.7}$$

The complex modulus E^* is a measure of the materials resistance to deformation. It encompasses elastic modulus E' (or storage modulus) and viscous modulus E'' (or loss

modulus). The storage modulus is the real part of the complex modulus: $E' = \frac{\sigma_0}{\varepsilon_0}\cos(\delta)$ (a measure of energy stored and recovered per cycle); and the viscous modulus is the imaginary part of the complex modus: $E'' = \frac{\sigma_0}{\varepsilon_0}\sin(\delta)$ (a characterization of the energy dissipated in the material by internal damping). The relationship between the complex modulus, storage modulus and loss modulus is given by

$$E^* = E' + iE'', \tag{A.8}$$

and this relationship is drawn in Fig. A.2. It can be seen from this figure that the tangent of the phase angle is the ratio of the loss modulus to storage modulus ($\tan\delta = E''/E'$ or $\tan\delta = G''/G'$). This ratio is a measure of the damping ability of a material.

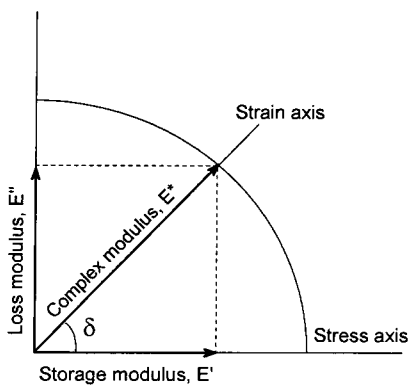

Fig. A.2. Relationship between complex modulus E^*, storage modulus E' and loss modulus E''.

References

[1] J. Van. Humbeeck, *J. Alloys Comp.*, **355** (2003) 58.

[2] J. San. Juan and M. L. Nó, *J. Alloys Comp.*, **355** (2003) 65.

[3] K. Otsuka and C. W. Wayman, *Shape Memory Materials*, (Cambridge University Press, Cambridge 1998) 166.

[4] J. E. Bidaux, R. Schaller and W. Benoit, *Acta. Metall.*, **37** (1989) 803.

[5] J. Van. Humbeeck, J. Stoiber, L. Delaey and R. Gotthardt, *Z. Metalkd.*, **86** (1995) 1976.

[6] S. H. Chang and S. K. Wu, *Scr. Mater.*, **55** (2006) 311.

[7] Y. Liu, J. Van Humbeeck, R. Stalmans, L. Delaey, *J. Alloys Compd.*, **247** (1997) 115.

[8] S. K. Wu and H. C. Lin, *J. Alloys Comp.*, **355** (2003) 72.

[9] S. H. Chang, *Mater. Lett.*, **64** (2010) 93.

[10] G. Fan, Y. Zhou, K. Otsuka, and X. Ren, *Appl. Phys. Lett.*, **89** (2006) 161902.

[11] S. Muto, R. Oshima and F. E. Fujita, *Acta. Metall.*, **38** (1990) 685.

[12] M. Sugiyama, R. Oshima and F. E. Fujita, *Trans. JIM.*, **27** (1986) 719.

[13] H. Kato, T. Wada, Y. Liang, M. Taya, T. Mori, *Mater. Sci. Eng. A*, **332** (2002) 134.

[14] M. Sugiyama, R. Oshima and F. E. Fujita, *Trans. JIM.*, **25** (1984) 585.

[15] S. Hamann et al., *Acta Mater.*, **58** (2010) 5949.

[16] V. Sanchez-Alarcos et al., *Acta Mater*, **57** (2009) 4224.

[17] J. Cui, T. W. Shield and R. D. James, *Acta. Mater.*, **52** (2004) 35.

[18] Y. Ma, M. Zink and S. G.. Mayr, *Appl. Phys. Lett.*, **96** (2010) 213703.

[19] H. T. Banks, S. Hu and Z. R. Kenz, *Adv. Appl. Math.*, **3** (2011) 2011.

[20] *TA Dynamic Mechanical Analyzer Operator's Manual* (2002).

Chapter 8

Summary

In the present study, the mechanical properties and related phenomena in Fe-Pd alloys, which exhibit a second-order-like martensitic transformation (MT), have been investigated. Following conclusions are derived.

In chapter 1, background, motivations, and purposes of this research work have been described.

In chapter 2, the Pd content dependence on the second-order-like FCC-FCT MT temperature in Fe-Pd alloys has been studied. The FCC-FCT MT temperature of Fe-Pd alloys decreases with increasing Pd content up to 33.0 at.%Pd and the transformation is suppressed in alloys including 33.1 at.%Pd and more. The latent heat of Fe-Pd alloy decreases with increasing Pd content, and is much lower than that in other shape memory alloys (SMAs), which could be attributed to the characteristic of the second-order-like FCC-FCT martensitic transformation.

In chapter 3, the deformation behavior in the Fe-31.2Pd (at.%) single crystals exhibiting a second-order-like FCC-FCT MT has been investigated by compressive tests in the $[001]_P$ direction. A large elastic-like strain of more than 6.5% with quite small stress hysteresis appears slightly above the transformation temperature (240 K) under 250 MPa. Most of the large elastic-like strain is caused by the continuous change of structure in a single variant martensite variant. A yield point appears at the strain of 7.3% and the stress of 285 MPa at 240 K, and the residual strain did not recover by heating to 300 K. Similar yield point appears at the strain of 4.6% under the stress of 310 MPa at 300 K. Introduction of mechanical twining with twin boundary {111} is the main reason of the residual strain for the plastically deformed specimens at 240 K and 300 K. The shear strength of the Fe-31.2Pd (at.%) single crystal is close to the ideal value at both temperatures, which is first reported in bulk materials with a FCC structure.

In chapter 4, the influence of various conditions on the limit of the elastic strain in Fe-Pd

alloys has been investigated. The limit of the elastic strain of Fe-Pd alloys significantly depends on temperature, which is probably attributed to the strong temperature dependence of elastic constant C'. The limit of the elastic strain is also significantly influenced by compressive direction and grain boundary because of the large elastic anisotropy in Fe-Pd alloy. On the other hand, the critical resolved shear stress is not significantly influenced by temperature and compressive direction; however, it is largely decreased by the existence of grain boundaries.

In chapter 5, the existence of a critical point in the stress-temperature phase diagram has been confirmed in Fe-30.8 and 31.2Pd (at.%) single crystals. From the stress-strain and strain-temperature curves in the $[001]_P$ direction, the critical point is determined to be (330 K, 100 MPa) for the Fe-30.8Pd (at.%) single crystal and (280 K, 40 MPa) for the Fe-31.2Pd (at.%) single crystal.

In chapter 6, a large elastocaloric effect in a wide temperature range between 240 K and 290 K has been detected in an Fe-31.2Pd (at.%) single crystal by applying a compressive stress in the $[001]_P$ direction. The temperature decrease caused by an adiabatic stress removal is approximately 2 K when the applied stress is 100 MPa. When the applied stress is 200 MPa, the temperature decrease is approximately 3 K. The refrigeration capacity is expected to be 2 MJ/m^3 when the stress maximum is 100MPa. Such large elastocaloric effect with a wide temperature range is essentially due to a significant temperature dependence of Young's modulus in the $[001]_P$ direction.

In chapter 7, the small energy dissipation of Fe-Pd alloy in the loading and unloading processes above its transformation temperature is confirmed by DMA measurements. It is also found that there is almost no frequency dependence of damping in the range between 0.1 Hz and 10 Hz. In addition, a stable high damping behavior is obtained in the Fe-31.2Pd (at.%) alloy in the temperature range between 150 K and 200 K. This high damping value is time independent, and probably originates from the high density of twinned structure in the martensitic phase.

In this study, we confirm large elastic strains, the existence of critical point in stress-temperature phase diagram, a large elastocaloric effect and stable high damping behavior

in Fe-Pd alloys exhibiting a second-order-like FCC-FCT martensitic transformation. Owing to their high corrosion resistance, ductility and biocompatibility, Fe-Pd alloy is a promising SMA to be widely applied in many fields.

Publications

1. Fei Xiao, Takashi Fukuda and Tomoyuki Kakeshita

   "Concentration dependence of FCC to FCT martensitic transformation in Fe-Pd alloys"

   Journal of Alloys and Compounds, 2012, article in press

   DOI: 10.1016/j.jallcom.2012.02.011

2. Fei Xiao, Kaname Yashima, Takashi Fukuda and Tomoyuki Kakeshita

   "Superelasticity of single crystalline Fe-30.8 at.%Pd alloy"

   Materials Science Forum, 2012, accepted

3. Fei Xiao, Takashi Fukuda and Tomoyuki Kakeshita

   "Composition dependence of martensitic transformation and supperelastic behavior in Fe-Pd alloys"

   Proceedings of ECO-MATES 2011, PT 9-9, 247-248

4. Fei Xiao, Takashi Fukuda and Tomoyuki Kakeshita

   "Elastic deformation of Fe-31.2Pd (at.%) alloy exhibiting lattice softening"

   Proceedings of TMS spring meeting, 2013, accepted

5. Fei Xiao, Takashi Fukuda and Tomoyuki Kakeshita

   "Large elastic-like deformation in an Fe-31.2Pd (at.%) single crystal exhibiting a second-order-like martensitic transformation"

   Submitted to *Acta Materialia*

6. Fei Xiao, Takashi Fukuda and Tomoyuki Kakeshita

"Large elastocaloric effect in an Fe-31.2Pd (at.%) single crystal"

To be published

7. Fei Xiao, Takashi Fukuda and Tomoyuki Kakeshita

"Stress-temperature phase diagram of an Fe-31.2Pd (at.%) single crystal"

To be published

Presentations

International conferences

1. Fei Xiao, Takashi Fukuda and Tomoyuki Kakeshita

   "Composition dependence of martensitic transformation and supperelastic behavior in Fe-Pd alloys"

   Eco-Materislas Eco-Innovation for Global Sustainability, ECO-MATES 2011

   November 2011, Osaka, Japan

2. Fei Xiao, Takashi Fukuda and Tomoyuki Kakeshita

   "Concentration dependence of FCC to FCT martensitic transformation in Fe-Pd alloys"

   International Conference on Martensitic Transformations, ICOMAT 2011,

   September 2011, Osaka, Japan

3. Fei Xiao, Takashi Fukuda and Tomoyuki Kakeshita

   "Superelastic behavior associated with second-order-like martensitic transformation in a disordered Fe-31.2Pd (at.%) alloy"

   The European Symposium on Martensitic transformations, ESOMAT 2012

   September 2012, Sankt Peterburg, Russia

4. Fei Xiao, Takashi Fukuda and Tomoyuki Kakeshita

   "Elastic Deformation in Fe-31.2Pd (at.%) alloy exhibiting lattice softening"

   The Minerals, Metals & Materials Society Annual Meeting & Exhibition, TMS 2013

   March 2013, San Antonio, USA (to be presented)

Domestic conferences

1. Fei Xiao, Takashi Fukuda and Tomoyuki Kakeshita

   "Phase diagram of FCC-FCT martensitic transformation and a large reversible strain in Fe-Pd alloy"

   The Japan Institute of Metals, Annual Fall Meeting, September 2011

   Okinawa convention center, Okinawa

2. Fei Xiao, Takashi Fukuda and Tomoyuki Kakeshita

   "Superelastic behavior in Fe-31.2at.%Pd single crystal"

   The Japan Institute of Metals, Annual Fall Meeting, March 2012

   Yokohama National University, Yokohama

3. Fei Xiao, Takashi Fukuda and Tomoyuki Kakeshita

   "Large elastic-like deformation in ferromagnetic Fe-31.2Pd (at.%) single crystal"

   The Magneto-Science Society of Japan, 7th Fall Meeting, Nov 2012

   Kyoto University, Kyoto

4. Fei Xiao, Takashi Fukuda and Tomoyuki Kakeshita

   "Temperature dependence of elastic strain and a large elastocaloric effect in Fe-31.2Pd (at.%) alloy"

   Zairyo Bussei Kougaku Danwakai, Jan, 2013

   Osaka University, Osaka

Acknowledgements

The author wishes to express sincere appreciations to Dr. Tomoyuki Kakeshita, Professor of the Division of Materials and Manufacturing Science, for his long term support and his valuable comments over the course of my doctoral research in Osaka University.

I am greatly indebted to Dr. Hidehiro Yasuda, Professor of the Research Center for Ultra-High Voltage Electron Microscopy, and Dr. Hiroyuki Yasuda, Associate Professor of the Division of Materials and Manufacturing Science who have served as members of my doctoral dissertation examination committee, for their valuable comments and enlightening discussions.

I owe my warmest gratitude to Dr. Takashi Fukuda, Associate Professor of the Division of Materials and Manufacturing Science, for his guidance and support during my study and research works.

I gratefully acknowledge Dr. Tomoyuki Terai, Associate Professor of the Division of Materials and Manufacturing Science, for his continuous kind help.

I take this opportunity to express my sincere gratitude to Dr. Xuejun Jin, Professor of the School of Materials Science and Engineering in Shanghai Jiao Tong University, for his encouragement and constructive comments.

I am grateful to Mr. Eiji Taguchi, technical staff of the Research Center for Ultra-High Voltage Electron Microscopy for his kind assistance regarding the electron microscopy research parts of the present study.

I also take this opportunity to express my sincere gratitude to Dr. Kohki Takahashi, Assistant Professor of High Field Laboratory for Superconducting Materials in Tohoku University, for providing the *in-situ* X-ray diffraction of this work.

I wish to appreciate Dr. Yan Feng and Dr. Mingjiang Jin for their encouragement and great support during my doctoral study. I also own my sincere gratitude to all members of Kakeshita Laboratory for their helps during my study in Japan.

This study was supported by Priority Assistance for the Formation of Worldwide Renowned Centers of Research - The Global COE Program (Project: Center of Excellence for Advanced Structural and Functional Materials Design) from the Ministry of Education, Culture, Sports, Science and Technology (MEXT), Japan.

Most importantly, I would like to express my deepest gratitude to my parents for their love and support which without I would not have been able to complete the doctoral degree.

Fei Xiao

March 2013